



**University Library**

Author/Filing Title ..... SEATON, A. ....

Class Mark ..... T .....

Please note that fines are charged on ALL  
overdue items.

FOR REFERENCE ONLY

040341119X





**THERMOMECHANICAL DEFORMATION OF SHAPE MEMORY  
ALLOYS**

by

**Alexander Brian Seaton**


**A Doctoral Thesis  
submitted in partial fulfilment of the requirements  
for the award of  
Doctor of Philosophy  
of  
Loughborough University**

**September 2006**

**Supervisor: Dr. G. M. Swallowe**

**Department of Physics**

**© Alexander Brian Seaton**

	Loughborough University Pilkinson Library
Date	JAN 2007
Class	T
*Acc No.	040341119X



# Abstract

NiTi is a shape memory alloy and can undergo crystallographically reversible martensitic transformation under applied loads resulting in recoverable of strains of the order of 5 %. The single crystal properties of shape memory alloys have been studied extensively in the past and a good understanding of the mechanical properties of the material in this form has been acquired. However, when used in practical applications shape memory alloys are used in their polycrystalline form. In a polycrystalline form the deformation behaviour may be quite different to that of a single crystal due to the constraints of surrounding grains and anisotropy of material properties. In the case of shape memory alloys these are anisotropic elastic and transformation properties.

The main focus of the work in this thesis is the deformation behaviour of commercial rod samples of NiTi while under thermomechanical loads. The grain-orientation-specific internal strain development and phase fraction evolution within particular grain orientations is evaluated during deformation by the in-situ neutron diffraction technique.

The experimental results presented include stress-induced martensitic transformation, cooling through the martensitic transformation under a fixed stress, the generation of recovery stresses while heated under constraint, and studies of the detwinning of the B19' martensite phase under compressive and tensile loading. In addition, the effect of ageing on mechanical properties of NiTi is investigated via the method.

Changes in the load partitioning behaviour is noted for NiTi cooled under a fixed tensile stress of 200 MPa which compare well with modelling predictions in the literature. Large changes in the mechanical properties of NiTi as a results of ageing are ascribed to the presence of the R-phase due to the formation of precipitates during ageing. Evidence of detwinning of B19' martensite in both tension and compression is found, in contrast to other work in the literature.

## Acknowledgments

Firstly I would like to thank my supervisor, Dr. Gerry Swallowe, for his help, advice and guidance over the course of this work. I would also like to thank Dr. Petr Sittner who has also been of great help and assistance, and has given me the benefit of his knowledge of the properties of NiTi and application of the neutron diffraction technique to its study. Thanks are due to the instrument scientists dealing with ENGIN-X: Drs. Daymond, Oliver and Santistiban – and in particular Ed Oliver – who has provided assistance above and beyond the call of duty. Also, thanks are due to Prof. A. R. Rennie and Dr. R. L. Peng for provision of laboratory facilities, help and beamtime at the NFL facility in Studsvik, Sweden. Mr. T. Edwards and Mr. B. Seaton are thanked for their expert and rapid machining of test samples. All members of the technical and administrative staff in the Department of Physics are thanked for help over the past years: Mrs. M. Mackenzie, Mrs. T. Moore, Mr. B. Dennis, Mr. M. Stenlake, Mr. B. Chavda, Mr. R. Pancholi, and Mr. R. Pancholi.

# Table of contents

## **1 Introduction to martensitic transformations and shape memory alloys**

1.1 Aims and objectives of the thesis	1
1.2 Phase transformations in general	2
1.3 Martensitic transformation	4
1.3.1 Introduction	4
1.3.2 Thermodynamic aspects of martensitic transformations	6
1.3.3 Kinetics of martensitic transformations	9
1.3.4 Effect of stress on transformation behaviour	10
1.4 Crystallography of the martensitic transformation	12
1.4.1 Introduction	12
1.4.2 Experimental observations during martensitic transformation	12
1.4.3 Bain model of martensitic transformation	14
1.4.4 Wechsler, Lieberman and Read and Bowles and Mackenzie theory	18
1.5 Shape memory alloys	19
1.5.1 Introduction	19
1.5.2 Thermomechanical behaviour of shape memory alloys	20
1.5.3 Calculation of strain generated due to transformation	22
1.6 Physical metallurgy of NiTi: crystal structures and phase diagrams	23
1.7 References	24

## **2 Introduction to internal strain measurement by diffraction techniques**

2.1 Introduction	27
2.2 Diffraction	27
2.2.1 Introduction to diffraction and Bragg's law	27

2.2.2 Neutron diffraction	30
2.2.3 Reactor neutron sources	30
2.2.4 Spallation neutron sources	33
2.3 The ENGIN-X diffractometer	36
2.3.1 Sample positioning	36
2.3.2 Detectors	36
2.3.3 Beam slits	37
2.3.4 Stress rig	38
2.4 Strain measurement using neutrons	38
2.4.1 Types of stresses evaluated	38
2.4.2 Strain scanning	39
2.4.3 Lattice strain in polycrystals under loading	41
2.4.4 Single peak fitting of diffraction spectra	45
2.5 References	48

### **3 Stress-induced martensitic transformation in NiTi using in-situ neutron diffraction**

3.1 Introduction	53
3.1.1 Literature review	53
3.2 Experimental details and material	56
3.3 Results and discussion	57
3.3.1 Macroscopic response	57
3.3.2 Sample texture	58
3.3.3 Intensity and phase fraction changes on loading	59
3.3.4 Lattice strain response	63
3.4 Conclusions	66
3.5 References	67

### **4 Deformation of aged NiTi studied using in-situ neutron diffraction**

4.1 Introduction	70
------------------	----

4.1.1 General	70
4.1.2 Precipitation process in Ni-Ti	71
4.1.3 R-phase martensitic transformation	72
4.1.4 Multi-step transformation behaviour in nickel-rich alloys	75
4.1.5 Methods of analysis	78
4.1.6 Objectives of present study	81
4.2 Experimental details	81
4.2.1 Material and heat treatment	81
4.2.2 Experimental arrangement	82
4.3 Results and discussion	83
4.3.1 Calorimetry results	83
4.3.2 Mechanical response	84
4.3.3 Diffraction results	86
4.3.3.1 Room temperature microstructures	86
4.3.3.2 Deformation of solution heat treated sample	90
4.3.3.3 Sample aged at 400 °C for 1.5 hours	91
4.3.3.4 Sample aged at 400 °C for 20 hours	95
4.4 Conclusions	96
4.5 References	97

## **5 Deformation twinning in NiTi under tensile and compressive stress**

5.1 Introduction	102
5.1.1 Stress-free twins in B19' martensite	102
5.1.2 Mechanical behaviour of twinned B19' martensite	103
5.1.3 Objectives of present work	105
5.2 Experimental details	106
5.2.1 Material	106
5.2.2 In-situ diffraction experiments	107
5.2.3 REST diffractometer	108
5.3 Results and discussion	108
5.3.1 Macroscopic stress-strain response	109
5.3.2 Intensity evolution	109

5.3.3 Pole figures	113
5.3.4 Lattice strain evolution	114
5.4 Conclusions	115
5.5 References	115

## **6 Cooling under fixed stress and recovery stress generation in NiTi**

6.1 Introduction	117
6.1.1 Martensitic transformation under constraint	117
6.1.2 Objectives of present work	119
6.2 Experimental details	119
6.2.1 Material	119
6.2.2 Diffraction measurements	120
6.3 Results and discussion	120
6.3.1 Cooling under fixed tensile stress of 200 MPa	120
6.3.2 Recovery stress generation	123
6.4 Conclusions	126
6.5 References	126

## **7 Conclusions and suggestions for future research**

7.1 Summary	128
7.2 Future research	131

## **Appendix A: The Sittner-Novak model**

A1 Introduction	133
A2 Properties and assumptions	133
A3 References	134

# **Chapter 1:**

## **Introduction to martensitic transformations and shape memory alloys**

### **1.1 Aims and objectives of the thesis**

The main focus of the work contained within this thesis is the type II intergranular strains developed due to phase transformations in shape memory alloys conducted almost exclusively at the ISIS facility and using the ENGIN-X diffractometer.

The ability of polycrystalline shape memory alloys to transform under an applied thermal and/or mechanical load depends to some extent on the intergranular stresses which developed during transformation. This is known as the partitioning of the applied stress and as mentioned in the previous section, is due to differential material properties. In the case of shape memory alloys intergranular stresses arises due to two main causes: the elastic anisotropy – due to the difference in elastic constants – and the transformation anisotropy, i.e. the propensity of different austenite grain orientations to transform at different stresses.

The single crystal properties of shape memory alloys have been studied extensively over the previous 50 years and a good understanding of the mechanical properties of the material in this form has been acquired. However, when used in practical applications shape memory alloys are used in their polycrystalline form. Thus the way in which the intergranular strain

develop during transformation is of crucial importance to understanding the mechanical properties in this state. Also of interest is the texture, which reflects the evolving variant microstructure during martensitic transformation. All of these may be evaluated using the in-situ neutron diffraction method.

In what follows, the in-situ diffraction technique is applied to the study of the thermomechanical deformation behaviour of NiTi, the most widely used shape memory alloy. The experiments have been conducted on commercially available rod samples.

The experiments have been chosen such that they encompass all the types of deformation under the application of thermomechanical loads that may be encountered while being used in practical applications. Thus the experiments include the following: stress-induced martensitic transformation, cooling under a fixed stress in order that a controlled displacement is achieved, the generation of recovery stresses due to constrained heating, and studies of the detwinning of the B19' martensite phase under compressive and tensile loading. In addition, the very important problem of the effect of ageing on mechanical properties of NiTi is investigated.

## **1.2 Phase transformations in general**

A phase can be described as that part of a system which has uniform physical and chemical properties. For example, a glass of water is a single phase system. However, if it is cooled and ice crystals begin to appear and coexist with the water, then this becomes a two-phase system. Further



cooling results in the rest of the water turning to ice and the system is once again single phase. The above example of water becoming ice is an example of a phase transformation. Phase transformations of one type or another can be induced by changes in pressure and/or temperature of a system, with the ability to transform being governed by the availability of both a driving force, i.e. a difference in the Gibbs free energy of the phases, and a route and finite time period in which the transformation can be completed, known as the kinetics of the transformation (Ashby and Jones, 1998).

Phase transformations can be classified into two distinct groups: diffusive and martensitic, or displacive, transformations. The diffusive transformation involves the free movement of atoms over a range greater than that of the interatomic spacing in a solid. Examples of this type of transformation are melting and solidification, and recrystallisation in heavily deformed metals. Martensitic transformations, on the other hand, involve a coordinated movement of atoms, in a shear-like manner, over distances less than that of interatomic spacing. The orderly manner in which these types of transformations occur have lead them to be called ‘military’ transformations by some.

Diffusional transformations are by far the more prevalent in nature, but the martensitic transformation, probably best known through its use as a strengthening mechanism in steels, is of great interest from a technological perspective. It will be seen that the martensitic transformation lies at the heart of the unique properties of shape memory alloys when these are discussed later on in the chapter.

The terms displacive, military and martensitic are all equivalent in usage. The word martensitic derives from martensite – a term originally used only

to describe the product phase formed on quenching iron, containing a small amount of carbon in solution, from red heat. It has subsequently become a generic term for the product phase of any displacive transformation.

Thermodynamic, crystallographic and mechanical aspects of the martensitic transformation will now be discussed. In order to define some essential terminology, such as Bain strain and habit plane, the familiar example of the martensitic transformation in the Fe-C system will be discussed briefly. This will then be followed by a discussion of the properties of shape memory alloys in general. Next will be the properties of the most popular shape memory alloy, NiTi: the main alloy studied in this thesis.

### **1.3 Martensitic transformation**

#### *1.3.1 Introduction*

Martensitic transformations are named after the distinguished German metallurgist, Dr. Adolf Martens, in honour of his contributions to the understanding of the mechanical properties of steels, based on microscopical investigations of the microstructure in various alloys.

The martensitic transformation begins at a well-defined starting temperature known as the martensite start temperature, denoted  $M_s$ . As mentioned above martensitic transformation are diffusionless and occur via the homogeneous deformation of the parent phase in a shear-like manner. The transformation occurs in an abrupt manner at speeds approaching that of the speed of sound in the materials, i.e. of the order of  $1000 \text{ m s}^{-1}$ . Although this is not a direct

requirement for a martensitic material, as some transformations occur at a much slower rate than this.

It is solid-solid phase transformation which involves a change in crystal structure from, generally speaking, a higher symmetry phase known as austenite, to a lower symmetry phase (martensite). The transformation is first order and therefore is associated with the evolution or absorption of a latent heat.

The transformation can be observed either metallographically or even with the naked eye in some cases. A well polished surface is required (that has been polished while in the austenite phase). Upon cooling the following will be seen: when the  $M_s$  temperature is reached plates of martensite will be formed on specific planes within the visible grains, as shown in Figure 1.1. Martensitic transformations are highly crystallographic in character and form on well-defined crystal planes. These are the so-called habit planes, which form the interface between the martensite phase and the austenite phase (Honeycombe and Bhadeshia, 1995). Under conditions of stress-free cooling the martensite plates will be seen to form in several different orientations proportional to the multiplicity of the a habit plane. For example, a material such as indium-thallium has 24 of these, with the  $\{110\}$  planes being the habit planes (or at least very close to this index, as the habit planes are usually irrational).

The martensite start temperature for some materials are shown in Table 1.1.

So, how does one know for sure if the martensitic transformation is displacive or whether diffusion plays some part in its formation? As can be seen in Table 1.1 the martensite start temperature can vary over a large

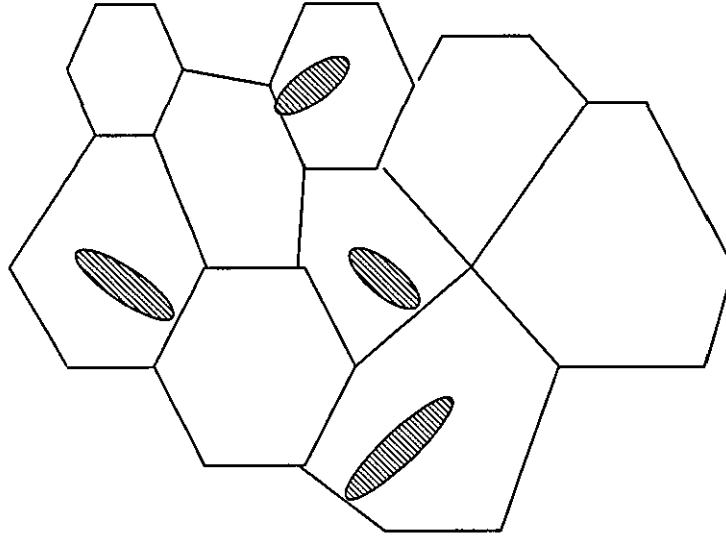


**Figure 1.1:** Schematic diagram of the grain structure of a polycrystalline material which exhibits the martensitic transformation. The shaded regions are the plates of martensite which have nucleated on the grain boundaries and grown into the grains. This growth occurs on specific planes known as the habit planes.

Material and composition	Martensite start temp. [K]
ZrO <sub>2</sub>	1200
Cu-15Al	253
Fe-31Ni-0.23C	83

**Table 1.1:** Selected materials exhibiting martensitic transformations and their associated martensite start temperatures. Data from Bhadeshia, 2001.

range of temperature, from the very high to the very low. Evidence of such low temperature transformation, such as that seen for Fe-31Ni-0.23C in Table 1.1, originally provided the experimental evidence that the martensite formations does indeed take place without diffusion of atoms. However this evidence on its own is not wholly convincing, as there are some transformations which take place at temperatures at which diffusion is not an inconceivable transformation path. Further evidence is required. This is found in the form of the speed at which martensite plate formation occurs and the lack of composition change upon transformation. These observations, when combined together, indicate that the martensitic transformation is truly diffusionless (Bhadeshia, 2002).

### *1.3.2 Thermodynamic aspects of the martensitic transformations*

The driving force for phase transformations is given by the difference in Gibbs free energy,  $\Delta G = G_M - G_A$ , of two phases, where  $G_M$  is the Gibbs free energy of the martensite phase and  $G_A$  is the Gibbs free energy of the austenite parent phase. The diagram in Figure 1.2 illustrates the respective free energy curves for the martensite and austenite phases and includes some of the key features such as the  $M_s$ ,  $A_s$  and  $T_0$ .

The equilibrium temperature,  $T_0$ , is given by (Tong and Wayman, 1974) as:

$$T_0 = \frac{A_f + M_s}{2}.$$

This is the temperature at which the Gibbs free energy of the two phases is equal.

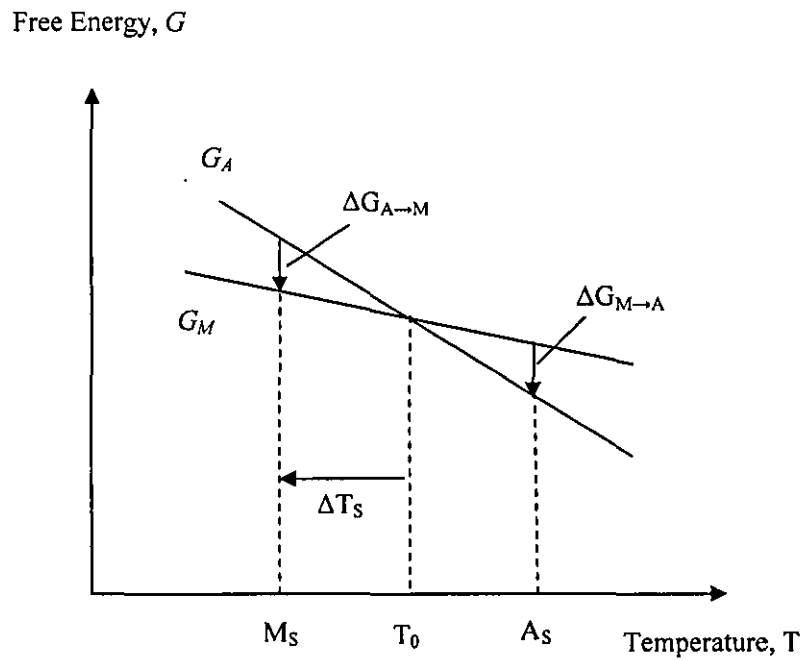


**Figure 1.2:** Diagram of the Gibbs free energy curves for the martensite,  $G_M$ , and austenite,  $G_A$ . The equilibrium temperature,  $T_0$ , the martensite start temperature,  $M_S$ , and the austenite start temperature,  $A_S$ , are all marked on the diagram. Also included are the Gibbs free energy differences for the austenite  $\rightarrow$  martensite and martensite  $\rightarrow$  austenite transformations at the  $M_S$  and  $A_S$  temperatures respectively. (After Kaufmann and Cohen, 1958).

The change in the Gibbs free energy can be factorised into the following components (Kaufmann and Cohen, 1958):

$$\Delta G = \Delta G_c + \Delta G_s + \Delta G_e = \Delta G_c + \Delta G_{nc}.$$

With the symbols having the following meaning,

$\Delta G_c$ : chemical free energy term due to the differences in crystal structures between the two phases.

$\Delta G_s$ : a non-chemical quantity which represents the surface energy between the two phases.

$\Delta G_e$ : another non-chemical quantity which represent the free energy contribution of the elastic and plastic strain around the formed martensite.

The last two terms can be combined to give the total contribution of non-chemical terms, and it is important to note that in the case of martensitic transformations this non-chemical energy can be as large as the chemical term due to the large shape change that is usually involved. This is the reason why the material needs to be cooled below its equilibrium temperature,  $T_0$ , before the martensite start temperature is reached and martensite plates begin to form. The transformation is therefore said to require ‘supercooling’ to begin (Otsuka and Wayman, 1998). The same principle applies for the reverse transformation of martensite to austenite, which is possible for shape memory alloys, where a ‘superheating’ of the material is required to begin the transformation.

In the same way in which phase transformations in general can be divided into those which are diffusive and martensitic, it is possible to further subdivide the martensitic transformations into those which are thermoelastic and non-thermoelastic. The martensitic transformation in shape memory alloys such as NiTi is thermoelastic, whereas in other martensitically transforming materials such as some Fe-Ni alloys they are non-thermoelastic. The characteristics of the thermoelastic and non-thermoelastic transformation are quite different. Non-thermoelastic transformations require a very large driving force and generally involve a greater change in shape. This large shape change often results in plastic deformation occurring around the martensite plate causing there to be a lack of coherency between the plate and its parent phase, and thus results in the plates ceasing to grow with decreasing temperature. Reactions such as this therefore do not result in a fully martensitic microstructure and some residual austenite will remain (Machlin and Cohen, 1952).

This type of transformation has a very large hysteresis (of the order of several hundred Kelvin) between the forward transformation, i.e. austenite to martensite, and the reverse transformation from martensite to austenite. In the case of non-thermoelastic transformations, on the reverse transformation the austenite is grown in a similar way to recrystallisation: by renucleation and growth of the austenite grains (Kessler and Pitch, 1967).

By contrast, thermoelastic transformations require less driving force and thus have much smaller hysteresis in the forward and reverse transformations (of the order of tens of Kelvin). This type of transformation is characterised by having a highly mobile austenite-martensite interface. Experimentally, it can be observed that the existing martensite plates grow in size on cooling and shrink on heating due to this interface mobility



(Kurdjimov and Khandros, 1949) and in a suitably cut single-crystal a single interface will be seen to travel from one end of the crystal to the other as the temperature is lowered. On the reverse transformation, the opposite occurs, with the interface sweeping through the crystal in the opposite direction. The transformation via single-interface is in distinct contrast to that seen in the non-thermoelastic transformation discussed in the previous paragraph, where many plates are nucleated and grow almost immediately to their final size (Reed-Hill, 1964).

Thermoelastic transformations therefore result in the re-grown parent phase being microstructurally identical to its starting structure, i.e. the austenite grains have the same orientation as they possessed prior to transformation. The transformation can therefore be termed crystallographically reversible. The transformation in NiTi is thermoelastic and, as will be seen later in this chapter, results in some very interesting properties.

### *1.3.3 Kinetics of martensitic transformations*

Growth of martensite can occur in several different ways. The kinetics of martensitic transformations can be classified as follows (Honeycombe and Bhadeshia, 1995):

- Athermal: The transformation begins at the well defined martensite start temperature,  $M_s$ , and then continues on further cooling only. There is no isothermal transformation in this type of reaction, i.e. the martensite volume fraction will remain constant if the temperature remains constant.

- Athermal with bursts: This type begins with an increasing volume fraction of martensite plates and then proceeds as the athermal reaction. It therefore has an isothermal character initially.
- Isothermal: This type of transformation proceeds at a constant temperature, with the volume fraction of martensite being dependent only upon the isothermal holding time.

Schematic diagrams of the martensite volume fraction evolution are shown in Figure 1.3. The athermal type of transformation is the most common, with isothermal martensitic transformations only being found in iron alloys that are free of carbon (Honeycombe and Bhadeshia, 1995). The main alloy discussed within this thesis, NiTi, exhibits an athermal martensitic transformation.

#### *1.3.4 Effect of stress on transformation behaviour*

The martensitic transformation occurs in a shear-like manner and therefore it would be expected that shear stress acting on a habit plane should have some effect on the transformation.

Uniaxial stress applied to a martensically transforming material acts to raise the martensite start temperature and thus aids the transformation. That is not to say any type of stress aids the transformation, as in some cases in which a hydrostatic stress, i.e. a stress without a shear component, has been applied to a material such as Fe-Ni alloy, the transformation has been seen to be retarded. The role of the hydrostatic stress in aiding or resisting the transformation is dependent upon the volume change during transformation. In the case where the volume change, or more accurately the dilatation

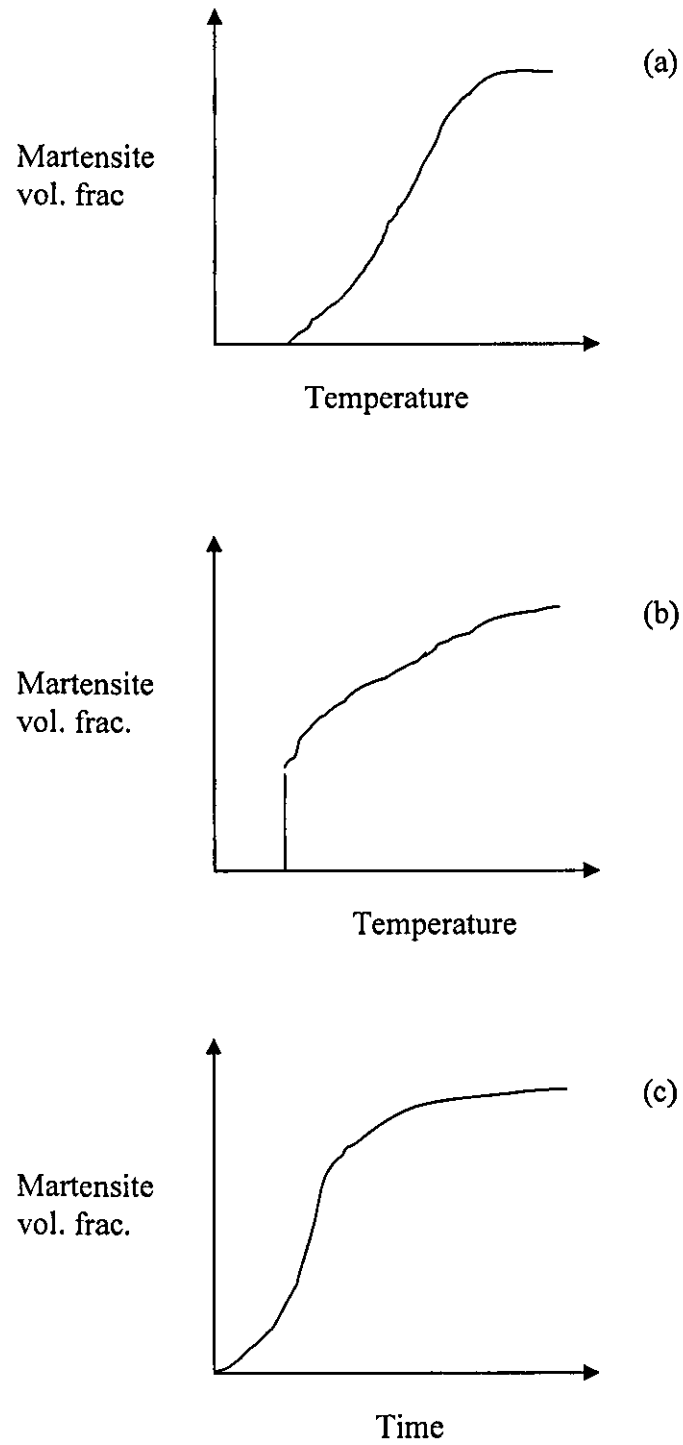


**Figure 1.3:** Schematic diagrams of the evolution of martensite volume fractions during the various types of martensitic transformation: (a) athermal, (b) athermal with bursts, and (c) isothermal. See text for details. Diagrams after Christian, 1970.

( $=\Delta V/V$ ), upon transformation is less than zero then the hydrostatic stress will aid the transformation, i.e. increase the  $M_s$  temperature. If the dilatation is positive then the hydrostatic stress resists the transformation, i.e. the  $M_s$  temperature is depressed (Otsuka and Wayman, 1998). Only uniaxial tests are used in the work presented in this thesis.

The well-known Clausius-Clapeyron equation can be used to describe behaviour of first-order phase transition behaviour such as the martensite formation discussed here. The Clausius-Clapeyron equation allows the prediction of the slopes of the phase transformation lines on a pressure-temperature phase diagram (Rock, 1983) and thus allows estimation of transformation temperatures/pressures. It is shown in equation 1.1:

$$\frac{dP}{dT} = \frac{\Delta H}{T\Delta V}. \quad (1.1)$$

Where  $P$  is the pressure,  $T$  is the temperature,  $\Delta H$  is the latent heat of transformation and  $\Delta V$  is the change in volume due to transformation. In the case of a uniaxial applied stress acting on a material this can be rewritten using metallurgical terms as:

$$\frac{d\sigma}{dT} = \frac{-\Delta H}{\epsilon T}. \quad (1.2)$$

Where  $\sigma$  represents the uniaxial applied stress (either compressive or extensional) and  $\epsilon$  is the accumulated strain resolved along the direction of the applied stress (Wayman and Duerig, 1990). It will be seen in later sections how this equation can be applied to the study of the mechanical properties of shape memory alloys.

## **1.4 Crystallography of the martensitic transformation**

### *1.4.1 Introduction*

The crystallography of martensitic transformations will now be discussed, starting with the experimental observations and finishing with a discussion on the various theories available to help predict the crystallographic details of the transformation.

By way of introduction, the classical example of martensite formation in an alloy of iron and carbon is focussed upon.

Originally, the martensitic transformation was used specifically to describe the FCC-BCT phase transformation occurring in steels, but, as mentioned previously, it has now become the generic term for a particular phase transformation which occurs in many alloys and also includes non-metals and even biological systems.

### *1.4.2 Experimental observations during martensitic transformation*

If the surface of a crystal of a martensitically transforming material is prepared by polishing while in the austenite phase and then parallel scratches are marked on the surface, it becomes possible to see the effects of martensite formation on cooling. Figure 1.4 shows a schematic diagram of an austenite crystal being cooled below the  $M_s$  temperature. There is a change in direction of the pre-marked scratch in the region that has undergone transformation, as well as an accompanying surface relief effect.

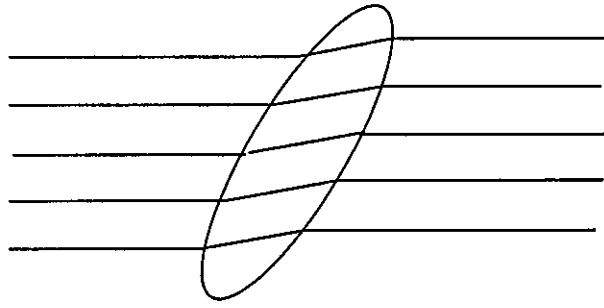


**Figure 1.4:** Schematic drawing of the straight line lines on an austenitic material being diverted by the presence of a martensite plate.

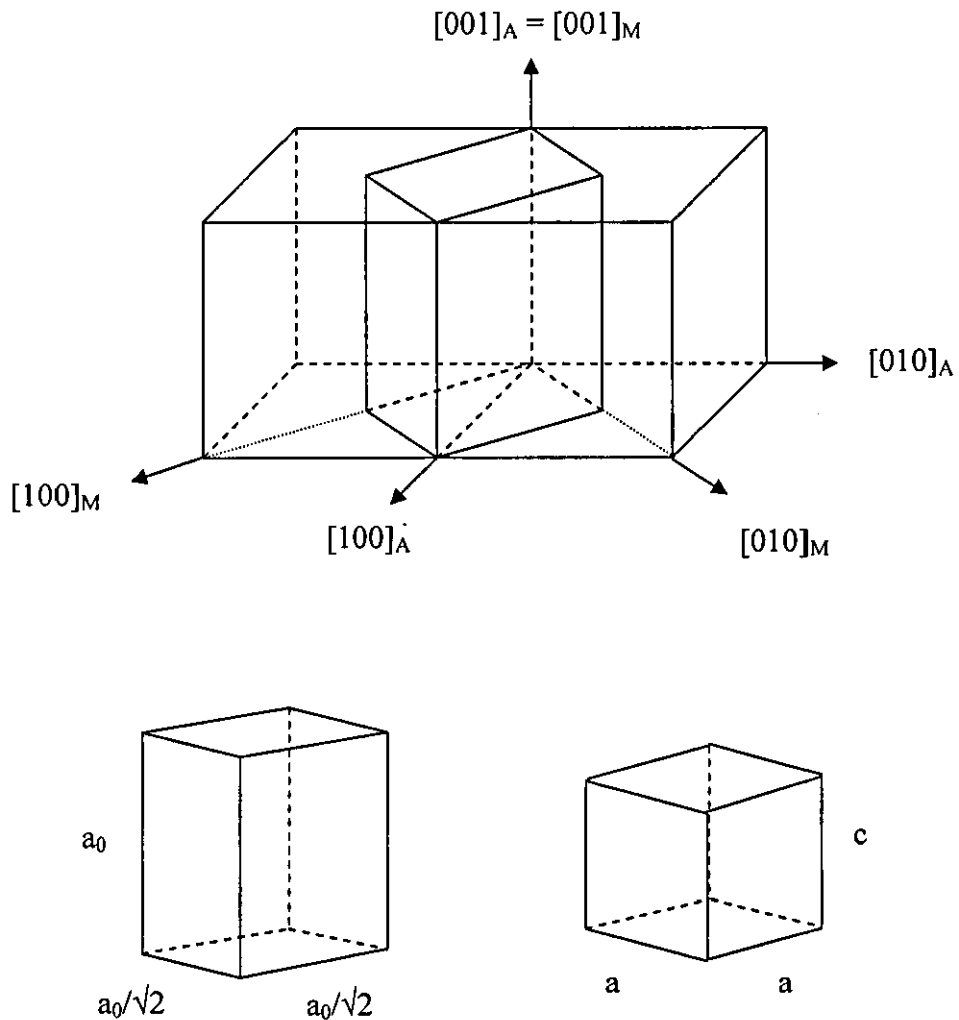


**Figure 1.5:** Diagram illustrating the transformation of the FCC austenite into the BCT martensite. Two FCC unit cells of lattice parameter  $a_0$  can be seen side by side, with a tetragonal unit cell of axes length  $a = b = a_0/\sqrt{2}$ , and  $c = a_0$  delineated. Compression along the  $c$ -axis and expansion of the  $a$ - and  $b$ -axes, results in the formation of the martensite BCT unit cell. Atoms are not included in the diagram for the sake of clarity. After Wayman, 1964.

It can be seen from Figure 1.4 that, on transformation, straight lines are transformed into other straight lines and therefore planes are transformed into other planes. This implies that within the two crystal structures there are certain planes and certain directions which coincide with one another. This is termed the 'orientation relationship' or 'lattice correspondence' and is a feature of all martensitic transformations. It will be further discussed in the next section using the example of martensitic transformation in steel.

It is also the case that the lines are continuous as they traverse the interface. This implies that there is no rotation of the interface plane since if there was, some localised plastic deformation in the region of austenite material close to the habit plane would result in a loss of continuity, i.e. further displacement, of the scratches. Bowles and Mackenzie made these observations in their study of the surface relief in martensitic transformations in 1954, and concluded therefore that the habit plane is unrotated during transformation (Bowles and Mackenzie, 1954, Wayman, 1964b)

In a previous paragraph the habit plane was defined as that on which the martensite plates form. It is a requirement of martensitic reactions that this plane should be undistorted, i.e. that all vectors residing within this plane should be unchanged in magnitude and their angular separation must not change.

Experimentally, the habit plane can be determined by two-surface trace analysis on a suitably polished single crystal, i.e. two surfaces at right angles to each other. The single crystal's orientation should have been determined prior to the experiment using Laue back-reflection X-ray diffraction, for example (Wayman, 1964b). Further diffraction experiments on a not-fully-

transformed crystal allow the orientation relationship, lattice parameters and crystal structures to be determined.

The atomic movements during transformation are very small compared with diffusion and dislocation slip in metals. They are much less than the interatomic distances in the material, although this distance can vary depending on the alloy composition. For example, the atomic movements in Fe-30Ni are large when compared with the atomic movements in an indium-thallium shape memory alloy composed of 18-20 % thallium (Reed-Hill, 1964).

#### *1.4.3 Bain model of martensitic transformation*

In 1924, Edgar C. Bain published a landmark paper in which he proposed that the transformation in steel could be achieved by a expansion of two of the axes in the FCC structure and a shortening of the third (Bain, 1924). Conversion of one crystal into another by expansion or contraction along the principal axes of the unit cell is known as the Bain strain or the Bain distortion. Figure 1.5 illustrates how this can occur, following the approach adopted by Bain. In the figure two unit cells of the austenite phase can be seen side by side with a body-centred tetragonal (BCT) unit cell delineated between them. By expansion of approximately 12 % along the  $a$  and  $b$  axes of the BCT unit cell, i.e. the  $[1 \ -1 \ 0]_A$  and  $[1 \ 1 \ 0]_A$  directions in the original FCC austenite cells, and a contraction of around 20 % along the  $[0 \ 0 \ 1]_A$ , the transformed unit cell (a BCT unit cell) is created (Honeycombe and Bhadeshia, 1995). It can be observed in Figure 1.5 that the lattice correspondence for this particular transformation is as follows:



$$[\frac{1}{2} \ -\frac{1}{2} \ 0]_A // [1 \ 0 \ 0]_M,$$

$$[\frac{1}{2} \ \frac{1}{2} \ 0]_A // [0 \ 1 \ 0]_M,$$

$$[0 \ 0 \ 1]_A // [0 \ 0 \ 1]_M.$$

From this, we can write a matrix which allows the transformation of one direction in the austenite phase  $[u \ v \ w]$  into its equivalent direction in the martensite phase  $[U \ V \ W]$  thus:

$$\begin{pmatrix} u \\ v \\ w \end{pmatrix} = \begin{pmatrix} \frac{1}{2} & \frac{1}{2} & 0 \\ -\frac{1}{2} & \frac{1}{2} & 0 \\ 0 & 0 & 1 \end{pmatrix} \begin{pmatrix} U \\ V \\ W \end{pmatrix}. \quad (1.3)$$

It can therefore be seen that the  $[1 \ 1 \ 1]_M$  direction in the martensite phase corresponds to the  $[1 \ 0 \ 1]_A$  direction in the parent phase, for example. It is also possible to determine the origin of particular planes within the martensite crystal using this coordinate transformation, as follows:

$$\begin{pmatrix} H \\ K \\ L \end{pmatrix} = \begin{pmatrix} \frac{1}{2} & -\frac{1}{2} & 0 \\ \frac{1}{2} & \frac{1}{2} & 0 \\ 0 & 0 & 1 \end{pmatrix} \begin{pmatrix} h \\ k \\ l \end{pmatrix}. \quad (1.4)$$

Where  $H, K$  and  $L$  are the Miller indices of the martensite plane  $(H \ K \ L)$  and  $h, k$  and  $l$  are the Miller indices of the austenite plane  $(h \ k \ l)$ . We can therefore see that the martensite  $(0 \ 1 \ 0)_M$  plane was derived from the  $(1 \ 1 \ 0)_A$  austenite plane, for example, and that the  $(-1 \ 0 \ 1)_M$  is derived from the  $(-1 \ 1 \ 1)_A$  (Otsuka and Wayman, 1998).

In steels, for example, there exists a number of orientation relations dependent upon the relative fractions of iron and carbon. For example, in

low carbon steels, the orientation relationship between the austenite and martensite phases is as follows (the well-known Kurdjumov-Sachs relation):

$$\begin{aligned}\{111\}_A // \{110\}_M, \\ \langle 01-1 \rangle_A // \langle -111 \rangle_M.\end{aligned}$$

With the habit plane being  $\{111\}_A$  (Honeycombe and Bhadeshia, 1995).

It is very important to note that although in this instance the BCT cell was formed via contraction of the  $c$ -axis and expansion of the other two axes, it is possible for the new unit cell to be formed via this contraction along each of the  $c$ -axes in turn, with the associated expansion along the other two. It is therefore said that the BCT martensite has three crystallographically equivalent variants. These are known as the lattice correspondence variants (LCVs) and their number depends on the crystallography of the transformation.

Another concept which is important to define is that of the ‘lattice deformation’ or ‘Bain strain’ matrix, usually given the symbol  $\mathbf{B}$ . This provides the measure of the lattice distortions in the principal strain directions, and requires knowledge of the lattice parameters of both phases. Referring again to Figure 1.5, it can be seen that the distortions,  $\eta_i$  ( $i = 1, 2, 3$ ), required to convert the outlined cell into the martensite BCT cell are, in terms of the lattice parameters of the two phases:

$$\text{In the } a\text{- and } b\text{- directions: } \eta_1 = \eta_2 = \frac{\sqrt{2}a}{a_0}.$$

$$\text{In the } c\text{-direction (i.e. vertically): } \eta_3 = \frac{c}{a_0}.$$

The lattice deformation matrix can therefore be written as:

$$\bar{B} = \begin{pmatrix} \sqrt{2}a/a_0 & 0 & 0 \\ 0 & \sqrt{2}a/a_0 & 0 \\ 0 & 0 & c/a_0 \end{pmatrix}. \quad (1.5)$$

If we wish to write this matrix in with reference to the austenite lattice (the general case) then a coordinate transformation is required as follows:

$$B = R\bar{B}R^T. \quad (1.6)$$

Where  $R$  is the rotation matrix and  $R^T$  is its transpose. For the case shown in Fig. 1.5 it would be as follows (Otsuka and Wayman, 1998):

$$B = \begin{pmatrix} 1/\sqrt{2} & 1/\sqrt{2} & 0 \\ -1/\sqrt{2} & 1/\sqrt{2} & 0 \\ 0 & 0 & 1 \end{pmatrix} \begin{pmatrix} \sqrt{2}a/a_0 & 0 & 0 \\ 0 & \sqrt{2}a/a_0 & 0 \\ 0 & 0 & c/a_0 \end{pmatrix} \begin{pmatrix} 1/\sqrt{2} & -1/\sqrt{2} & 0 \\ 1/\sqrt{2} & 1/\sqrt{2} & 0 \\ 0 & 0 & 1 \end{pmatrix}. \quad (1.7)$$

The problem with the Bain distortion is that, acting on its own, there is no undistorted plane using this approach, i.e. it does not agree with the experimental observations mentioned in the previous section. There is thus no way of predicting the habit plane using this approach. The next section details a theory which makes use of the Bain strain concept but uses other operations in order to bring theory into line with experiment. It is successful in predicting the crystallographic details associated with martensite formation and is known as Wechsler-Lieberman-Read or Bowles-Mackenzie theory.

*1.4.4 Wechsler, Lieberman and Read, and Bowles and Mackenzie theory*

The theories allows the predication of the crystallographic features of the martensitic transformation, such as the habit plane and orientation relationship between the two phases.

The theories were developed by Wechsler, Lieberman and Read, and Bowles and Mackenzie, independently, in 1953 and 1954 respectively (Wechsler et al, 1953, Bowles and Mackenzie, 1954). The two theories are different but were shown to be mathematically equivalent to each other in 1955 by J. W. Christian (Christian, 1955).

Wechsler, Lieberman and Read proposed that the martensitic transformation is composed of a combination of three deformations:

- Bain distortion.
- Lattice invariant shear: can be either slip or twinning. This is required for the habit plane to remain macroscopically undistorted. There will obviously be some kind of localised distortion at the interface but this can be neglected for the length scales discussed here.
- Rigid body rotation: this is required to ensure the undistorted plane is common to both phases.

The theory (and that of Bowles and Mackenzie) is phenomenological. That is, it does not try to describe the physical mechanism of the movement of atoms at the austenite-martensite interface as it sweeps through the crystal. It simply provides the deformations (which need not be applied in the order given above) necessary to create one lattice from another, while remaining

true to the experimental observations. However, the two theories do require certain details to be known *a priori*. These are:

- The lattice parameters of the austenite and martensite phases.
- The nature of the lattice invariant shear, i.e. whether slip or twinning, and either the slip or twinning system.
- The lattice correspondence between the phases.

The theory is usually presented using a matrix formulation as follows. The shape strain is represented as  $\mathbf{P}_1$ , with  $\mathbf{R}$  as the rigid body rotation,  $\mathbf{B}$  the Bain strain matrix (discussed in the previous section), and  $\mathbf{P}$  as the lattice invariant shear. Thus equation 1.8 defines the transformation (Wayman, 1964c) :

$$\mathbf{P}_1 = \mathbf{RBP}. \quad (1.8)$$

## **1.5 Shape memory alloys**

### *1.5.1 Introduction*

Shape memory alloy is the name given to a metallic material which can fully recover a deformation either by heating to a temperature above the austenite finish ( $A_f$ ) temperature, or by removal of the stress. This behaviour is due to the martensitic transformations which occur in these materials. In this section we discuss the origins of this unique behaviour with the emphasis on the NiTi alloy system, discussing the crystal structures, mechanical and thermodynamic behaviour of this material since its study via diffraction techniques makes up the bulk of the thesis content.

### 1.5.2 Thermomechanical behaviour of shape memory alloys

In a first approximation some distinction can be drawn between the strain recovery behaviour exhibited by the material based on the temperature of deformation. Above the  $A_f$  temperature the transformation is induced solely through the action of an applied stress. Removal of this stress removes the driving force for transformation and thus the material transforms spontaneously back to the austenite phase in its original crystal orientation, causing the complete recovery of induced strain. This behaviour is known as *superelasticity* or *pseudoelasticity*. Note that there is a hysteresis in the stress levels for forward and reverse transformation due to the dissipation of energy during the mechanical cycle (see Fig. 1.6).

The other type of behaviour, the *shape memory effect*, results when the material is deformed below the  $M_f$  temperature. Stress-free cooling of the a shape memory alloy results in a martensitic transformation without any change in the macroscopic dimensions in the alloy. This is the result of the twinned microstructure which is formed in under zero stress conditions, as required by the phenomenological theory of martensitic transformation discussed in the previous section. The results of this is the presence of many interfaces due to the fact that all lattice correspondence variants will be present in such a microstructure. These interfaces are highly mobile and, as a result of the twinned microstructure obtainable on cooling thermoelastic alloys, an applied stress results in a detwinning of this structure as a way of generating strain. On heating (above  $A_f$ , as the transformation temperature is usually higher due to the stabilisation of the martensite) the reverse transformation proceeds. Again, this results in the conversion of the martensite variants back to the austenite structure in its original orientation – this crystallographic reversibility allows the strain to be fully recovered. The

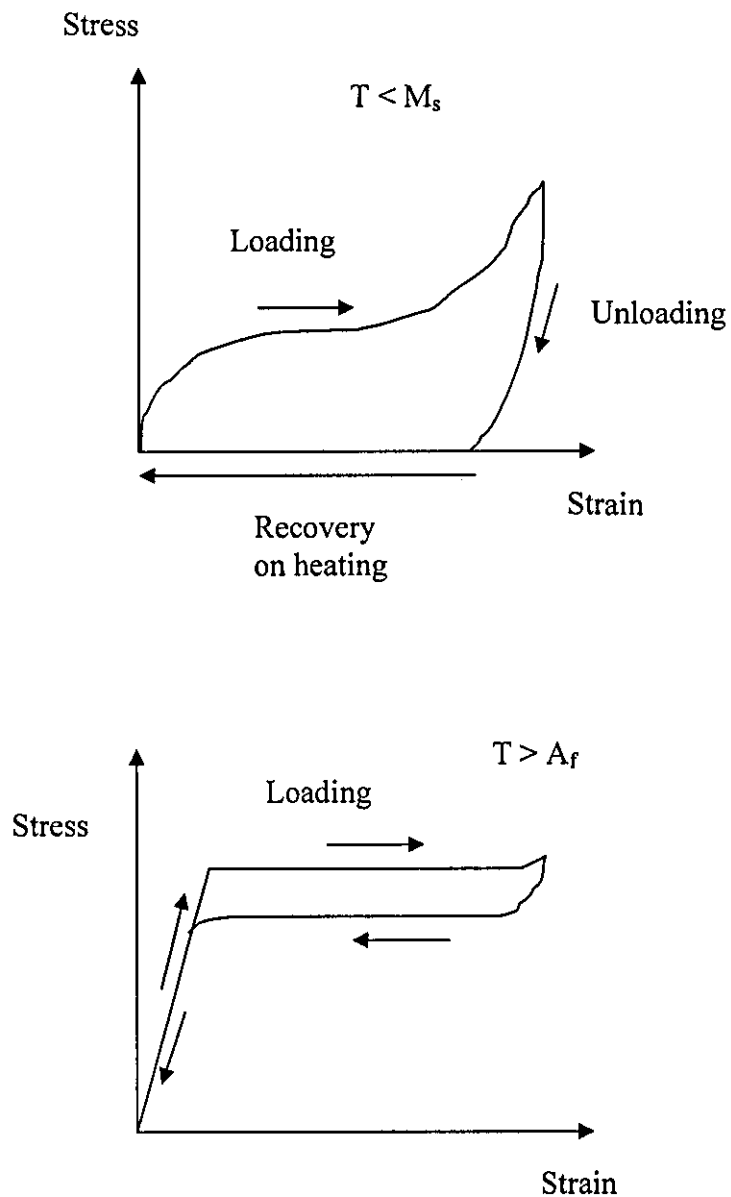


**Figure 1.6:** Schematic diagrams of the shape memory effect and superelasticity occurring in a shape memory alloy. The upper diagram refers to the shape memory effect, with the deformation occurring via variant reorientation at a temperature below  $M_f$ . The lower diagram shows superelastic behaviour. The alloy is in the austenite phase initially and transformation proceeds via the application of stress to a critical level.

crystallographic reversibility is due to the thermoelastic nature of the transformation. Schematic diagrams of superelasticity and the shape memory effect are shown in Figure 1.6 for a generic shape memory single-crystal. Such transformation mechanisms allow the recovery of large strains in both single- and poly-crystals, ranging anywhere from zero to around 15 %. Some example of materials exhibiting martensitic transformation, along with appropriate compositions and rough values for the hysteresis, are given in Table 1.2.

The shape memory effect was first discovered in an Au-Cd alloy in 1951 by Chang and Read (Chang and Read, 1951). However, it was not until its discovery in the Ni-Ti system by Buehler, Gilfrich and Wiley in 1963 that the effect became more widely publicised (Buehler et al, 1963). The appropriate composition to observe shape memory behaviour in a NiTi alloy is a nickel content of 49-51 at.%.

In shape memory alloys, stress-free cooling results in a transformation occurring without any macroscopic distortion of the alloy, i.e. there is no change in dimensions in the material.

Thermodynamic properties of shape memory alloys, such as the transformation temperatures,  $A_f$ ,  $M_s$ , etc, are easily measured. Since the transformation is first-order a latent heat is released on cooling (an exothermic reaction) and on heating, transformation heat is absorbed during the endothermic reaction. The most popular method of determining thermodynamic parameters associated with the transformation is via calorimetry work, usually differential scanning calorimetry (DSC).



Alloy	Composition (at.%)	Structural change	Hysteresis [K]
Ag-Cd	44-49 Cd	B2 $\leftrightarrow$ 2H	~ 15
Au-Cd	46.5-50 Cd	B2 $\leftrightarrow$ 2H	~ 15
Cu-Zn	38.5-41.5 Zn	B2 $\leftrightarrow$ 9R	~ 10
Cu-Zn-X (X = Si, Sn, Al, Ga)	Several at. %	B2 $\leftrightarrow$ 9R	~ 10
Cu-Al-Ni	28-29 Al 3-4.5 Ni	DO <sub>3</sub> $\leftrightarrow$ 2H	~ 35
Cu-Sn	~15 Sn	DO <sub>3</sub> $\leftrightarrow$ 2H, 18R	-
Cu-Au-Zu	23-28 Au 45-47 Zn	Heusler $\leftrightarrow$ 18R	~ 6
Ni-Al	36-38 Al	B2 $\leftrightarrow$ 3R	~ 10
Ni-Ti	49-51 Ni	B2 $\leftrightarrow$ B19' B2 $\leftrightarrow$ P-3	~ 20-100 ~ 1-2
In-Tl	18-23 Tl	FCC $\leftrightarrow$ FCT	~ 4
In-Cd	4-5 Cd	FCC $\leftrightarrow$ FCT	~ 3
Fe-Pt	~ 25 Pt	L1 <sub>2</sub> $\leftrightarrow$ BCT	small
Fe-Pd	~ 30 Pd	FCC $\leftrightarrow$ FCT	small

**Table 1.2:** A list of some common shape memory alloys and their compositions, transformation crystallography and approximation of the temperature hysteresis invloved. Data taken from Miyazaki and Otsuka, 1989.

Alternatively, the transformation temperatures can be determined by measuring resistivity changes in the material during cooling and can be used to determine the type of structural change occurring (Liu et al, 1997). Resistance measurement and DSC are the most popular methods of determining the transformation temperatures in shape memory alloys.

### *1.5.3 Calculation of strain generated due to transformation*

The generated strain due to martensitic transformation is anisotropic and thus varies with crystal orientation. The strain generated is predictable based on the experimental observation that a large enough applied stress will result in the formation of a single martensitic variant. There are several methods by which the strain can be determined. It can be calculated from the plateau length in single crystal deformation experiments or can be calculated based on the known structural changes occurring during transformation (see Otsuka and Wayman, 1998b, for example). Since it is possible to determine the correspondent lattice planes during transformation via an equation similar to that given in eqn. 1.4 for steel materials, the d-spacing of these planes may be used to calculate to strain generated on full transformation to a particular variant.

For example, based on the lattice correspondence between the austenite and B19' martensite unit cells, it can be calculated that in the diffraction experiment the  $(100)_A$  austenite peak is constrained by the transformation crystallography to transfer intensity to two martensite peaks only: the  $(011)_M$  peak at  $\sim 3.07$  Angstroms (corresponding to 8 variants, which are indistinguishable from one another) and the  $(100)_M$  at  $\sim 2.86$  Angstroms (4 variants, which are again indistinguishable in the diffraction experiments).

Given that the lattice parameter for the austenite phase is 3.015 Å, the strain can be calculated from the positions of these reflections as  $(d_M - d_A)/d_A$ . Thus, in diffraction experiments, growth of the  $(011)_M$  martensite peak results in the generation of approx. 5.1 % tensile strain. In the case of growth of the  $(100)_M$  peak, compressive strain of approx. -1.7 % is generated. This calculation can be repeated for all other reflections in the diffraction spectrum and thus the strain associated with the formation of particular martensitic variants calculated. It is used in all subsequent chapters in order to determine strain values associated with the formation of specific peaks.

## 1.6 Physical metallurgy of NiTi: crystal structures and phase diagram

The shape memory alloy NiTi is the main material studied within this thesis. In solution heat treated form the transformation occurs between two phases the austenite phase which has an ordered BCC structure with lattice constant  $a_0 = 3.015$  Å (space group Pm-3m). The ordered structure of the austenite phase is referred to as B2 in *strukturbericht* notation (for an explanation of *strukturbericht* notation the reader is referred to the *International Tables for Crystallography*, Kluwer Academic Publishers, Dordrecht, The Netherlands).

The martensitic phase is denoted B19' and has a monoclinic crystal structure, with space group of P2<sub>1</sub>/m. The lattice parameters, obtained from the structure refinement work of Kudoh et al, are as follows:  $a = 2.898$ ,  $b = 4.108$ ,  $c = 4.646$  with  $\beta = 97.78^\circ$  (Kudoh et al, 1985).

The phase diagram associated with Ni-Ti alloys is shown in Figure 1.7.

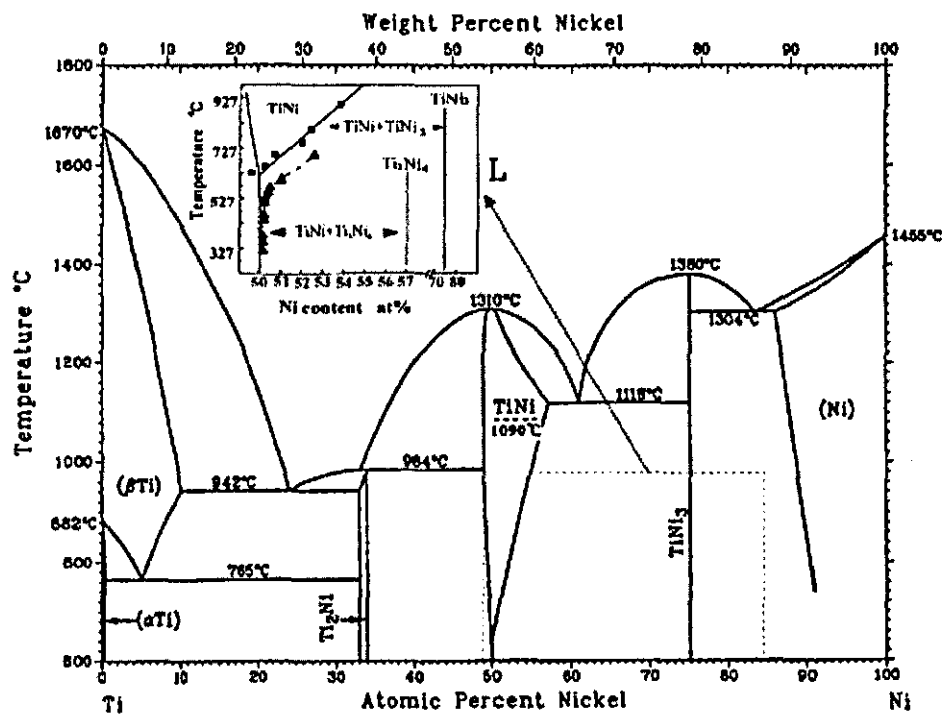


**Figure 1.7:** Ni-Ti alloy phase diagram after Massalski (Binary alloy phase diagrams (2<sup>nd</sup> edition, vol. 3, ASM International, (1990), p. 2874). Reproduced from Otsuka and Ren (*Progress in Materials Science*, 50, (2005), 511-678.

## 1.7 References

Ashby, M. F., and Jones, D. R. H., *Engineering Materials 2*, Butterworth-Heinemann, Oxford, UK, (1998).

Bain, E. C., *Trans. AIME*, 70, (1924), 25.

Bhadeshia, H. K. D. H., *Worked Examples in the Geometry of Crystals*, The Institute of Materials, UK, (2001), 51.

Bhadeshia, H. K. D. H., <http://www.msm.cam.ac.uk/phase-trans/2002/martensite.html>, 2002.

Bowles, J. S., and Mackenzie, J. K. *Acta Metallurgica*, 2, (1954), 129.

Buehler, W. J., Gilfrich, J. W., and Wiley, R. C., *Journal of Applied Physics*, 34, (1963), 1475.

Chang, L. C., and Read, T. A., *Trans. AIME*, 189, (1951), 47.

Christian, J. W., in E. R. Petty (Ed.), *Martensite: Fundamentals and Technology*, Longmans, (1970).

Christian, J. W., *Journal of the Institute of Metals*, 84, (1955), 386.

Honeycombe, R. W. K., and Bhadeshia, H. K. D. H., *Steels: Microstructure and Properties*, Butterworth-Heinemann, Oxford, UK, (1995), 83-114.

Kaufmann, L., and Cohen, M., *Progress in Metal Physics*, 7, (1958), 165.

Kessler, H., and Pitsch, W., *Acta Metallurgica*, 15, (1967), 401.

Kudoh, Y., Tokonami, M., Miyazaki, S., and Otsuka, K., *Acta Metall.*, 33, (1985), 2049.

Kurdjmov, G. V., and Khandros, L. G., *Dokl. Nauk SSSR*, 66, (1949) 211.

Liu, Y., Van Humbeeck, J., Stalmans, R., Delaey, L., Some aspects of the properties of NiTi shape memory alloy, *Journal of Alloys and Compounds*, 247, (1997), 115-121.

Machlin, E. S., and Cohen, M., *Trans. AIME*, 194, (1952), 489.

Otsuka, K., and Wayman, C. M., Introduction, in K. Otsuka and C. M. Wayman (eds.), *Shape Memory Materials*, Cambridge University Press, (1998a), 22-23.

Otsuka K. and Wayman C. M., Stress-induced martensitic transformation and superelasticity, in K. Otsuka and C. M. Wayman (eds.), *Shape Memory Materials*, Cambridge University Press, (1998b), 27-48.

Reed-Hill, R. E., *Physical Metallurgy Principles*, D. Van Nostrand Company Ltd, (1964), 399-438.

Rock, P. A., *Chemical Thermodynamics*, Oxford University Press, (1983), 276.

Tong, H. C., and Wayman, C. M., *Acta Metallurgica*, 22, (1974), 887.

Wayman, C. M., and Duerig, T. W., An Introduction to Martensite and Shape Memory, in T. W. Duerig, K. N. Melton, D. Stockel and C. M.

Wayman (Eds.), *Engineering Aspects of Shape Memory Alloys*, Butterworth-Heinemann, (1990), 15.

Wayman, C. M., *Introduction to the Crystallography of Martensitic Transformations*, The Macmillan Company, (1964), 85.

Wayman, C. M., *Introduction to the Crystallography of Martensitic Transformations*, The Macmillan Company, (1964b), 76-83.

Wayman, C. M., *Introduction to the Crystallography of Martensitic Transformations*, The Macmillan Company, (1964c), 84-97.

Wechsler, M. S., Lieberman, D. S., and Read, T. A., *Trans. AIME*, 197, (1953) 1503.

Miyazaki, S., and Otsuka, K., Development of Shape Memory Alloys, *ISIJ International*, 29(5), (1989), 353-377.

## **Chapter 2:**

# **Introduction to internal strain measurement by diffraction techniques**

### **2.1 Introduction**

Internal stress measurements are best conducted using beams of radiation. Typically these measurements are made using synchrotron X-rays or neutrons. Some significant advantages are offered over conventional strain measurement methods such as resistance strain gauges, not least of which is the ability to provide accurate depth-resolved strain non-destructively. Strain determination by diffraction methods rely on precise measurements of the lattice parameters or Bragg reflection positions by fitting a known function which approximates the shape of the peak.

The technique is now so well developed that a standard has been developed under the auspices of the Versailles Project on Advanced Materials and Standards (VAMAS) in order to provide the engineering community with confidence in the accuracy of the technique and standardise the measurements made at different locations.

### **2.2 Diffraction**

#### *2.2.1 Introduction to diffraction and Bragg's law*



The utility of the diffraction technique is great, with it having application in many diverse field such as biology, chemistry, physics, engineering and even archaeology.

Diffraction phenomena rely on the coherent scattering by a large scale, regular array of scattering centres, which in the scientific fields will generally be atoms.

Materials to be studied by diffraction methods are required to be crystalline in nature, that is to say that they must have a regularly repeating pattern, called the *space lattice* or *Bravais lattice*, with which the array of scattering centres – an arrangement of atoms, known as the *basis* – can be associated (Blakemore, 1985). There are a total of 14 Bravais lattices, all of which are based on seven geometric shapes known as *crystal systems* or *unit cells*. Knowledge of the crystal system is all that is required to determine the approximate position of Bragg reflections. Intensity is dependent upon the atomic arrangement within the unit cell (Clegg, 1998).

The seven possible crystal systems are: Cubic, trigonal, hexagonal, tetragonal, orthorhombic, monoclinic, and triclinic. A unit cell is defined by the length of its lattice vectors and interior angle. The axial parameters associated with each unit cell are detailed in Table 2.1.

In fact, much information can be gleaned from external examination of a samples morphology, since the underlying symmetry on a microscopic level is the same as that observed on the macroscale. Early crystallographers often conducted their investigations into crystal structures of minerals in this way. However, this is often qualitative and to truly understand the arrangement of atoms within a material a technique with resolution sufficient to resolve

Crystal system	Lattice parameters
Cubic	$a = b = c$ $\alpha = \beta = \gamma = 90^\circ$
Trigonal (rhombohedral/hexagonal)	$a = b = c$ $\alpha = \beta = \gamma \neq 90^\circ$ (rhom.) $a = b \neq c$ $\alpha = \beta = 90^\circ; \gamma = 120^\circ$ (hex.)
Hexagonal	$a = b \neq c$ $\alpha = \beta = 90^\circ; \gamma = 120^\circ$
Tetragonal	$a = b \neq c$ $\alpha = \beta = \gamma = 90^\circ$
Orthorhombic	$a \neq b \neq c$ $\alpha = \beta = \gamma = 90^\circ$
Monoclinic	$a \neq b \neq c$ $\alpha = \gamma = 90^\circ; \beta > 90^\circ$
Triclinic	$a \neq b \neq c$ $\alpha \neq \beta \neq \gamma$

**Table 2.1:** The seven possible crystal systems and associated lattice parameters.

atoms typically no more than 1 Angstrom apart is required. For this diffraction is generally used, with the penetrating radiation having a wavelength of the order of the separation of the objects being studied.

The fundamental equation of diffraction phenomena is Bragg's law, given in equation 2.1:

$$n\lambda = 2d_{hkl} \sin \theta_{hkl}. \quad (2.1)$$

Where  $\lambda$  is the wavelength of the radiation,  $d_{hkl}$  the d-spacing of a Bragg peak within the diffraction spectra and  $\theta_{hkl}$  is half of the diffraction angle,  $2\theta_{hkl}$ . The diffraction order is given by  $n$  which can be equal to 1, 2, 3, etc. The Miller index notation  $h$ ,  $k$  and  $l$  is used to identify the planes being studied.

Equation 2.1 can be derived by considering the construction shown in Figure 2.1. This shows the geometry of the diffraction phenomena by considering the incident radiation as beams travelling in straight lines (geometrical optics). The construction is due to W. L. Bragg and W. H. Bragg (his father). The rays are considered to undergo specular reflection, i.e. the angle of incidence is equal to the angle of reflection. For constructive interference to take place the reflected beams must all be in phase, thus the path difference between waves reflected from parallel planes must be equal to an integral number of wavelengths, i.e. equal to  $n\lambda$ .

Thus a conventional diffraction experiment would involve a sample being immersed in radiation of a known wavelength while a detector scans in  $2\theta$ .

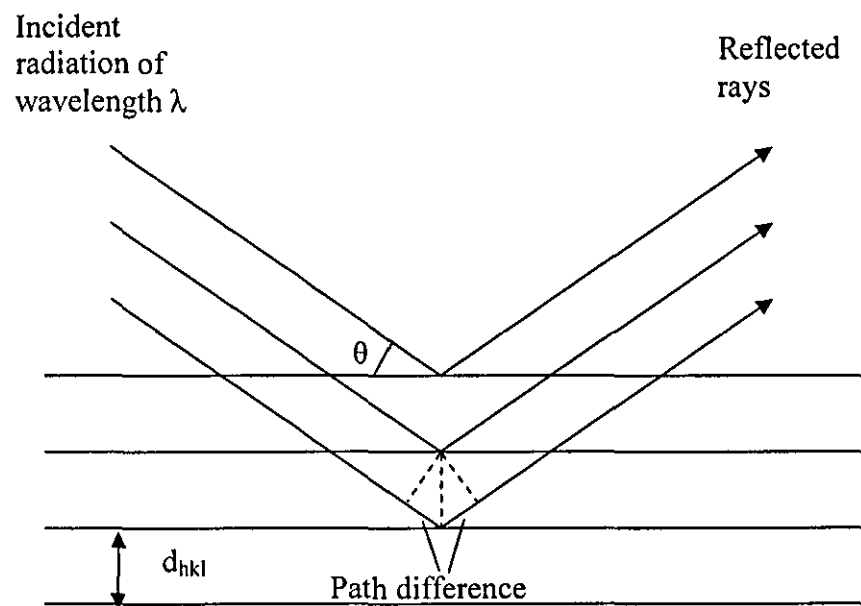


**Figure 2.1:** Bragg construction for rays of incident radiation reflected from parallel planes. From the figure the path difference between waves of equal phase can be calculated as  $2d_{hkl} \sin \theta$ . Thus for constructive interference to occur, this path difference must be equal to an integral multiple of the incident radiation wavelength,  $\lambda$ .

### *2.2.2 Neutron diffraction*

Many types of radiation can be used in diffraction experiments, most commonly the favoured ones are X-rays and neutron since these are available with wavelengths which are of the order of interatomic separation. Neutrons are used exclusively in the work discussed within this thesis and therefore they are the main focus of the following.

Neutrons are electrically neutral and have magnetic spin. They are therefore useful for the study of magnetic structure as well as atomic structure.

Neutrons are generally only available at large-scale facilities such as the Institute Laue-Langevin (ILL) in Grenoble and the ISIS facility at the Rutherford Appleton Laboratory, in Oxfordshire, England, due to the large cost and amount of technical staff required to run reactors. Both facilities are however fundamentally different due to the way in which they supply neutrons. The ILL is a reactor-based source of neutrons while ISIS is a spallation neutron source.

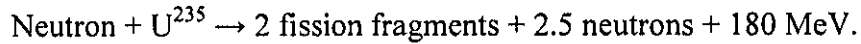
There are few natural processes by which neutrons may be formed, although they can be produced by fusion processes in stars, for example (Carlile, 2002). The production of neutrons for the purposes of scientific experiments and the associated instrumentation at these facilities are now discussed.

### *2.2.3 Reactor neutron sources*

Reactor neutron sources utilise nuclear reactors optimised for the maximum production of neutrons for the minimum amount of heat. This is the direct

opposite to the goal of those used in the power industry, where the generation of heat is the main goal. Hence those engaged in production of neutrons for scientific experiments are known as *research reactors* (Krawitz, 2001).

The neutrons are generally produced by the fission of uranium-235 with an average of approximately 2.5 high-energy neutrons produced per fission. The average reaction proceeds as follows:



For every five neutrons produced this way, two are used to begin another fissile process (one each), with one being lost through absorption in other material, and two being liberated from the reactor core for use in experiments. Thus the reaction is self-sustaining (Carlile, 2002).

The wavelengths of neutrons emerging from these types of reactors has a Maxwellian profile, thus there are a great many neutrons of different wavelengths within the beam emerging from the reactor. The characteristic temperature of the distribution governs the velocity of the neutrons. For neutrons of use in diffraction experiments this temperature is around 300 K, or roughly room temperature. Hence the neutrons used in diffraction experiments are known as thermal neutrons.

Such sources are generally used to provide neutrons of a single wavelength for use in diffraction experiments (an exception to this is the IBR-II facility in Russia which runs in time of flight mode). This selection of a single wavelength from the flux profile emerging from the reactor is achieved through diffraction from a suitably cut single crystal, usually silicon or

germanium, placed along the beam-path. Thus in order to satisfy Bragg's law the experimental set-up generally consists of a detector which scans in increments of  $2\theta$  while the sample rotates in-step in increments of  $\theta$ .

Figure 2.2 shows the typical experimental arrangement at a reactor source, where the purpose of the experiment is to measure internal strain within the sample.

A typical residual strain measurement experiment requires the determination of the lattice parameter or reflection position within a certain region of the sample, this is known as the gauge volume, and the strain calculated is the average over this volume (usually several cubic millimetres).

A diffraction spectrum collected at a reactor-based source of neutrons will consist of a table of intensity versus  $2\theta$ . Thus the fitting of peaks within this spectrum will yield peak positions in units of  $2\theta$ . Strain,  $\varepsilon$ , from this information is worked out via the derivative of Bragg's law, which after rearrangement can be written:

$$\varepsilon = \frac{\Delta d}{d_{hkl}^0} = -\Delta\theta \cot \theta. \quad (2.2)$$

Where  $\Delta\theta = \theta_{hkl} - \theta_{hkl}^0$  and is the difference in value of half the scattering angle for the unstressed peak,  $\theta_{hkl}^0$ , and the stressed peak,  $\theta_{hkl}$ .

Some measurements made using a steady state neutron source – the RESidual Stress and Texture diffractometer (REST), situated near Nykoping in Sweden – are discussed in a later chapter in this thesis.

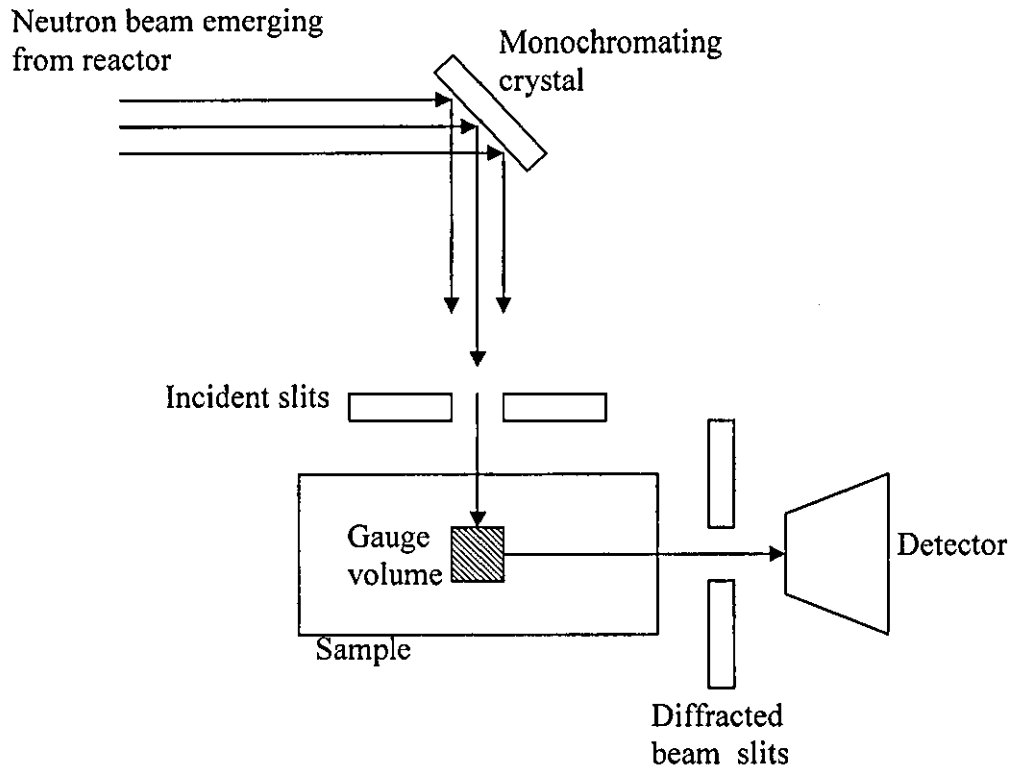


**Figure 2.2:** Typical experimental arrangement for a strain scanning experiment at a steady state reactor source. The neutrons emerging from the reactor are diffracted by the monochromating crystal (typically silicon or germanium) so that radiation of a nominally single wavelength impinges on the sample. The incident and diffracted beam slits define the size of the region irradiated. This is known as the gauge volume. Experimentally, the detector will be able to scan in  $2\theta$  while the sample rotates in step but in increments of  $\theta$ .



#### *2.2.4 Spallation neutron sources*

The main neutron source used in the work described in this thesis is the ISIS spallation neutron source in Oxfordshire (Wilson, 1995). Production of neutrons at ISIS begins initially with hydrogen ions accelerated by a linear accelerator operating at a frequency of 50 Hz and therefore with pulses of ions occurring every 20 ms.

These have their electrons removed from them by passage through thin alumina foil ( $\text{Al}_2\text{O}_3$ ), the remaining protons are then accelerated to energies of around 800 MeV by a synchrotron. Typically there are about  $2.5 \times 10^{13}$  protons per pulse. The protons are then impacted onto a heavy metal target made of tantalum. The incident protons form a 'compound' with the nuclei of the target material and the target nucleus is set into an excited state. The by product of the de-excitation of the nucleus is the production of neutrons, plus several other particles such as neutrinos. This process is called spallation, with the net result that around 20-30 neutrons are produced per proton incident upon the target. The fast neutrons that emerge via this process are too high in energy for use in diffraction experiments are therefore moderated, i.e. reduced in energy, prior to their admission onto the various beamlines available (Carlile, 2002).

The type of diffraction work carried out at spallation sources is commonly known as time-of-flight diffractometry. As the name implies, the basis of this technique is the accurate determination of the velocities of scattered neutrons.

These types of sources offer a reduced amount of neutrons (neutron flux), however, in comparison with the steady-state reactor sources.

The measurement of diffraction patterns at a spallation neutron source is fundamentally different due to the strong intensity of most wavelengths of neutrons in the incident flux profile. This is referred to as a white beam. In contrast to the operation of diffractometers at steady-state neutron sources, where a single wavelength (or at least a narrow band of wavelengths) is used, at a spallation source, use is made of the entire incident flux profile.

The neutrons produced by the spallation process have a range of velocities and therefore wavelengths. Wavelength and velocity are related by the de Broglie relation:

$$\lambda = \frac{h}{mv}, \quad (2.3)$$

Where  $h$  is Planck's constant,  $m$  the neutron mass which is equal to  $1.67 \times 10^{-27}$  kg (Rauch and Waschowski, 2002),  $\lambda$  is the wavelength and  $v$  is the velocity of the neutron.

The spallation process creates all of the neutrons within a pulse at the same time, thus by knowledge of the length of the beam path from source to detector,  $L$ , and by using a detector to determine the neutron flight times,  $t$ , it is possible to relate time of flight with d-spacing as follows.

Substitution of  $v = L/t$  into equation 2.3 gives:

$$\lambda = \frac{ht}{mL}. \quad (2.4)$$

Substitution of equation 2.4 into Bragg's law (equation 2.1) leads to:

$$\frac{ht}{mL} = 2d_{hkl} \sin \theta, \quad (2.5)$$

which can be rearranged to give:

$$t = \frac{2d_{hkl} \sin \theta mL}{h}. \quad (2.6)$$

Substitution of known constants leads to:

$$d = \frac{t}{505.55L \sin \theta}. \quad (2.7)$$

It can be seen that time of flight is therefore proportional to d-spacing.

Thus we can rewrite Bragg's law in following form (Wilson, 2002):

$$\lambda_{hkl} = 2d_{hkl} \sin \theta, \quad (2.8)$$

implying that the diffraction angle  $2\theta$  stays fixed during diffraction and that scanning therefore take place in  $\lambda$  as opposed to  $\theta$ . Scanning in wavelength is the equivalent of scanning in time-of-flight,  $t$ , since they are proportional to each other and therefore strain is calculated via equation 2.4 as:

$$\varepsilon = \frac{d_{hkl} - d_{hkl}^0}{d_{hkl}^0} = \frac{t_{hkl} - t_{hkl}^0}{t_{hkl}^0}. \quad (2.9)$$

## **2.3 The ENGIN-X diffractometer**

The main instrument used in the work contained within this thesis is the ENGIN-X instrument based on the ISIS beamline in Oxfordshire (Dann et al, 2003). A schematic diagram of the instrument is shown in Figure 2.3. The instrument is the successor to the ENGIN instrument at ISIS (Johnson et al, 1997) which had the distinction of being the first instrument at a spallation neutron source to be dedicated to strain measurement when it was constructed in 1994 (Hutchings et al, 2005).

### *2.3.1 Sample positioning*

Samples are mounted on a table which is capable of linear movements in the x-y-z direction and also rotation. The table is capable of moving a 500 kg sample a maximum of 250 mm in the x- and y-directions (horizontal plane), 600 mm in the z-direction (vertically) and performs a maximum rotation of 370 ° (Hutchings et al, 2005).

A long beamline is used which measures approximately 50 m. The longer beamline length optimises the resolution of the diffraction spectra without adversely affecting the intensity and increasing measurements times to impracticable lengths. Such an arrangement is the optimum one for strain measurement instruments based on the Figure of Merit concept developed by Daymond and Johnson (Johnson and Daymond, 2002).

### *2.3.2 Detectors*

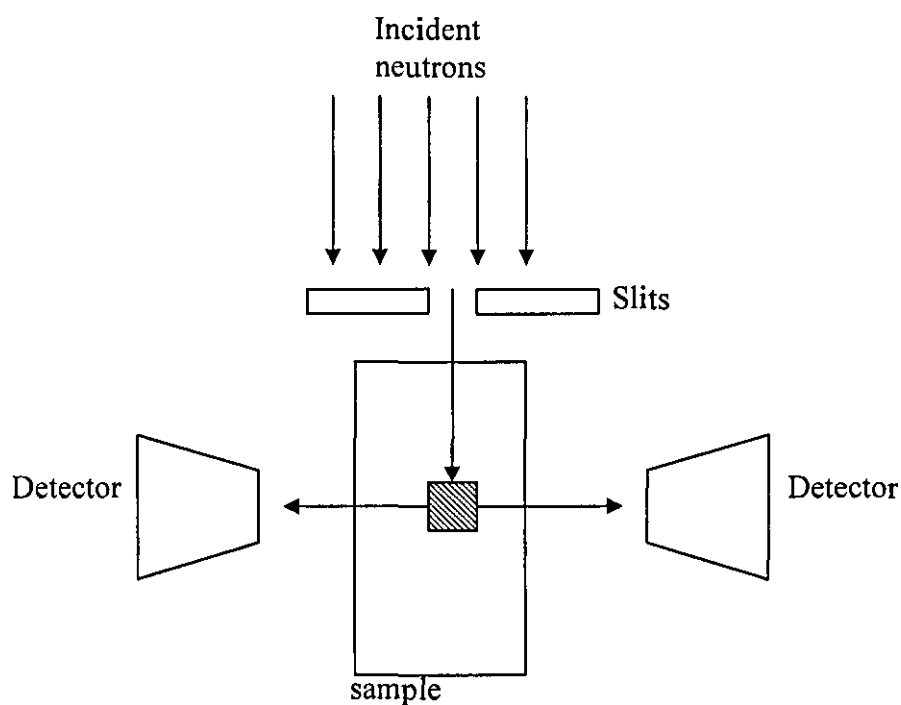


**Figure 2.3:** Typical experimental arrangement of the ENGIN-X diffractometer at the ISIS spallation neutron source. Due to the incident neutrons having a range of velocities, the detectors may recorded a full diffraction profile while maintaining a fixed scattering angle. On ENGIN-X the detectors have radial collimators attached and thus no slits are required for the diffracted beam. The shaded area is the gauge volume.

The two detectors shown in Figure 2.3 are actually composed of banks of scintillator detectors which measure time-resolved spectra. In order to minimise counting times the detectors actually subtend an angle of approximately 15 degrees at the sample position with radial collimators used in front of detector elements used to define the gauge volume (Withers et al, 2000). The differences in flight path and diffraction angle are corrected by computer program and the spectra from all detectors elements added to given the measured diffraction pattern. Several types of collimators are available which allows the exit beam width to be varied between 0.5 to 5 mm in width.

Strain measurements made at a spallation source are generally made using 2 fixed detectors at  $\pm 90^\circ$  to the incident beam. The usual arrangement is that these detectors are fixed in position, and thus two perpendicular strain components can be determined at the same time. This is the set-up on ENGIN-X and for example the SMARTS strain instrument at the Los Alamos National Laboratory in New Mexico.

### *2.3.3 Beam slits*

The incident beam slits are made of boron carbide, which strongly absorbs neutrons, and are capable of reducing the incident beam to one of dimensions 0.3-20 mm in the vertical direction and to a width of 0.3-10 mm (Hutchings et al, 2005). As mentioned in the previous section, exit slits are not required due to the radial collimators placed in front of the detectors. Such a set-up allows a minimum gauge volume of sub-1 mm<sup>3</sup> to be realised for experiments requiring the highest spatial resolution.

### *2.3.4 Stress rig*

Measurements of interior strain in samples while they are undergoing mechanical testing is becoming an increasingly popular method. This is known as *in-situ* diffraction. The large space capacity usually reserved for engineering components is used in this case to allow a full-scale stress rig to be placed on the beamline. On ENGIN-X this is a bespoke rig built by Instron and is capable of operating in stress or strain control, or in fatigue mode if required, with a loading capacity of 50 kN. The rig is controlled by computer and can be synchronised with the diffraction spectra collection program to enable loading experiments to run automatically. The usual set-up is for the rig to be oriented at an angle of 45 degrees to the incident beam. Thus, in this set-up, strain is measured both in the direction of the applied stress (the axial direction) and perpendicular to the applied stress, denoted the radial direction for a cylindrical sample. Such an experimental set-up is the main one used in the work in subsequent chapters of the thesis.

## **2.4 Strain measurement using neutrons**

### *2.4.1 Types of stresses evaluated*

We draw a distinction between the type of stresses which we can measure via the fitting of diffraction peaks. These are classified as type I, type II and type III stresses:

- Type I stresses are known as macrostresses. These generally have length scales comparable with the dimensions of the sample under test. In this case the peak shift is assumed to correspond to the

average macroscopic strain within an area defined by the gauge volume. This type of measurement can be affected by the intergranular strains which generally develop in polycrystalline engineering materials.

- Type II are classified as microstresses and are otherwise known as intergranular stresses. They have a length scale corresponding the grain size of the material under test. In a diffraction experiment, they represent the average stress developed by grains of the same orientation, i.e. parallel scattering vectors. Thus it is common to refer to these grains as a family, as in the (100) grain family for example.
- Type III are also known as microstresses but act over distances comparable with interatomic distances. Thus, defects such as, say, dislocations and interstitial atoms are the cause of these types of stress. Their effect on diffraction patterns is a broadening of the profile. There are some methods of measuring the dislocation density/plastic strain associated with deformation, based on the widths of measured peaks (see, for example, Swallowe et al, 1996).

#### *2.4.2 Strain scanning*

The technique of strain measurement was first developed in the 1980s with notable contributions from Allen et al, 1981; Krawitz et al, 1981; and Pintschovius et al, 1981. The technique is founded on the principle that the atomic lattice may be used as a strain gauge to measure the elastic strain within materials.



The aim of these early contributions was to map the residual strain fields in materials. A residual strain or residual stress is a self-equilibrating internal strain/stress which exists within a material which has no external forces acting upon it (Mura, 1987). Residual stresses are generally classified as type I stresses. Knowledge of the magnitude of residual stress is of great importance to the engineering industry since it can have a strong effect on, for example, the fatigue lifetime. The important point is that the stress is always due a difference in the shape between the constituent parts (e.g. grains in a polycrystal) giving rise to what is known as a misfit stress.

Residual stresses may be brought about by various means such as shot peening, i.e. bombarding a material with metal shot to create plastic deformation near the surface. Peening treatments are generally beneficial to the life of a product since they create a compressive stress field close to the surface which prevents cracks forming on the surface. Other residual stresses are however detrimental to the lifetime of a product and therefore a quantitative measurement of residual stresses is always of use to the engineer.

The early experiments relied on mapping the residual strain through translation of the gauge volume through the material. This type of approach is known as *strain scanning*, and the diffraction method is used to provide a value of the internal stress, via measurement of strain, acting at a point – or more accurately a finite volume of material around that point (equal in size to the gauge volume).

Typically the sample is required to be reoriented so that the strain component can be measured in several directions in the sample in order that the stress tensor can be fully defined. Many engineering components,

however, are of a shape such that measurements can be made in the directions of the principal stresses and therefore the sample is only required to be reoriented 3 times in order to do this.

Some examples of strain scanning experiments are as follows: to provide depth-resolved measurements of the residual stress field in shot-peened components (Wang et al, 1996); measurements of residual strain after TIG welding (Prime et al, 2001; Owen et al, 2003) and the effects of post-weld heat treatments (Preuss et al, 2002).

The technique has developed rapidly over the years and is now well-established with a number of conferences, such as the MECASENS series of conferences, publishing proceedings containing papers on all aspects of instrumentation, measurement techniques, data analysis and interpretation, related to the technique. The standard prepared by the VAMAS group (Webster, 2001) has given the engineering community increased confidence in the method and, with the decreasing measurement times now available, private commercial research is being carried out on instruments at large scale facilities.

#### *2.4.3 Lattice strain in polycrystals under loading*

More recently, the strain measurement technique has been extended to include measurements of the internal strain evolution in-situ during mechanical testing in polycrystalline materials. These studies have particularly focussed on the generation of intergranular (type II) strains during the elastic and plastic deformation due to the differential mechanical behaviour of grains of different orientation.

In general, when a diffraction measurement is made with the sample being loaded in its elastic regime, it will be observed that the lattice strain generated for individual reflections will be proportional and have a linear relationship with the applied stress. However the magnitudes of these shifts will differ for different grain orientations. Such behaviour is known as elastic anisotropy and is due to the difference in elastic constants of the material. These are dependent upon the crystal structure of the material in question and there can be as many as 36 independent elastic constants in the case of triclinic crystal. Fortunately, it is often the case that most engineering materials are either cubic or hexagonal. This reduces the number of independent elastic constants to 3 in the case of cubic materials.

The measured gradients from plots of the applied stress versus lattice strain are referred to as diffraction elastic constants (DECs) and while they can be close to the single crystal elastic constants measured in the same direction, they generally differ in value. This is due to the deformation taking place under the constraints of the surrounding grains while in the polycrystalline state (Hutchings et al, 2005b).

For a standard in-situ experiment, conducted with a uniaxially applied stress, strain in both the axial direction and the radial direction is measured. This leads to the measurement of two separate DECs for grain families measured from linear fits to plot of the applied stress versus axial lattice strain,  $\epsilon_{axial}^{hkl}$ , and radial lattice strain,  $\epsilon_{radial}^{hkl}$ , respectively. The DECs are known as the diffraction Young's modulus,  $E_{hkl}$ , and the diffraction Poisson's ratio,  $\nu_{hkl}$ . These are determined from equations (2.10) and (2.11):

$$\sigma_{app} = E_{hkl} \epsilon_{axial}^{hkl} \quad (2.10)$$

and

$$\nu_{hkl} = -\frac{\epsilon_{radial}^{hkl}}{\epsilon_{axial}^{hkl}}. \quad (2.11)$$

The diffraction elastic constants obtained this way are often comparable with the theoretical solutions for the elastic deformation of polycrystals, namely the Reuss, Voigt and Hill's average/Kroner model.

The Reuss model assumes a constant stress in all grains of the material, with the diffraction Young's modulus being determined by (Hutchings et al, 2005b):

$$E_{hkl} = \frac{1}{(S_{11} - 2S_0 A_{hkl})} \quad (2.12)$$

where  $S_0$  is a constant reflecting the inherent anisotropy of the crystal based on the measured single crystal elastic compliances  $S_{11}$ ,  $S_{12}$  and  $S_{44}$  and determined as:

$$S_0 = (S_{11} - S_{12} - S_{44} / 2). \quad (2.13)$$

$A_{hkl}$  is an anisotropy parameter which governs the orientation of the elastic properties of cubic crystals:

$$A_{hkl} = \frac{(h^2 k^2 + k^2 l^2 + l^2 h^2)}{(h^2 + k^2 + l^2)} \quad (2.14)$$

where  $h$ ,  $k$  and  $l$  are the usual Miller index notation.

The Reuss value for the diffraction Poisson's ratio is given by (Hutchings et al, 2005b):

$$\nu_{hkl} = -\frac{(S_{12} + S_0 A_{hkl})}{(S_{11} - 2S_0 A_{hkl})}. \quad (2.15)$$

In the Voigt model a uniform strain condition is assumed to be present in the constituent grains. Thus the diffraction Young's modulus and the diffraction Poisson's ratio is the same for each reflection, given by

$$E_{hkl} = 3K(1 - 2\nu_{hkl}) \quad (2.16)$$

where  $K$  is the bulk modulus, and by

$$\nu_{hkl} = \frac{3K - 2\mu}{2(3K + \mu)} \quad (2.17)$$

where the bulk modulus,  $K$ , and the shear modulus,  $\mu$ , are given by

$$K = \frac{1}{3}(C_{11} + 2C_{12}) \quad (2.18)$$

and

$$\mu = \frac{1}{5}[(C_{11} - C_{12}) + 3C_{44}] \quad (2.19)$$

where  $C_{11}$ ,  $C_{12}$  and  $C_{44}$  are the single crystal elastic constants for the cubic material. The orientation-specific diffraction Young's modulus and Poisson's ratio are equal for the Voigt approach.

In fact the Reuss and Voigt methods detailed above give upper and lower bounds to the calculated elastic constants. A more accurate value is obtained by considering the average values of the two methods. This is known as Neerfeld-Hill average (Noyan and Cohen, 1987). These approaches are valid for untextured polycrystals.

Beyond the elastic limit, lattice strain are generally non-linear. This is due to differences in the inelastic deformation behaviour of the single crystals, which, in the case of plasticity, is referred to as plastic anisotropy. The study of lattice strain response during plastic loading has been quite intensively studied in recent times and has made up the bulk of the work studied using the in-situ method (see for example Allen et al, 1989). The lattice strain response is often interpreted using a micromechanical modelling approach – the elastoplastic self-consistent (EPSC) method (Clausen and Lorentzen, 1998) – and such models can provide insight into the operative deformation mechanisms.

#### *2.4.4 Single peak fitting of diffraction spectra*

In order to measure sample strain, the lattice parameter or position of a Bragg reflection has to be accurately determined. Subsequent shifts must be determined via equations 2.2 or 2.9 depending on the type of experiment with an error of around 100 microstrain ( $1 \times 10^{-4}$ ) allowing stress to be determined with good precision.

Position of reflections is determined by fitting a known function to the measured profile and then allowing the variables in the mathematical function to be minimised in a least-squares refinement carried out through

computer programs such as the RAWPLOT function in GSAS (Larson et al, 2002) or PeakFit by Jandal Software.

Peaks acquired at time of flight sources tend to be asymmetric, even in stress free samples. This is in contrast to those obtained at steady-state reactor source for which the shape of peaks is symmetric and approximately Gaussian in form. Functions suitable for time of flight peaks can be obtained by considering the moderation process.

It is important that the fitting method be the same for all peaks within the spectra if meaningful comparisons are to be made. Therefore the same profile function and background function should be used for each peak within the spectra wherever possible. Generally, the more parameters that are allowed to refine in a fit, the less precise the peak position becomes. In practice only the position, Gaussian width, integrated intensity and background parameters are varied during fitting.

The main peak function used in fitting the diffraction profiles was that of Jorgensen et al, 1978; Von Dreele et al, 1982). With spectrum consisting of time of flight versus intensity, the function is as follows:

$$H(\Delta T) = N \left[ e^u \operatorname{erfc} y + e^v \operatorname{erfc} z \right]. \quad (2.20)$$

Here  $\Delta T$  is the difference in time of flight between the reflection position,  $T_{ph}$ , and the point in the profile function,  $T$ . The term 'erfc' in equation 2.20 is the complementary error function. The terms  $N$ ,  $u$ ,  $v$ ,  $y$  and  $z$  can be explained by consideration of the following derivation contained taken from the GSAS manual (Larson and Von Dreele, 2000).

The profile given in eqn. 2.20 is the results of a convolution of a Gaussian function with two back-to-back exponential functions:

$$H(\Delta T) = \int G(\Delta T - \tau) E(\tau) d\tau, \quad (2.21)$$

with the Gaussian function given by equation 2.22:

$$G(\Delta T - \tau) = \frac{1}{\sqrt{2\pi\sigma^2}} \exp\left[-\frac{(\Delta T - \tau)^2}{2\sigma^2}\right] \quad (2.22)$$

for which  $\sigma^2$  is the Gaussian variance and where, for the exponentials,

$$E(\tau) = 2Ne^{\alpha\tau} \text{ for } \tau < 0 \quad (2.23)$$

and

$$E(\tau) = 2Ne^{-\beta\tau} \text{ for } \tau > 0. \quad (2.24)$$

$\alpha$  and  $\beta$  are the rise and decay coefficients of the exponentials.

The normalisation factor,  $N$ , in equation 2.20 is given by:

$$N = \frac{\alpha\beta}{2(\alpha + \beta)} \quad (2.25)$$

and the variables  $u$ ,  $v$ ,  $y$  and  $z$  are defined as:



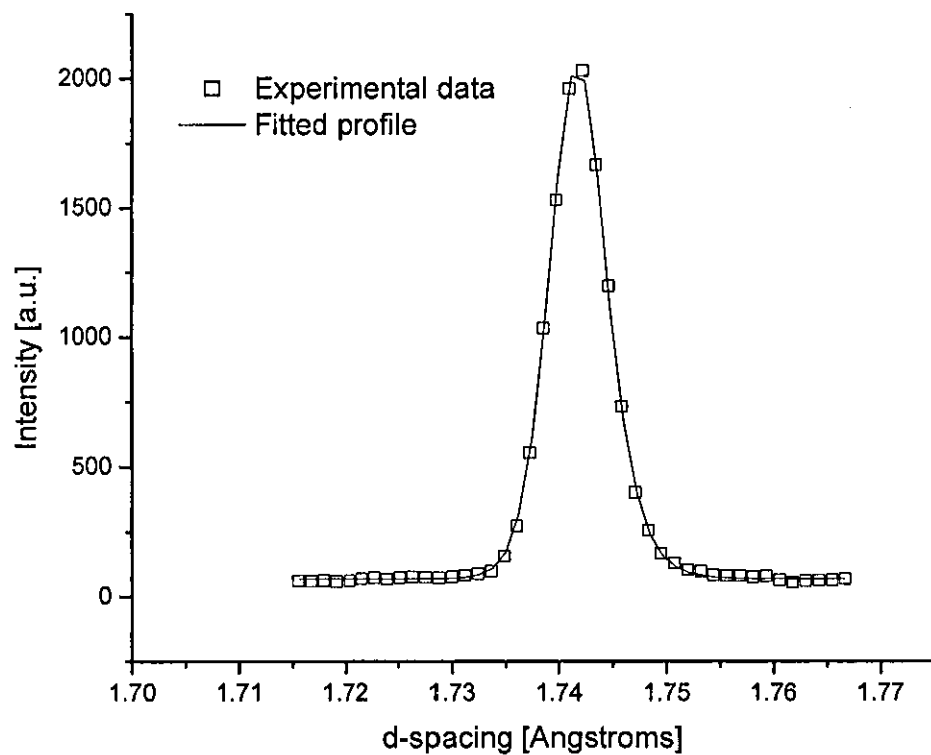


**Figure 2.4:** Example of the fit obtained by the convolution function of Jorgensen and Von Dreele to a peak obtained at a spallation neutron source (function details in main text).

$$u = \frac{\alpha}{2} (\alpha \sigma^2 + 2\Delta T) \quad (2.26)$$

$$v = \frac{\beta}{2} (\beta \sigma^2 - 2\Delta T) \quad (2.27)$$

$$y = \frac{\alpha \sigma^2 + \Delta T}{\sqrt{2\sigma^2}} \quad (2.28)$$

and

$$z = \frac{\beta \sigma^2 - \Delta T}{\sqrt{2\sigma^2}}. \quad (2.29)$$

In practice the function is used in a slightly different form with an integrated intensity term replacing the normalisation term.

Thus the function has 5 variables: the integrated intensity (i.e. area of peak), peak position, Gaussian width and exponential rise and decay coefficients. The function has been used with the PeakFit software by Jandel combined with a background fitting function in all of the single peaks fits contained within this thesis. An example of a fit to a peak obtained on the ENGIN-X instrument is shown in Figure 2.4.

## 2.5 References

Allen, A. J., Andreani, C., Hutchings, M. T., and Windsor, C. G., *NDT International*, 15, (1981), 249-254.

Allen, A. J., Bourke, M. A. M., David, W. I. F., Dawes, S., Hutchings, M. T., Krawitz, A. D., and Windsor, C. G., *Proceedings of the 2<sup>nd</sup> International Conference on Residual Stresses*, London, (1989), 78-83.

Blakemore, J. S., *Solid State Physics* (2<sup>nd</sup> edition), Cambridge University Press, (1985), 25-73.

Carlile, C. J., The Production of Neutrons, in A. J. Dianoux and G. Lander (Eds.), *Neutron Data Booklet*, Institute Laue-Langevin, (2002), 3.1.

Clausen, B. and Lorentzen, T., *Acta Materialia*, 46, (1998), 3087-3098.

Clegg, W., *Crystal Structure Determination*, Oxford University Press, (1998), 1-26.

Dann, J. A., Daymond, M. R., James, J. A. J., Santistiban, J. R., and Edwards, L., *Proceedings of the International Colloquium on Advanced Neutron Sources XVI*, G. Mank and H. Conrad (Eds.), Forschungszentrum Julich GMBH, (2003), 231-238.

Hutchings, M. T., Withers, P. J., Holden, T. M., and Lorentzen, T., Diffraction Techniques and Instrument Design, in *Introduction to the Characterization of Residual Stress by Neutron Diffraction*, Taylor and Francis, (2005a), 65-148.

Hutchings, M. T., Withers, P. J., Holden, T. M., and Lorentzen, T., Interpretation and Analysis of Lattice Strain Data, in *Introduction to the Characterization of Residual Stress by Neutron Diffraction*, Taylor and Francis, (2005b), 203-262.

Johnson, M. W., Edwards, L., and Withers, P. J., *PhysicaB*, 234, (1997), 1141-1143.

Johnson, M. W. and Daymond, M. R., *Journal of Applied Crystallography*, 35, (2002), 49-57.

Jorgensen, J. D., Johnson, D. H., Mueller, M. H., Worlton, J. G., and Von Dreele, R. B., *Proceedings of the Conference on Diffraction Profile Analysis*, Cracow, Poland, (1978), 20-22.

Krawitz, A. D., Brune, J. E., and Schmank, M. J., in E. Kula and V. Weiss (Eds.), *Proceedings of the 28<sup>th</sup> Army Materials Research Conference*, (1981), 139-155.

Krawitz, A. D., *Introduction to Diffraction in Materials Science and Engineering*, John Wiley and Sons, Inc., (2001), 105-118.

Larson, A. C., Von Dreele, R. B. Von Dreele, *General Structure Analysis System (GSAS)*, Los Alamos National Laboratory Report LAUR 86-748 (2002).

Mura, T., *Micromechanics of Defects in Solids* (2<sup>nd</sup> edition), Martinus Nijhoff Publishers, (1987).

Noyan, I. C., and Cohen, J. B., *Residual Stress: Measurement and Interpretation*, Springer-Verlag, (1987), 72.

Owen, R. A., Preston, R. V., Withers, P. J., Shercliff, H. R., and Webster, P. J., *Materials Science and Engineering A*, 346, (2003), 159-167.

Pintschovius, L., Jung, V., Macherauch, E., Schafer, R., and Vohringer, in E. Kula and V. Weiss (Eds.), *Proceedings of the 28<sup>th</sup> Army Materials Research Conference*, (1981), 467-482.

Preuss, M., Pang, J. W. L., Withers, P. J., and Baxter, G. J., *Metallurgical and Materials Transactions A*, 33, (2002), 3227-3234.

Prime, M. B., Hughes, D. J., and Webster, P. J., *Proceedings of the SEM Annual Conference on Experimental and Analytical Methods*, Oregon, USA, (2001), 608-611.

Rauch, H., and Waschowski, W., Neutron Scattering Lengths, in A. J. Dianoux and G. Lander (Eds.), *Neutron Data Booklet*, Institute Laue-Langevin, (2002), 1.1.

Swallowe, G. M., Osborn, J. C., Lukas, P., and Vrana, M., *Proceedings of the 4<sup>th</sup> European Conference on Residual Stress*, Cluny, France, (1996), 61-67.

Von Dreele, R. B., Jorgensen, J. D., and Windsor, C. G., *Journal of Applied Crystallography*, 15, (1982), 581-589.

Wang, D. Q., Harris, I. B., Withers, P. J., and Edwards, L., *Proceedings of the 4<sup>th</sup> European Conference on Residual Stress*, (1996), 69-78.

Webster, G. A., (Ed.), *Polycrystalline Materials – Determination of Residual Stresses by Neutron Diffraction*, ISO/TTA3 Technology Trends Assessment, Geneva, (2001).

Wilson, C. C., *Neutron News*, 6, (1995), 27-34.

Wilson, C. C., Time of Flight Neutron Diffraction, in A. J. Dianoux and G. Lander (Eds.), *Neutron Data Booklet*, Institute Laue-Langevin, (2002), 2.3.

Withers, P. J., Johnson, M. W., and Wright, J. S., *Physica B*, 292, (2000), 273-285.

## **Chapter 3:**

# **Stress-induced martensitic transformation in NiTi studied using in-situ neutron diffraction**

### **3.1 Introduction**

#### *3.1.1 Literature review*

The first recorded investigation of the stress-induced transformation in NiTi using neutron diffraction was made by Bourke et al using the Neutron Powder Diffractometer at the Manuel Lujan, Jr. Neutron Scattering Center, New Mexico, USA in 1996 (Bourke et al, 1996). The experimental setup used was almost identical to that of the ENGIN-X instrument described in a previous chapter, i.e. detectors at  $\pm 90$  degrees to the incident beam, with the loading rig at a 45 degree angle to the incident beam. They studied the compressive response of an untextured superelastic NiTi rod formed by hot-isostatic pressing, which was fully austenitic at room temperature. They found that by loading to approximately  $-2.9\%$  strain around 90 % of the austenite transformed into martensite. They noted that the austenite  $(100)_A$  grains transformed before the  $(111)_A$  grains (i.e. lattice plane normals for these grain orientations aligned with the axis of the sample) – this clearly indicated the strong dependency of the transformation on crystal orientation. Strong texture of the induced martensite phase was observed with the martensite  $(010)_M$  peak being absent in the spectra collected in the axial detector and the  $(100)_M$  reflection unseen in the radial spectra.

Companion papers were then published which provided further experimental results from a NiTi sample and NiTi-TiC composite (Vaidyanathan et al, 1999a). The techniques used in the analysis were also published (Vaidyanathan et al, 1999b). They used both single-peak fitting and Rietveld methods to investigate the phase fraction, internal strain and texture evolution during transformation. A bulk value for the phase fractions was obtained using the Rietveld method. Texture was found to be best modelled using the spherical-harmonics approach, and gave a linear relationship between martensite volume fraction and the macroscopic strain generated during deformation. The lattice parameters obtained from the refinements allowed the bulk strain in the austenite phase to be determined during deformation. They noted a small transfer of load from the austenite phase to the increasing martensite phase at higher applied stresses. A hysteretic bulk lattice strain response was noted. They also note the preferential transformation of the  $(100)_A$  austenite grains during transformation giving rise to an evolving texture as the compression continues. They also calculated the lattice strain responses of austenite grain families and noted that while these were linear at low applied stresses, they showed deviations from this behaviour at higher stress. This was ascribed to strain redistribution as the martensitic phase grows within grains.

These papers illustrated the applicability of the technique to the study of stress induced martensitic transformations (SIMT) in NiTi and polycrystalline shape memory alloys in general. They were rapidly followed by a number of papers concerning the study of SIMT in a Cu-Al-Zn-Mn polycrystal by Sittner and co-workers (Sittner et al, 2001; Sittner et al, 2002a). They adopted a combined experimental and modelling approach to try to understand the mechanics of the load partition behaviour during stress-induced transformation. A specially developed model which used the



single crystal properties of NiTi was developed which allowed a direct comparison between the observable quantities in a diffraction experiment, i.e. lattice strains and martensite volume fractions, with model calculations (Sittner and Novak, 2000). This approach was very successful in explaining the observed mechanical behaviour and correcting some of the misinterpretations in the literature. One example is that of the ‘hardening’ behaviour often seen during transformation – it is more correctly ascribed to the effects of the load partitioning during deformation than the conventional hardening behaviour seen in plastically deforming metals. See appendix for further model details.

Although experimental details have been published elsewhere regarding the study of stress-induced transformations in NiTi using in-situ neutron diffraction the work presented here differs fundamentally due to the fact that the previous highly-referenced work of Vaidyanathan et al was conducted using an untextured sample created by the hot isostatic pressing of elemental powders. This is very much a different processing route to that adopted by commercial manufacturers which involves cold-drawing or extrusion of the ingot formed by arc-melting.

The only other previous studies of NiTi using in-situ neutron diffraction are those conducted by Sittner and co-workers, which have been reported at a number of recent conferences, and have mainly utilised a reactor source and position sensitive detector (PSD) focussing on a small d-spacing around the 1.7 Angstroms. Here the in-situ neutron diffraction technique has been applied to several commercially obtained rods processed via similar routes, resulting in a well-defined  $\langle 111 \rangle$  fibre texture in the rods. It is well-known that the rods have almost identical texture to the commercially available wires and therefore the results and conclusions for the rods are valid also for wire specimens.

This chapter also provides a full list of *hkl*-specific and bulk diffraction elastic constants and diffraction Poisson's ratio for the main austenite reflections for commercially obtained rods, which are unavailable anywhere in the literature. The values are compared with theoretical predictions for NiTi using the Hill and Kneerfeld average of the solutions for elastic constants using the average values of the Reuss (constant stress) and Voigt (constant strain) solutions for a polycrystalline aggregate deforming elastically. These can be calculated using the published elastic constants for austenitic NiTi available in the literature:  $C_{11} = 162.5$  GPa,  $C_{12} = 126$  GPa and  $C_{44} = 37$  GPa (Ren et al, 2001).

### **3.2 Experimental details and material**

The experiment described here was carried out on the ENGIN-X instrument at ISIS. A detailed description of the instrument has been given in Chapter 2, so only a brief summary is provided here. The stress rig was inclined at a 45 degree angle to the incident beam with the standard arrangement of two detectors at  $\pm 90$  degrees to the beam. This set-up allowed for strain to be measured both perpendicular and parallel to the applied stress. Stress was applied using the 50 kN capacity loading rig, and macroscopic strain was measured using a clip-on extensometer. The test was conducted in compression and stopped at various points along the stress-strain curve – the length of time ranging from 15 to 30 minutes – to allow for diffraction data to be collected.

The material was Ni-Ti rod obtained from Memory Metalle, Germany, with a nominal composition of Ni-49.8Ti (at.%) (manufacturer's notation: NiTi-

M). A sample of length = 27 mm and diameter = 10 mm was machined from the as-received material (formed by extrusion) and then subjected to a heat treatment of 600 °C for 1 hour followed by immediate quenching into room-temperature water. The transformation temperatures of the material were subsequently measured using differential scanning calorimetry (DSC). The transformation temperatures were found to be as follows:  $M_s = 30$  °C,  $M_f = 6$  °C,  $A_s = 52$  °C,  $A_f = 74$  °C. The DSC thermogram is shown in Figure 3.1.

The test was conducted at 50 °C after the sample had been cooled from 100 °C, to ensure that it was fully austenitic at that temperature. This temperature was maintained through use of an optical furnace attached to the loading rig. Sample temperature was measured using a thermocouple attached to the sample surface. The sample was maintained at 50 °C for several minutes prior to the deformation to ensure that thermal equilibrium had been achieved.

Analysis of the collected spectra was carried out using single peak fits. The RAWPLOT routine in the GSAS Rietveld refinement program (Larson and Von Dreele, 2000) was used to perform these fits. Peak position and intensity were extracted from each fit, allowing lattice strains and phase fractions to be calculated.

### **3.3 Results and Discussion**

#### *3.3.1 Macroscopic response*

The macroscopic stress-strain curve for the deformation is shown in Figure 3.2. The solid squares marked on the curve indicate the points at which

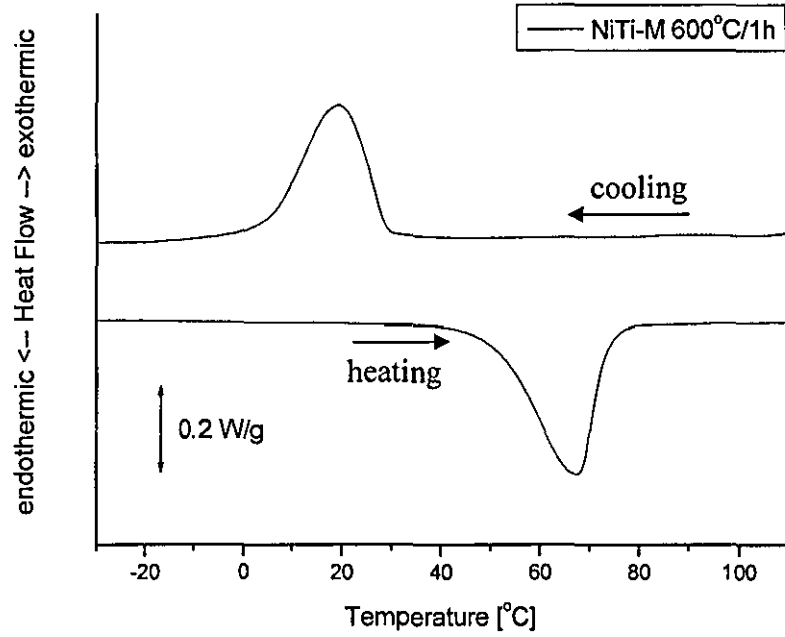


**Figure 3.1:** DSC thermogram of NiTi sample subjected to heat treatment of 600 °C for 1 hour followed by immediate quenching into water at room temperature.

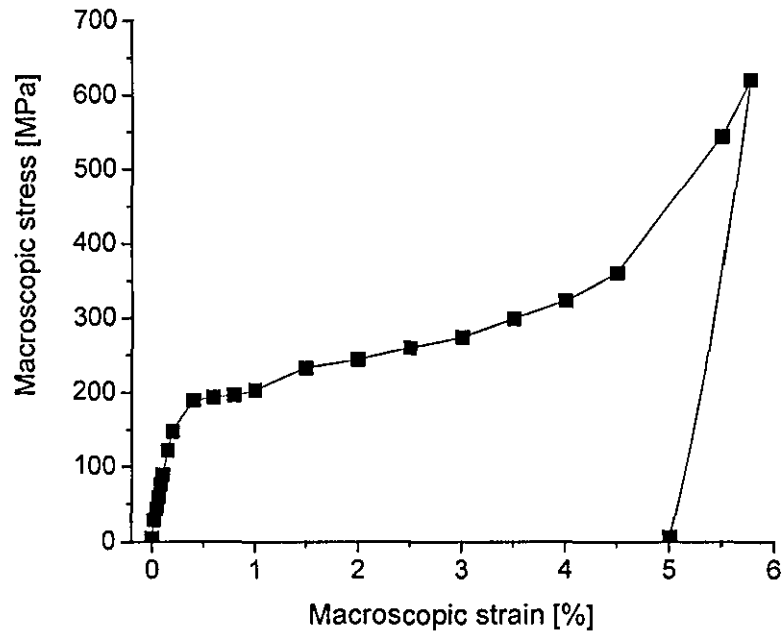


**Figure 3.2:** Macroscopic stress-strain curve for NiTi sample deformed at 50 °C. The test was conducted in compression. The compressive stresses and strains generated are represented as positive quantities in the figure.

diffraction spectra were collected. The measured Young's modulus is  $(70.3 \pm 3.3)$  GPa, which is consistent with literature values of 70-98 GPa (Van Humbeeck and Stalmans, 1998). The yield stress was measured to be 191 MPa using the 0.2 % strain offset method.

Since the deformation is taking place at 50 °C, which is below the austenite finish temperature,  $A_f$ , there is insufficient driving force for the spontaneous reverse transformation back to austenite on removal of the applied load. Hence the stress-strain curve can be seen to simply recover by conventional elasticity of the induced martensitic phase on unloading – giving rise to a compressive residual strain of 5.01 %. The material is therefore not superelastic at this temperature, although full recovery of sample shape was observed on heating well above the austenite finish temperature,  $A_f$ . Thus it is clear, even from the macroscopic measurements, that the induced strain has been caused by phase transformation, as opposed to plastic deformation by the movement of dislocations which is non-recoverable on heating.

### *3.3.2 Sample texture*

Figure 3.3 shows both the axial and radial spectra of the sample at the zero strain load of 5 MPa, i.e. in the austenite state. The peaks are indexed for clarity. It should be noted that there is a  $\langle 111 \rangle$  fibre texture present along the bar axis. This has been observed before for other drawn NiTi wires/rods (Yamauchi et al, 1996), although it is in contrast with the texture developed by other BCC metals during drawing/extrusion, which tends to be of the  $\langle 110 \rangle$  type (Krawitz, 2001). It is also different from the type of texture developed during the cold-rolling of NiTi plate. This tends to endow the

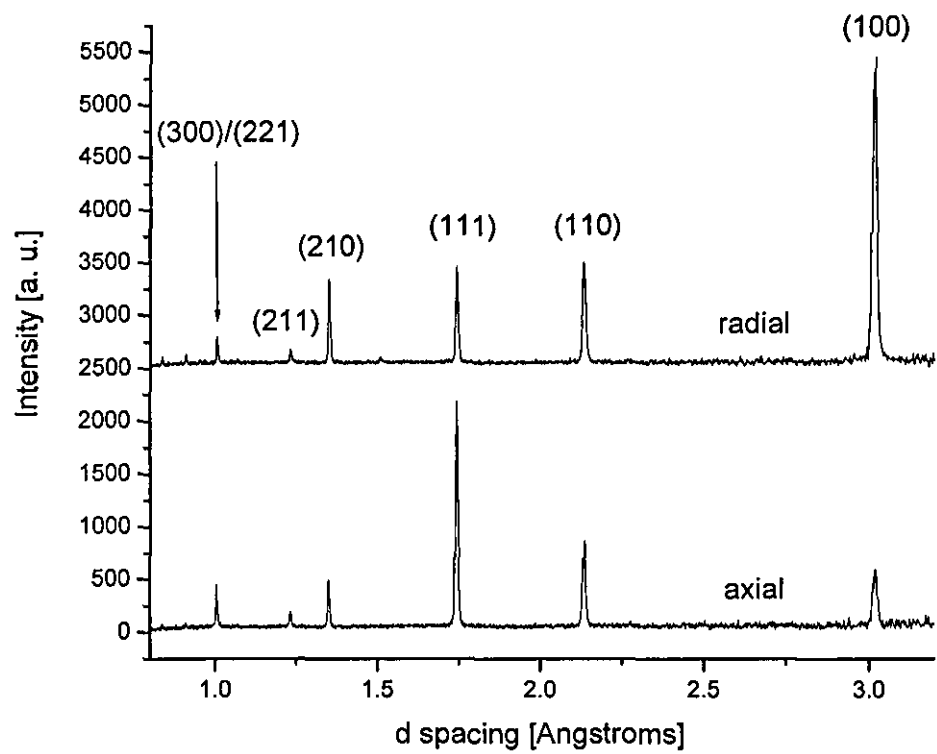


**Figure 3.3:** Zero strain diffraction spectra for NiTi sample used in compression experiments. The material is in the austenitic state.

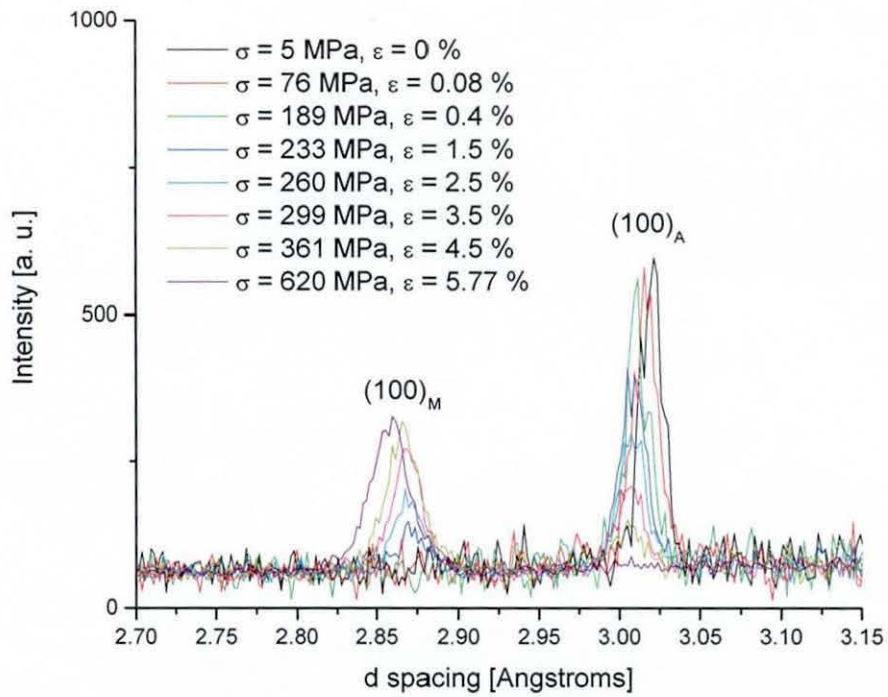


**Figure 3.4:** Axial diffraction spectra focussing on the area around the (100) austenite peak at 3.015 Angstroms. The transfer of intensity is directly to the martensite (100) peak. The (011) martensite peak at 3.07 does not appear.

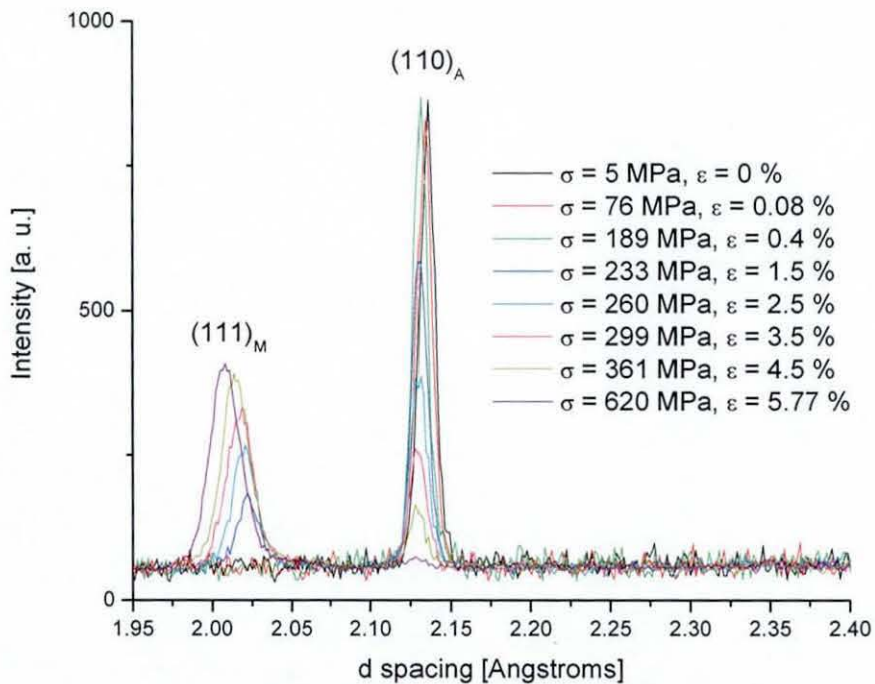


**Figure 3.5:** Axial diffraction spectra focussed on the austenite (110) peak. A direct transfer of intensity to the martensite (111) peak is observed.

plate with a rolling texture of either (110)[1-10] or (111)[1-10] depending on the temperature the rolling was carried out at (Zhao, 1997).

### *3.3.3 Intensity and phase fraction changes on loading*

Single peak fitting of the diffraction peaks allows for much information regarding the microstructure to be extracted. The relative growth, or decrease, in the area of the fitted peaks can be used to make quantitative measurements of the volume fractions of martensite with austenite grains. Qualitatively, the transformation and growth of martensite variants can be seen by examining a small window around the austenite peaks, and since the crystal structures and lattice parameters of the two phases involved in the transformation are well known, it is possible to relate each peak in the spectrum with a particular martensitic variant.

Figure 3.4 shows a small window around the  $(100)_A$  austenite peak, with the diffraction data collected in the axial detector. Due to the crystallography of the transformation and due to the detector geometry, only two martensite peaks – the  $(011)_M$  and  $(100)_M$  – will be seen to appear corresponding to growth of martensite variants within the  $(100)_A$  austenite grains. There are 12 martensitic variants that may form within the austenite grains. The  $(011)_M$  corresponds to those 8 variants (indistinguishable from each other in the diffraction experiment) which provide approximately 5.1 % strain when a fully detwinned martensite structure is formed in this grain under compressive stress (the calculation of strains associated with transformation to particular variants is covered in Chapter 1). The appearance of the  $(100)_M$  peak in the spectrum would indicate that variants providing extension (a tensile strain of approx. 1.7 %) in the direction of the applied compressive



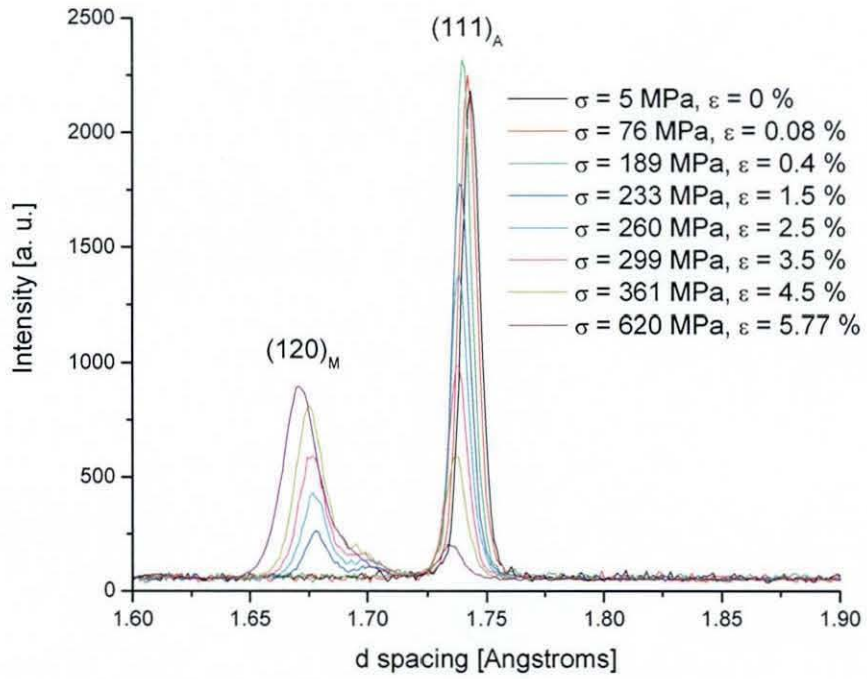
stress had formed. This should not happen under the action of a uniaxial compressive stress and therefore the  $(100)_M$  peak is not observed in the axial spectra after SIMT has occurred.

Similar plots for the intensity changes in the intensities of the austenite  $(110)_A$ ,  $(111)_A$ ,  $(210)_A$  and peaks are shown in Figs. 3.5-3.7.

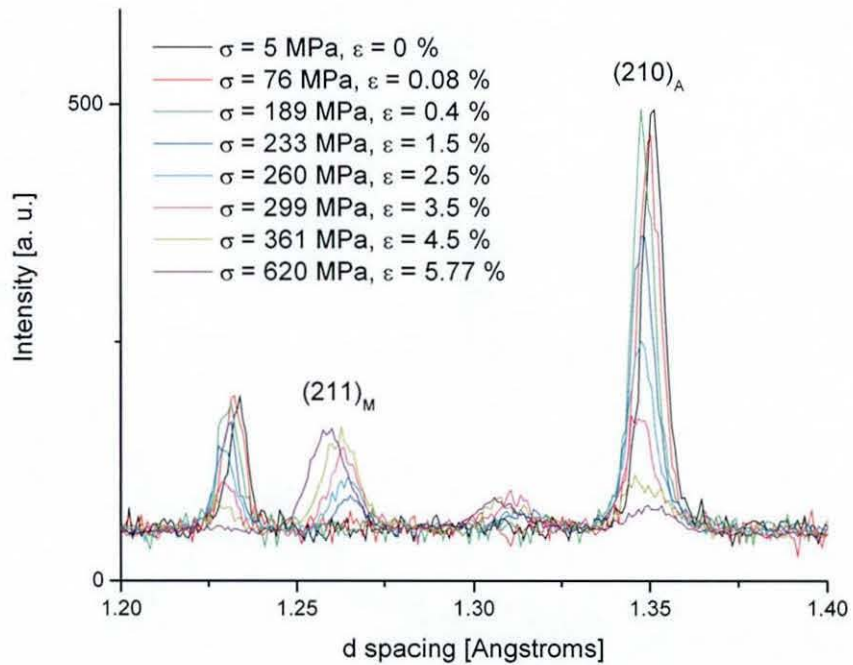
Figure 3.5 shows a small d-spacing window around the window of the  $(110)_A$  austenite peak. In the  $B2 \rightarrow B19'$  martensitic transformation, this peak can transfer intensity to a maximum of 4 peaks within martensitic spectra:  $(002)_M$  at approximately 2.29 Å,  $(-111)_M$  at  $\sim 2.18$  Å,  $(020)_M$  at  $\sim 2.06$  Å and  $(111)_M$  at  $\sim 2.02$  Å. Which each correspond to the formation of variants capable of providing 7.7 %, 2.5 %, -3.3 %, -5.7 % respectively, in the direction of the loading axis. From Fig. 3.5 it is clear that only the  $(111)_M$  peak grows during the transformation.

Figure 3.6 focusses on the d-spacing range around the  $(111)_A$  peak. In this case the peak intensity can be transferred to three peaks only: the  $(-102)_M$  at  $\sim 1.90$  Å, the  $(102)_M$  at  $\sim 1.69$  Å and the  $(120)_M$  at  $\sim 1.67$  Å. The variants corresponding to the growth of these particular peaks offer induced strains of approximately 9.7 %, -2.8 % and -3.9 % respectively. The intensity is transferred almost directly to the  $(120)_M$  peak as can be seen from Fig. 3.6.

Figure 3.7 shows the evolution of the  $(210)_A$  profile and the subsequent martensite variant growth within these grains during transformation. For the  $(210)_A$  peak, intensity can be transferred to 6 peaks: the  $(013)_M$  at  $\sim 1.43$  Å, the  $(-122)_M$  at  $\sim 1.40$  Å, the  $(-211)_M$  at  $\sim 1.34$  Å, the  $(031)_M$  at  $\sim 1.32$  Å, the  $(122)_M$  at  $\sim 1.31$  Å, and the  $(211)_M$  at  $\sim 1.26$  Å. The growth of these peaks offers respective strains of circa 6.4 %, 3.9 %, -0.6 %, -2.37 %, -3.0 % and –



**Figure 3.6:** Axial diffraction spectra focussed on the austenite (111) peak.



**Figure 3.7:** Axial diffraction spectra focussed on the (210) austenite peak. The growth of the (211)<sub>M</sub> peak corresponds to the growth of the most favourable variant in this grain family. The peak at ~ 1.23 Angstroms is the austenite (211).

6.7 %. And it can be observed that the growth of the  $(211)_M$  is concomitant with the decrease in the intensity of the  $(210)_A$  peak.

Figure 3.8 shows a comparison of the full diffraction spectrum obtained for the stress-induced martensite and compares it with the spectrum from martensite formed under stress-free conditions (both for axial geometry). The difference in texture (corresponding to the different variant microstructure) is quite clear.

Similar plots to Figs. 3.4-3.7 can be obtained using the data collected in the radial detector and are shown in Figs. 3.9-3.12.

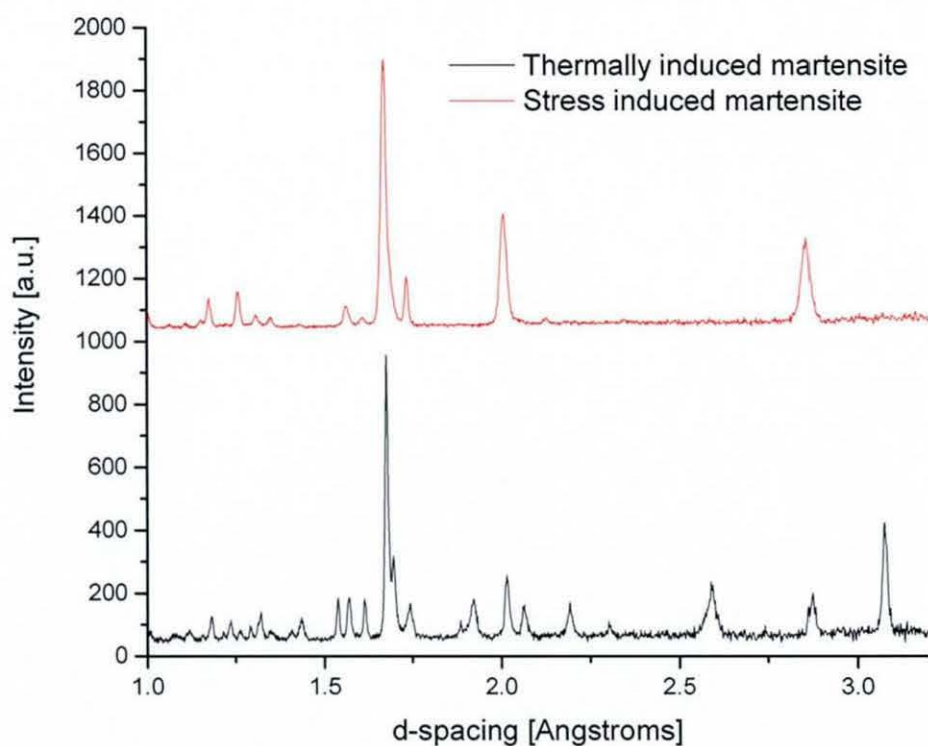
Figure 3.9 shows the d-spacing range around the austenite  $(100)_A$  peak. In contrast to the axial diffraction spectra focussed on this region (shown in Figure 3.4), only the martensite  $(011)_M$  is observed to grow during the transformation.

Figure 3.10 shows the d-spacing region around the  $(110)_A$  peak.

Figure 3.11 focusses on the  $(111)_A$  peak at 1.74 Angstroms.

In Figure 3.12, the d-spacing window containing the  $(210)_A$  peak is focussed on.

As can be seen, for the axial orientation, all the peaks transfer intensity to a single martensite peak. In the radial orientation the peaks with strong intensity observed in the axial detector do not form with any great intensity, or are absent as in the case of the  $(100)$  martensite peak. This behaviour implies that the variants that form within each grain are those which can



**Figure 3.8:** Comparison of thermally-induced martensite collected at room temperature with the stress-induced martensite spectrum. Both spectra were collected in the axial detector.



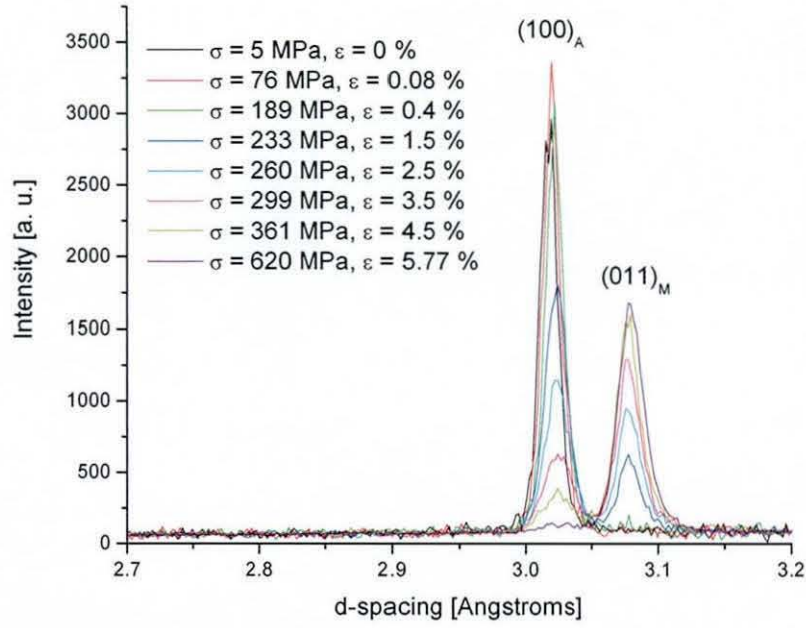


**Figure 3.9:** Radial diffraction spectra from stress-induced martensitic transformation. The d-spacing range focusses on the austenite  $(100)_A$  peak and the subsequent growth of the martensite  $(011)_M$  peak. The martensite  $(100)_M$  is not observed in this detector.

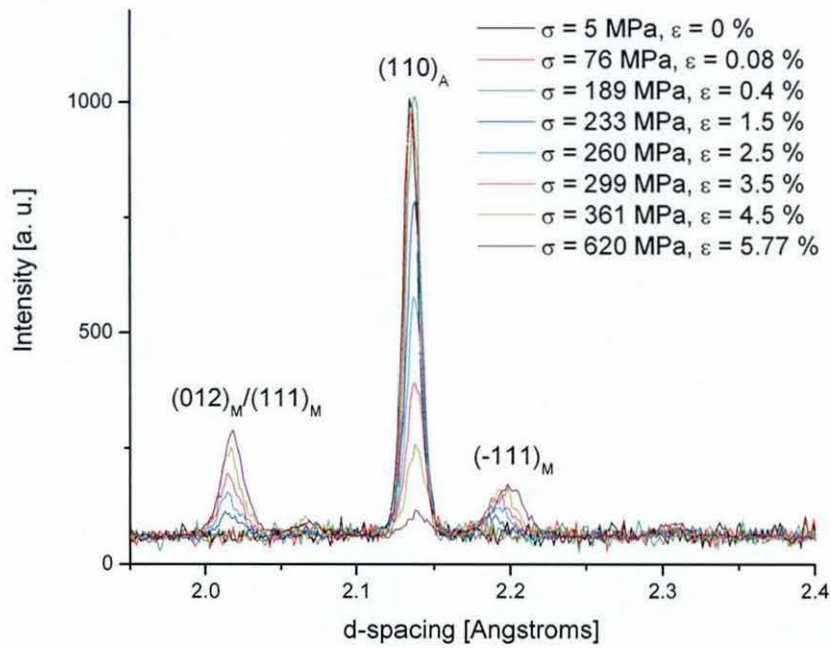


**Figure 3.10:** Diffraction spectra obtained from the radial detector, focussing on the d-spacing window around the austenite  $(110)_A$  peak.

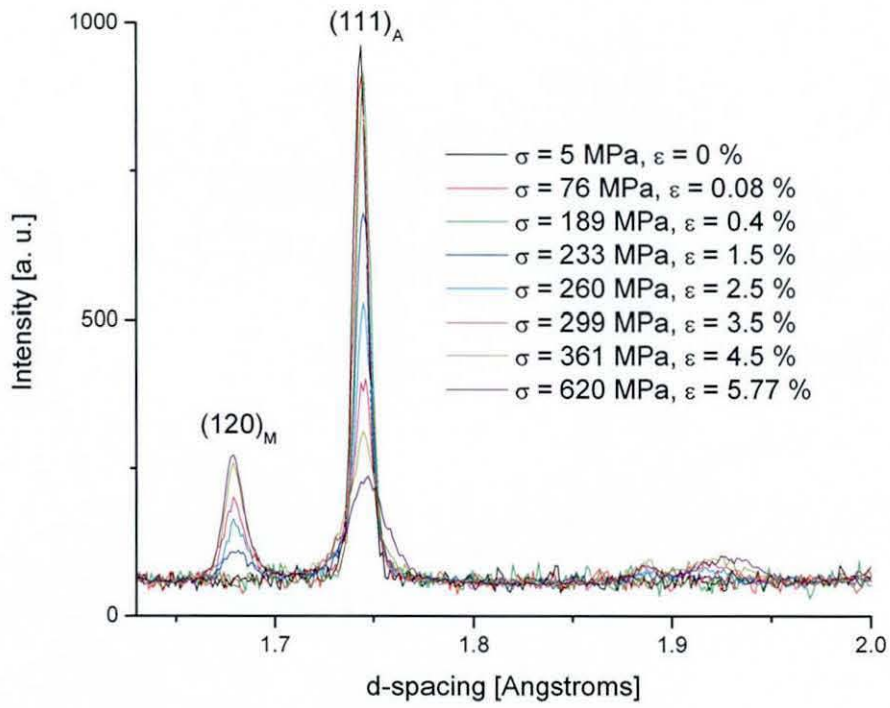


**Figure 3.11:** Radial diffraction spectra focussing on the d-spacing range around the austenite (111)<sub>A</sub> peak.

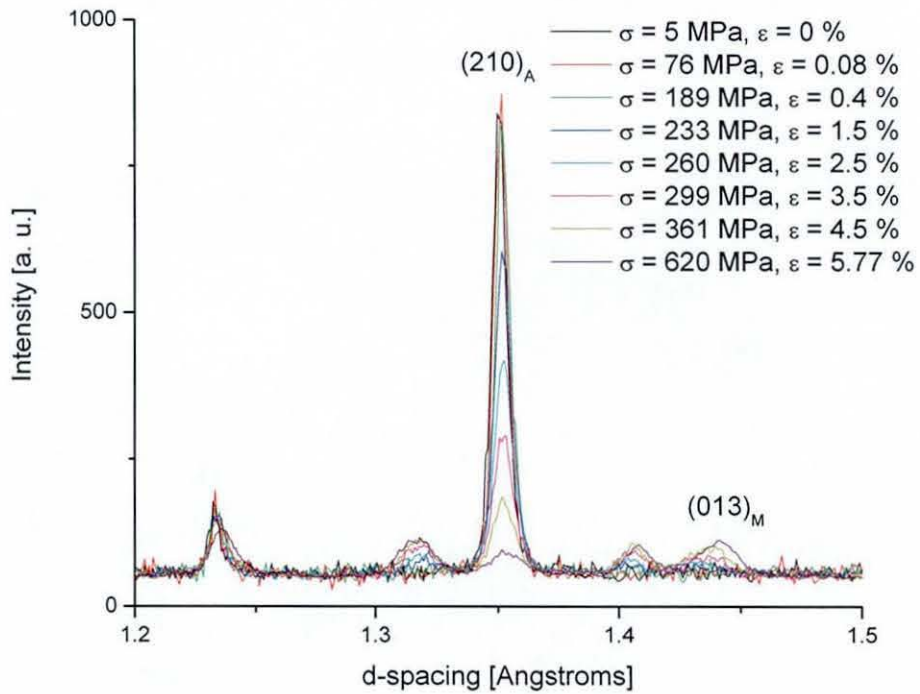


**Figure 3.12:** Radial diffraction spectra focussing on the the d-spacing window around the (210)<sub>A</sub> peak.

provide the maximum strain resolved in the direction of the loading axis. This variant selection rule is the reason for the very strong texture of the martensitic product phase. This strong texture can be very well seen by comparing the thermally-induced martensite spectrum, measured at room temperature, with that formed under stress at 620 MPa and 5.77 % strain, as shown in Figure 3.8. The same variant-selection rule was noted by Oliver et al (Oliver et al, 2003) in their study of stress-induced martensitic transformation in a ferromagnetic shape memory alloy, FePd. This was also observed by Sittner et al in their texture studies on NiTi (Sittner et al, 2004). It is possible to get good information on the transformation and growth of different variants by examining the evolution of diffraction profiles, as discussed above and shown in previous figures. However, the single peak fitting of the observed reflections allows quantitative information on the evolution of volume fractions of variants or phases to be calculated. By comparing the rate of decrease of the austenite reflection intensity, it is possible to see the preferential transformation of different austenite grain orientations. This method also allows the respective phase volume fractions residing within particular grain orientations to be determined.

Figure 3.13 shows the evolution of the fitted peak intensity, collected with the axial detector, as a function of the macroscopic stress. The intensities are normalised with respect to their initial values before loading. Only intensity evolution from the  $(100)_A$ ,  $(110)_A$ , and  $(111)_A$  reflections are reported due to the strong overlap of martensite reflections below around 1.5 Angstroms preventing reliable single-peak fits being made to the data in that region.

It can be seen that the reflection intensity decreases in the following order:  $(110)_A$  first, followed by the  $(100)_A$ , and finally the  $(111)_A$ . Some of the behaviour noted within the textured rod tested here is similar to that

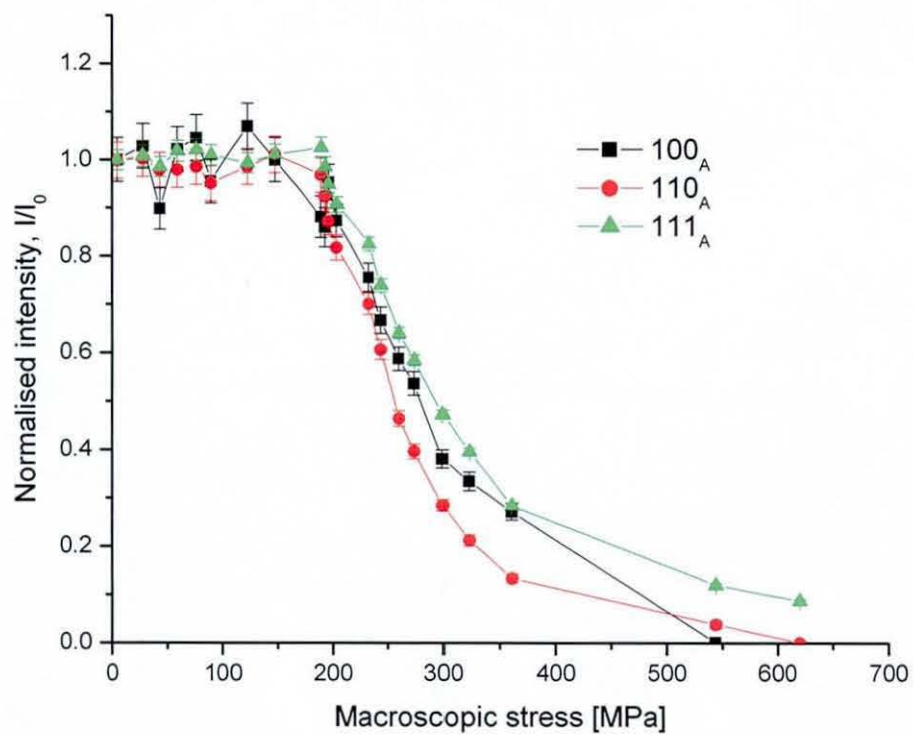


**Figure 3.13:** Evolution of austenite peak intensity with applied stress for the  $(100)_A$ , the  $(110)_A$  and  $(111)_A$  reflections. The intensity of the peaks are normalised with respect to their values in the unloaded state. The data is from the axial bank of detectors.



observed by Vaidyanathan et al, in that they note the lack of full transformation in the  $(111)_A$  grains; they record a retained volume fraction of around 40 % austenite still residing within this grain orientation at the end of the ‘plateau’ region of the stress-strain curve. Similar behaviour is recorded here, in which the  $(111)_A$  oriented grains are seen not to transform fully; at a compressive stress of 620 MPa, there still remains a 10 % volume fraction of austenite within these grains (see Fig. 3.13). Since there is no problem with transforming  $111_A$  oriented NiTi single crystals in compression, this behaviour must be ascribed to the characteristic load transfer behaviour in polycrystalline NiTi transforming under a compressive stress.

Comparison with the available micromechanical model results for the compressive stress-induced transformation in NiTi is interesting. Results from the Sittner-Novak crystallographic SMA model mentioned earlier are available in the literature and can be compared with the results presented here (see appendix for a brief review). Focussing purely on the evolution of intensity, they found that the order of transformation for the compressive SIMT deformation simulation of an untextured NiTi polycrystal was  $(110)_A \rightarrow (100)_A \rightarrow (111)_A$ . Comparison of the model results available in the literature are shown in figure 3.14 as a function of the macroscopic strain. These compare well despite the fact that the material from which these results were obtained is strongly textured and the simulation was run for an alloy which possesses random grain orientations. The differences that can be observed between model and experimental results are most likely due to the difference in texture of the rod used in the experiment and simulation.

#### *3.3.4 Lattice strain response*

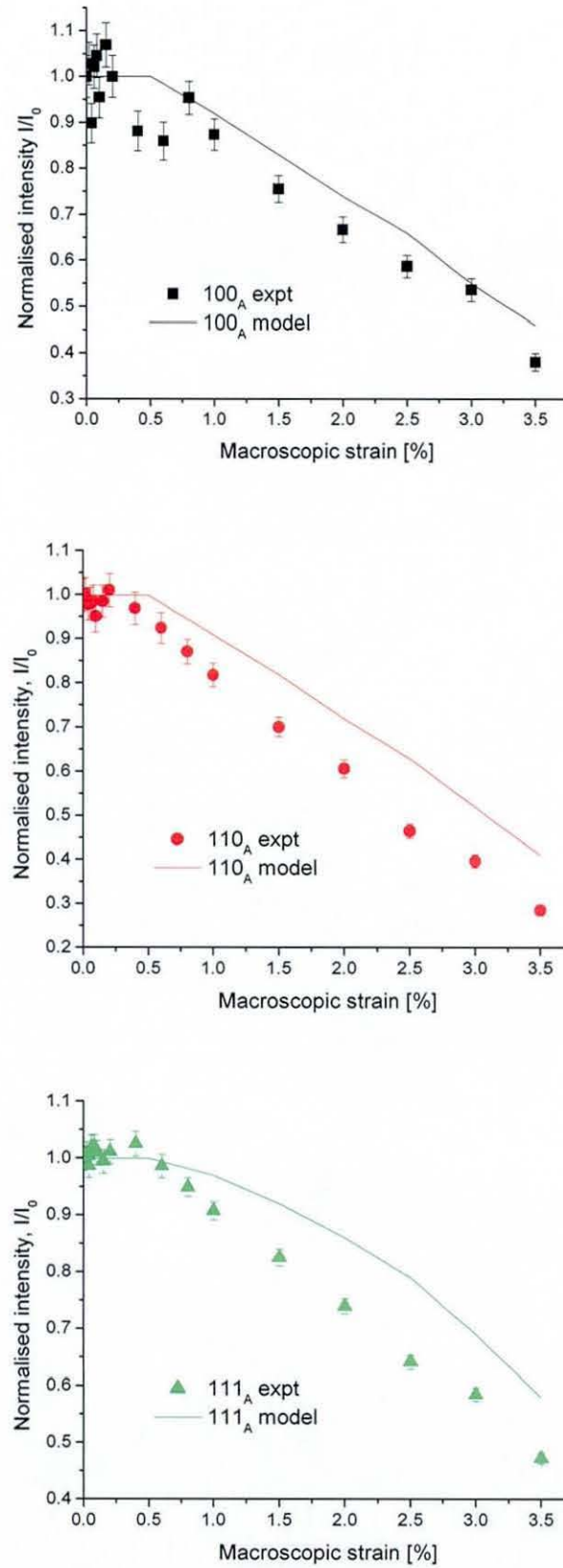


**Figure 3.14:** Comparison of intensity evolution for experimental and Sittner-Novak model simulations for compressive stress-induced martensitic transformation. Simulations results presented in reference (Sittner et al, 2002b).

The lattice strain response for individual grain families was obtained from the shifts in peak position during deformation, relative to their position in the unloaded state. The peaks were fitted using the same single-peak method used for the determination of the integrated intensity. The results of this shift for axial and radial detector banks are shown in Figures 3.15 and 3.16, respectively.

Below around 190 MPa, i.e. below the yield/transformation stress of the material (see the macroscopic stress-strain curve in Fig. 3.2) the response of all peaks is linear with the applied stress. The gradients of these responses do not show much difference due to the fact that the austenite has very low elastic anisotropy, the degree of which is given by the ratio  $2C_{44}/(C_{11}-C_{22})$ , and is equal around 2 for NiTi austenite (Mellor, 1987). These initially linear responses can be fitted with straight lines in order to obtain the diffraction elastic constants of the material. These are generally required in order to convert the measured strain into stress, and can be compared with polycrystal model predications of the elastic responses of grain families. The two quantities obtained from the fits: the diffraction Young's modulus,  $E_{hkl}$ , and the diffraction Poisson's ratio,  $\nu_{hkl}$ , are displayed in Figure 3.17 and Figure 3.18 respectively, where they are compared with theoretical values for the  $hkl$ -specific Young's modulus and Poisson's ratio, calculated using the Hill and Kneerfeld average of the Reuss and Voigt solutions for each peak. Experimentally determined values are marked by solid squares on the figures, with the Hill-Kneerfeld averages marked by a broken line drawn through calculated points.

Examining Figures 3.17 and 3.18 it can be seen that the experimentally determined values are quite close to those determined theoretically, despite the theoretical approach adopted here assuming a random distribution of



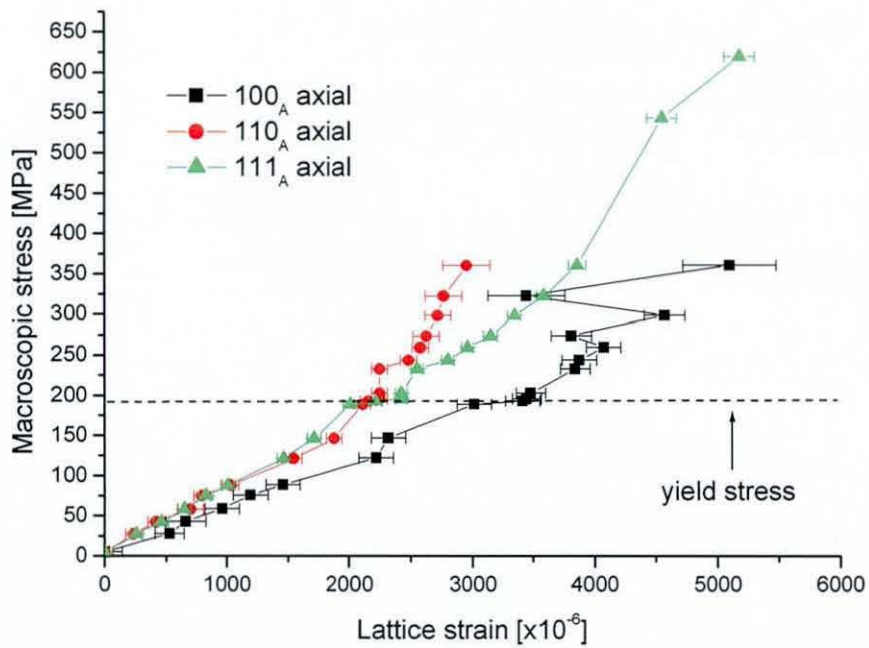


**Figure 3.15:** Axial lattice strains for austenite  $(100)_A$ ,  $(110)_A$  and  $(111)_A$  reflections. The yield stress of the bulk material (obtained by the 0.2 % offset method) is shown by the broken line. Stresses and strains are compressive and reported as positive quantities.

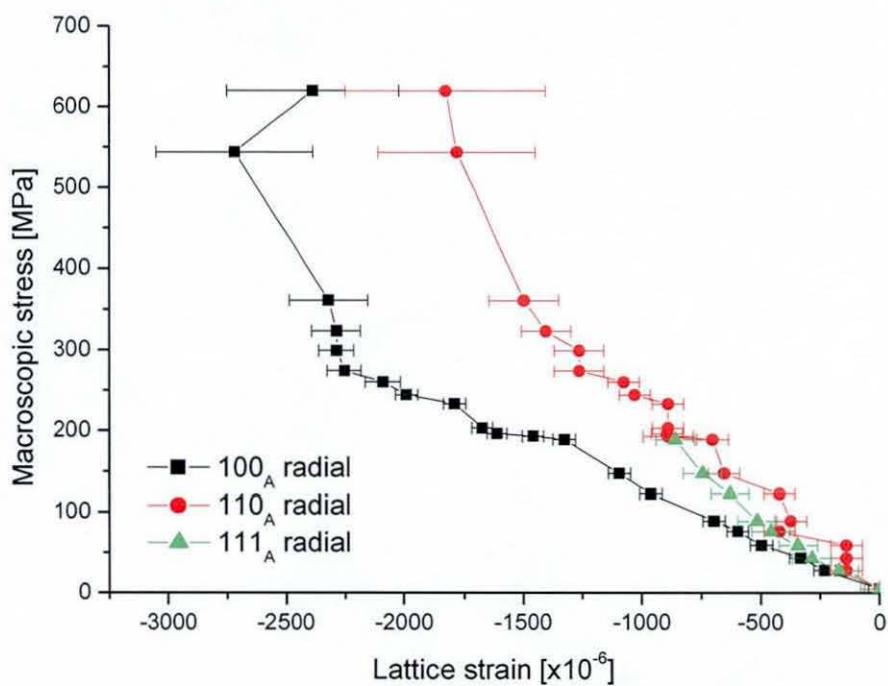


**Figure 3.16:** Radial lattice strains for austenite  $(100)_A$ ,  $(110)_A$  and  $(111)_A$  reflections. The test was conducted in compression with compressive stress being denoted as a positive quantity.

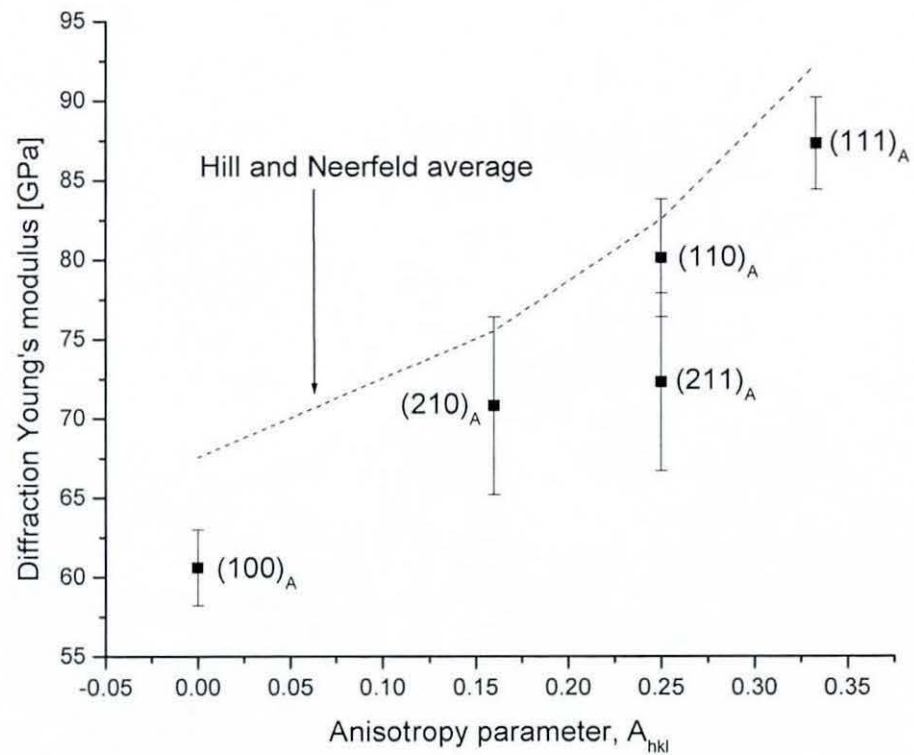


**Figure 3.17:** Diffraction Young's moduli obtained from the gradients of the stress-lattice strain responses of individual reflections in the axial detector. The solid squares correspond to the experimentally determined values while the broken line is fit to values calculated using the Hill-Kneerfeld average model of an elastically deforming polycrystal.

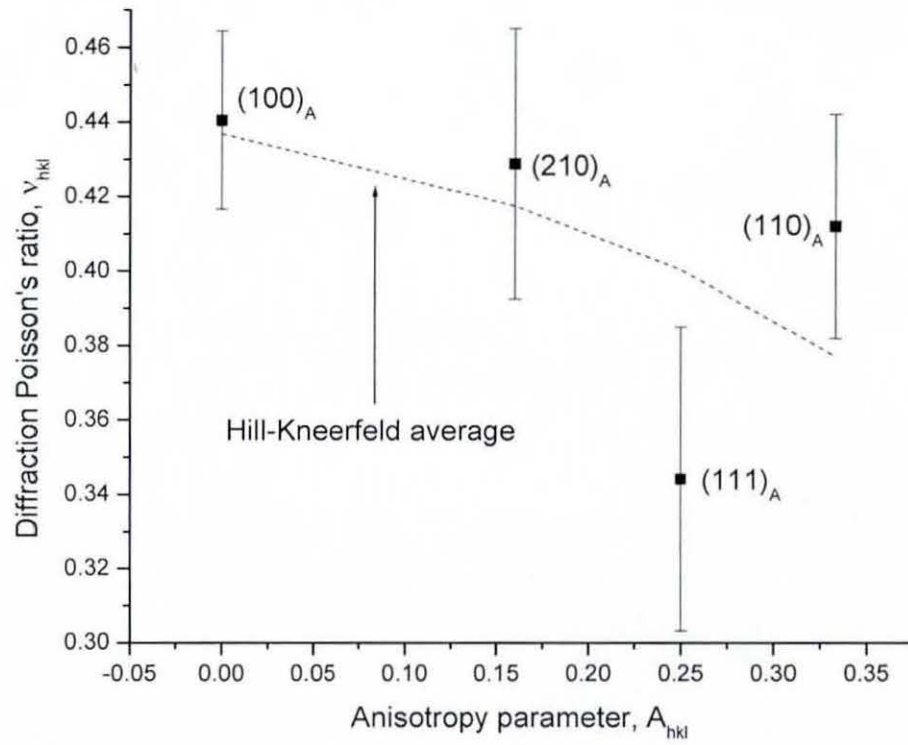


**Figure 3.18:** Diffraction Poisson's ratio obtained from the gradients of the applied stress-lattice strain responses of individual reflections in the radial detector. The solid squares correspond to the experimentally determined values while the broken line is fit to values calculated using the Hill-Kneerfeld average model of an elastically deforming polycrystal.

crystallite orientations and despite the differences that are apparent, the results follow from what would be conventionally expected for an cubic material such as NiTi austenite, with the (111) direction being the stiffest and the (100) being the most compliant. The other directions considered should have values which fall between these two extremes in proportion to the value of the anisotropy factor,  $A_{hkl}$ , for each particular peak. Thus it would be expected that the peaks would have stiffness increasing in the following order:  $(100)_A \rightarrow (210)_A \rightarrow (110)_A$  and  $(211)_A$  (which should be equal)  $\rightarrow (111)_A$ , and this is what is found experimentally.

Beyond the macroscopic yield stress it can be seen that the peaks exhibit marked deviations from linearity (Fig. 3.15). Since we associate the macroscopic yielding with the onset of the stress-induced martensitic transformation in the austenite grains, the differences in lattice strain response observed are due now to the combined effects of the elastic anisotropy and transformation anisotropy (the orientation dependence of the transformation).

For the axial peak strains shown in Figure 3.15 it can be seen that the  $(100)_A$  and  $(110)_A$  reflections exhibit qualitatively similar behaviour, i.e. they both show relaxation of the load they bear as the transformation within these grains continues since the load partitioning behaviour should follow, in an approximate way, the rule of mixtures for composites of the form:  $V_A\sigma_A + (1 - V_A)\sigma_M = \sigma_{\text{appl}}$ , where  $V_A$  is the volume fraction of austenite,  $\sigma_A$  is the stress in the austenite phase,  $\sigma_M$  is the stress in the martensite phase and  $\sigma_G$  is the applied stress. Thus it would be expected that as the martensite phase grows, load is progressively transferred to the martensite and load borne by the austenite grains diminishes.



This behaviour is observed in the case of the  $(100)_A$  and  $(110)_A$  reflections but not for the  $(111)_A$  peak which actually exhibits a deviation towards increasing compressive strain. This is most likely due to a lack of transformability of this grain orientation during the compressive SIMT in polycrystalline NiTi, since single crystals cut in this orientation exhibit full transformation behaviour under compression. The load partitioning behaviour is therefore such that these grains do not fully transform within the 'plateau' region of the stress-strain curve, i.e. up to about 4 % strain, nor are they fully transformed at the fullest extent of the deformation carried out here: there still resides a retained volume fraction of around 10 % within these grains. This lack of transformation of these austenite grains results in their need to bear an increasing amount of load and hence the shift to towards more compressive strain as opposed to the relaxation behaviour of both the  $(100)_A$  and  $(110)_A$  grains.

### **3.4 Conclusions**

The stress-induced martensitic transformation in a commercial NiTi rod during compression has been studied using in-situ neutron diffraction. Single peak fitting analysis was used to determine both the lattice strain response and evolution of martensite/austenite phase volume fractions existing within several grain families during the deformation.

From examination of the growth and decay of peak intensity within the axial and radial detector banks, intensity changes were seen to correspond with the variant selection mechanism seen in shape memory alloys which resulted in the growth of those variants providing maximum strain when resolved along the loading axis. Quantitative measurements were made of



these changes in peak integrated intensity and the results were compared with micromechanical model results for polycrystalline NiTi available within the literature. The measured response was quite close to that observed in the simulations, despite the fact that the simulations took no account of the strong texture present within the rod.

The lattice strain responses were measured using single peak fits to the data collected. The initially linear responses of grain families both parallel and perpendicular to the applied stress were compared with theoretical predictions based on the average responses predicated by the Voigt and Reuss approached to an elastically deforming polycrystal (the Hill-Kneerfeld average). Again, reasonable agreement was achieved despite the fact that the theoretical results are based on a random distribution of grains in the material. The lattice strain response into the transformation regime was seen to deviate from the initial linearity. This was ascribed to the particular load transfer behaviour which resulted from the preferential transformation of particular grain orientations. The  $(111)_A$  was seen to exhibit behaviour opposite to that of the  $(100)_A$  and  $(110)_A$  as a result of the lack of transformability in this particular grain orientation.

### **3.5 References**

Bourke, M. A. M., Vaidyanathan, R., Dunand, D. C., *Applied Physics Letters*, 69(17), (1996), 2477-2479.

Krawitz, A. D., *Introduction to Diffraction in Materials Science and Engineering*, John Wiley & Sons, (2001).

Larson, A. C., and Von Dreele, R. B., *General Structure Analysis System (GSAS)*, Los Alamos National Laboratory Report LAUR 86-748 (2000).

Mellor, B. G., in V. Torra (ed.), *The Science and Technology of Shape Memory Alloys*, Impresrapit, Barcelona, (1987), 334.

Oliver, E. C., Mori, T., Daymond, M. R., and Withers, P. J., *Acta Materialia*, 51, (2003), 6453-6464.

Ren, X., Miura, N., Zhang, J., Otsuka, K., Tanaka, K., Koiwa, M., Suzuki, T., and Chumlyakov, Y. I., *Materials Science and Engineering A*, 312, (2001), 196-206.

Sittner, P., and Novak, V., *International Journal of Plasticity*, 16, (2000), 1243-1268.

Sittner, P., Lukas, P., Daymond, M. R., Novak, V., and Swallowe, G. M., *J. Phys. IV*, 11, (2001), 159-166.

Sittner, P., Lukas, P., Neov, D., Daymond, M. R., Novak, V., and Swallowe, G. M., *Materials Science and Engineering A*, 324, (2002a), 225-234.

Sittner, P., Novak, V., Lukas, P., Lugovyy, D., Neov, D., and Tovar, M., *Materials Science Forum*, 404-407, (2002b), 829-834.

Sittner, P., Neov, D., Lukas, P., and Toeblens, D. M., *Journal of Neutron Research*, 12, (2004), 115-120.

Vaidyanathan, R., Bourke, M. A. M., Dunand, D. C., *Acta Materialia*, 47(12), (1999a), 3353-3366.

Vaidyanathan, R., Bourke, M. A. M., Dunand, D. C., *Journal of Applied Physics*, 86(6), (1999b), 3020-3029.

Van Humbeeck, J., and Stalmans, R., Characteristics of shape memory alloys, in K. Otsuka and C. M. Wayman (eds.), *Shape Memory Materials*, Cambridge University Press, (1998), 149-183.

Yamauchi, K., Nishida, M., Itai, I., Kitamura, K., and Chiba, A., *Mater. Trans. Japan Inst. Metals*, 37, (1996), 210-217.

Zhao, L. C., Texture Development and Anisotropic Behaviour in a Ti-45Ni-5Cu (at.%) Shape Memory Alloy, PhD thesis, University of Twente, (1997).

## **Chapter 4:**

# **Deformation of aged NiTi studied using in-situ neutron diffraction**

### **4.1 Introduction**

#### *4.1.1 General*

Single-crystals of NiTi have low mechanical strength when in solution heat treated form, with the consequence that superelastic studies of material in this state rarely show fully recoverable strains, even above the  $A_f$  temperature. To a certain extent the same is true of NiTi in its polycrystalline form (Saburi et al, 1982). It is very rarely used in practical applications in a solution heat treated state and more often than not requires strengthening before use. Strengthening can be achieved via a number of different routes. The main ones, as for most materials, being cold-working, grain size reduction, the addition of other elements to form an interstitial or substitutional solid-solution (solid solution strengthening) or the introduction of precipitates into material. Essentially, anything that impedes the motion of dislocations improves the strength (Callister, 2003). In the case of NiTi, it has been found that prior cold-working and appropriate annealing (circa 400 °C) is required before fully recoverable strains are observed in experiments (Saburi et al, 1986).

As stated in the paragraph above, the accepted optimum heat treatment temperature is 400 °C. However, the B2 austenite region of the equilibrium phase diagram (circa 800 °C) exists down to room temperature only for a



very narrow composition range of nickel content between 50.0 to 50.5 at. %. Slow cooling to room temperature of nickel compositions any greater or less than this figure results in the formation of precipitates. The phase diagram for Ni-Ti alloys was included in Figure 1.7 in Chapter 1.

#### *4.1.2 Precipitation process in Ni-Ti*

At ageing temperatures of around 400 °C nickel rich (at.% > 50.5) NiTi decomposes into metastable Ni<sub>4</sub>Ti<sub>3</sub> precipitates. Heat-treatment is often used to promote this precipitation as the strengthening effect, particularly when combined with prior cold working, optimizes the superelastic properties.

At temperatures below around 700 °C NiTi begins to decompose to its equilibrium phases while proceeding through a number of metastable phases. The reaction processes at different temperatures are as follows (Saburi, 1998):

- At temperatures less than 680 °C:  
$$\text{NiTi} \rightarrow \text{NiTi} + \text{Ni}_4\text{Ti}_3 \rightarrow \text{NiTi} + \text{Ni}_3\text{Ti}_2 \rightarrow \text{NiTi} + \text{Ni}_3\text{Ti}.$$
- At temperatures between 680 °C and 750 °C:  
$$\text{NiTi} \rightarrow \text{NiTi} + \text{Ni}_3\text{Ti}_2 \rightarrow \text{NiTi} + \text{Ni}_3\text{Ti}.$$
- At temperatures between 750 °C and 800 °C:  
$$\text{NiTi} \rightarrow \text{NiTi} + \text{Ni}_3\text{Ti}.$$

In all cases therefore, the final products are  $\text{Ni}_3\text{Ti}$  precipitates embedded with a matrix of NiTi. However, in the intermediate stage of ageing some useful properties results from the appearance of the  $\text{Ni}_4\text{Ti}_3$  precipitates.

The  $\text{Ni}_4\text{Ti}_3$  precipitates, which are lenticular in shape, grow on the  $\{111\}_A$  planes of the austenite phase and due to their coherency with the matrix, give rise to a localized distortion of the surrounding material. This has some interesting effects on the transformation behavior of NiTi alloys. The stresses strongly influence shape memory properties and offer an improvement on the amount of recoverable strain seen in both superelastic deformation and the shape memory effect. As such, heat treatments of around 400 °C are most commonly used since both precipitation of the  $\text{Ni}_4\text{Ti}_3$  occurs and the temperature is low enough that recrystallisation, and hence loss of dislocation strengthening, do not occur.

Since the precipitates are nickel-rich, their formation results in a lowering of the matrix, i.e. the austenite phase, composition. This has a strong effect on the transformation behaviour since a 0.1% change in composition results in a change in transformation temperature by approximately 10 °C (Melton, 1990).

#### *4.1.3 R-phase martensitic transformation*

The precipitates also strongly affect the crystalline phases appearing via the martensitic transformation occurring under temperature and/or stress. Solution heat treated NiTi displays only a two step reversible transformation from the cubic B2 phase to the monoclinic form of martensite designated B19' and vice versa.

However, it is possible for a second martensitic phase to be introduced into the transformation cycle. This phase is known as the R-phase and has a trigonal structure.

The R-phase was first observed in diffraction experiments by Dautovich and Purdy, 1965 and Wang et al, 1965 (Otsuka, 1990). However, it was not known at this time as a martensitic phase and its appearance was thought to be a precursor effect to the B19' martensite formation.

Cold-work, ternary alloying (with Fe, Al, Cu, Co or Cr for example) or, as in this case, ageing of nickel rich alloys is required for the R-phase transformation to be observed (Miyazaki et al, 1986).

Both the shape memory effect (SME) and superelasticity (SE) are associated with the formation of the R-phase in mechanical tests. Although it results in lower recoverable strains (of the order of 1 %), this is offset by the excellent fatigue properties, e.g. the 500,000<sup>th</sup> cycle of thermomechanical deformation experiment reports a curve unchanged from that on the first cycle (Otsuka, 1990).

This very small hysteresis is also observed in calorimetry experiments, where the observed hysteresis is of the order of 1-2 degrees. These properties make the R-phase interesting for applications such as thermal actuators and proportional control devices, which both require the small transformation hysteresis characteristic of the R-phase (Otsuka, 1990).

The lattice deformation associated with the B2  $\rightarrow$  R-phase is shown in Figure 4.1. The R-phase is thus formed by an elongation along one the four equivalent  $\{111\}$  body diagonals of the austenite phase. There are therefore

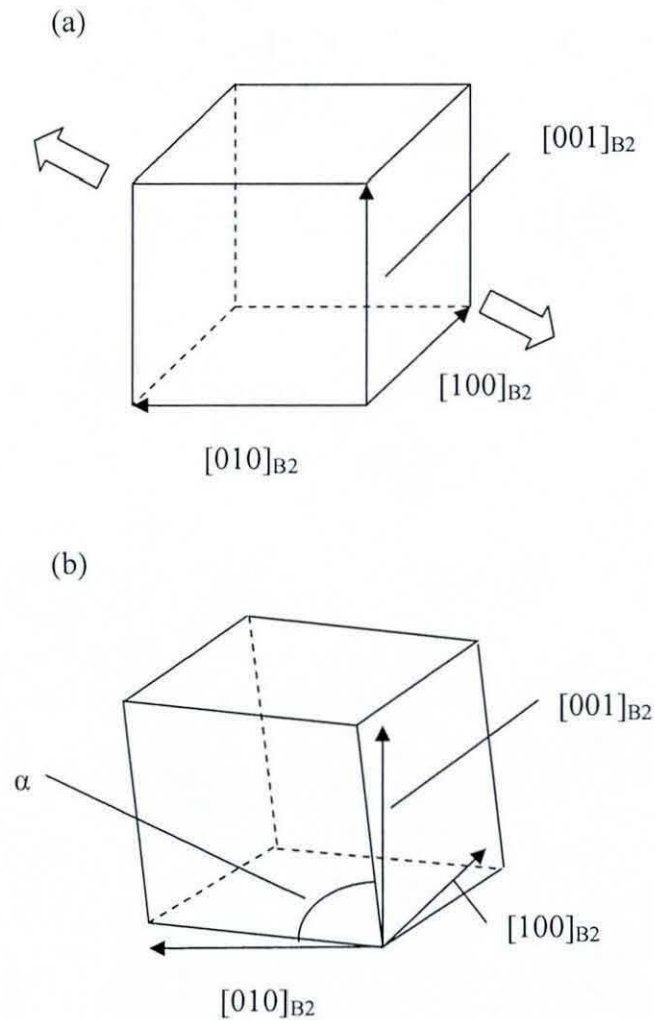


**Figure 4.1:** Schematic diagram of the lattice deformation required for the B2 to R-phase transformation. The two large arrows in Fig. 4.1a illustrate the formation of a particular variant by elongation along the  $\langle 111 \rangle$  body diagonal of the cubic unit cell. Figure 4.1b shows the R-phase unit cell, along with the original B2 lattice parameters. The rhombohedral nature of the new unit cell is characterised by the angle,  $\alpha$ , marked on the diagram. Diagram after Miyazaki et al, 1988.



4 lattice correspondence variants of the R-phase. The lattice correspondence for these four variants is shown in Table 4.1.

The crystal structure is trigonal and is therefore often described within the literature using hexagonal axes. Using this convention, the  $c$ -axis of the R-phase corresponds to the  $\langle 111 \rangle$  direction of the austenite phase.

Thus the lower symmetry phase is trigonal with an associated rhombohedral distortion,  $\alpha$ , and lattice parameter  $a$  ( $a=b=c$  for a rhombohedral unit cell). The transformation is first order in the same way as the B2-B19' transformation, and is therefore associated with an evolution of heat on cooling (and therefore an absorption of heat on heating). Although the latent heat is much smaller than that of the B2-B19' transformation.

The crystal structure data used in this study is that of Goryczka and Morawiec (Goryczka and Morawiec, 2004) with lattice parameters taken as  $a = 0.73541$  nm and  $c = 0.52834$  nm. The full structural data used for determining indices of fitted peaks, taken from this paper, are shown in Table 4.2. The data was used to obtain the expected peak position and intensities of the R-phase, and thus index the R-phase peaks.

Table 4.3 shows the expected peak positions and intensities expected, calculated using the structural data in Table 4.2. The expected diffraction pattern was calculated using the computer program *Powdercell for Windows* (version 2.4), written by Kraus and Nolze, 2000, available on the internet.

The B2-R-phase transition does, however, have a partially second order nature. Transformations of this type are associated with gradual changes in crystal structure as opposed to the large 'jumps' which occur in first order

Variant	$[100]_R$	$[010]_R$	$[001]_R$	$(0001)_R$
1	$[1-21]_A$	$[11-2]_A$	$[111]_A$	$(111)_A$
2	$[211]_A$	$[-11-2]_A$	$[-111]_A$	$(-111)_A$
3	$[121]_A$	$[112]_A$	$[-1-11]_A$	$(-1-11)_A$
4	$[211]_A$	$[11-2]_A$	$[1-11]_A$	$(1-11)_A$

**Table 4.1:** Lattice correspondence for the R-phase and the B2 parent phase. The R-phase indices are for a hexagonal basis using Miller indices notation. The lattice plane correspondence in the fifth column is given in Miller-Bravais notation (Fukada et al, 1992; Otsuka and Ren, 2005).

Alloy (at.%)	Lattice constants [nm]				
	<i>a</i>	<i>c</i>			
Ni-48.8Ti	0.73541	0.52834			
Atom	Wyckoff notation	Atomic coordinates			
		<i>x</i>	<i>y</i>	<i>z</i>	
Ti 1	1 <i>a</i>	0	0	0	
Ti 2	2 <i>d</i>	1/3	2/3	0.045	
Ti 3	6 <i>g</i>	0.663	0.658	0.651	
Ni 1	1 <i>b</i>	0	0	½	
Ni 2	2 <i>d</i>	1/3	2/3	0.544	
Ni 3	6 <i>g</i>	0.684	0.670	0.152	

**Table 4.2:** Structural data from the X-ray diffraction experiments of Goryczka and Morawiec, 2004, for the R-phase present in NiTi with a space group of *P*-3.

<i>h</i>	<i>k</i>	<i>l</i>	d-spacing [Angstroms]	Intensity (100 max.)	F( <i>hkl</i> )	Multiplicity
1	0	1	4.066	1.09	9.40	6
1	0	-1	4.066	0.85	8.31	6
1	1	0	3.677	0.00	0.27	6
2	0	0	3.184	0.24	5.57	6
1	1	-1	3.018	0.25	6.04	6
1	1	1	3.018	100.00	120.34	6
2	0	-1	2.727	0.01	1.45	6
2	0	1	2.727	0.09	3.93	6
0	0	2	2.642	0.04	4.74	2
1	0	-2	2.440	0.08	4.26	6
1	0	2	2.440	0.07	4.03	6
1	2	0	2.407	0.23	7.14	6
2	1	0	2.407	0.10	4.65	6
1	2	-1	2.191	0.07	4.27	6
1	2	1	2.191	0.85	15.00	6
2	1	-1	2.191	0.01	1.50	6
2	1	1	2.191	0.10	5.20	6
1	1	2	2.145	0.22	7.78	6
1	1	-2	2.145	12.90	59.73	6
3	0	0	2.123	13.32	61.29	6
2	0	-2	2.033	0.23	8.36	6
2	0	2	2.033	0.65	14.08	6
3	0	1	1.970	0.13	6.38	6
3	0	-1	1.970	0.12	6.29	6
2	2	0	1.839	0.00	1.26	6
2	1	2	1.779	0.50	13.95	6
2	1	-2	1.779	0.43	12.88	6
1	2	2	1.779	0.03	3.52	6
1	2	-2	1.779	0.03	3.29	6
3	1	0	1.766	0.52	14.28	6
1	3	0	1.766	0.00	0.72	6
0	0	3	1.761	10.25	110.27	2
2	2	-1	1.736	34.55	118.37	6
1	0	-3	1.697	1.42	24.51	6
1	0	3	1.697	0.34	12.00	6
1	3	-1	1.675	0.89	19.62	6
1	3	1	1.675	0.42	13.54	6
3	1	1	1.675	0.00	1.25	6
3	1	-1	1.675	0.58	15.82	6
3	0	2	1.655	0.07	5.37	6
3	0	-2	1.655	0.06	5.26	6

**Table 4.3:** Expected peak positions and intensities for the R-phase powder. Calculated using the structural model of Goryczka and Morawiec, 2004.

transformations. For example, in a diffraction experiment, a first order transformation would see the appearance of new peaks in the spectrum, whereas for a second order transformation, no new peaks would appear, and the original peaks would just shift in position slightly. Ling and Kaplow studied the second-order nature of the B2-R transition in NiTi in a series of classical experiments conducted in 1981 (Ling and Kaplow, 1981). These involved cooling NiTi wire through the R-phase transformation while recording X-ray diffraction spectra at various temperatures. They found the rhombohedral unit cell to continuously distort on cooling, with the measure of that distortion being the decrease in the rhombohedral angle,  $\alpha$ , with decreasing temperature. In diffraction experiments this results in a continuous splitting of R-phase peaks from which the change in rhombohedral angle can be measured. The results of Ling and Kaplow are reproduced in Figure 4.2. The rhombohedral distortion has a strong effect on the strain recoverable via the shape memory effect (Miyazaki et al, 1988). However, while previous studies have focussed on the mechanical behaviour of single crystals, the effects of this distortion on the mechanical behaviour of R-phase-structured polycrystalline NiTi has rarely been studied in the literature.

#### *4.1.4 Multi-step transformation behaviour in nickel-rich alloys*

Differential scanning calorimetry is probably the most popular method of determining the transformation temperatures of shape memory alloys. In the case of binary nickel-titanium, the DSC thermogram recorded usually displays a single peak on heating and a single peak on cooling. In the case of cold-work and annealed alloys then two peaks may be seen on cooling or heating, corresponding to the appearance of the R-phase martensitic

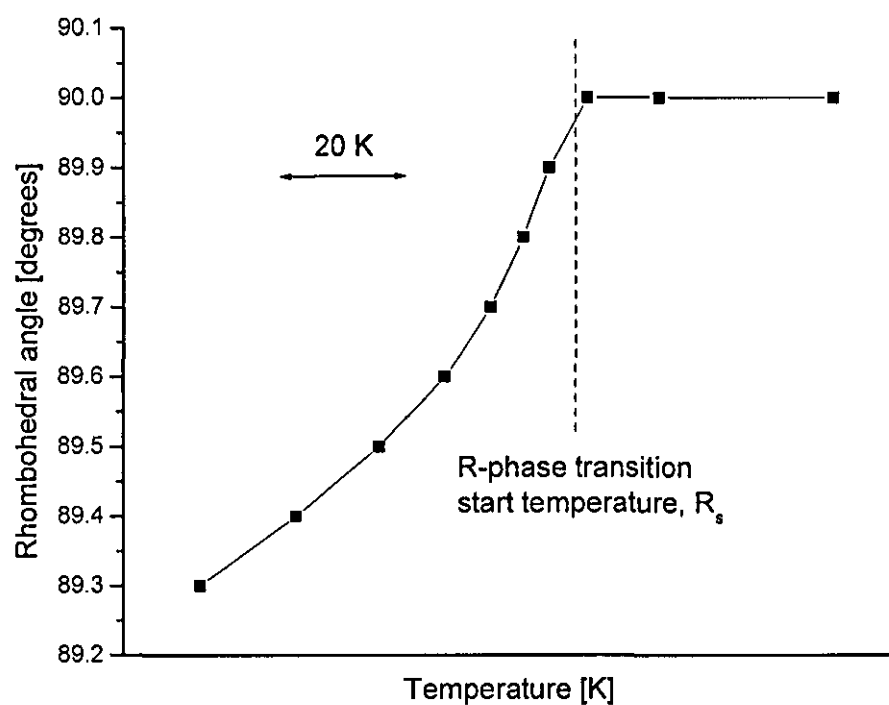


**Figure 4.2:** Evolution of R-phase rhombohedral angle on cooling below the R-phase transformation start temperature,  $R_s$ . Results reproduced from those obtained by Ling and Kaplow (Otsuka, 1990; Ling and Kaplow, 1981).

transformation, which often occurs following thermoemchanical heat treatments (Nam et al, 1990). However, there are occasions when three peaks appear in DSC spectra. Since it is well known that only two types of martensite can be formed in binary Ni-Ti alloys (Morawiec et al, 1997), the origin of the third peak is puzzling and many papers in the literature have been devoted to studying it. 'Multi-step transformation behaviour' is the term commonly used when three peaks are observed on the DSC chart. This multi-step behaviour is very strongly related to the presence of  $\text{Ni}_4\text{Ti}_3$  precipitates in the microstructure.

The multi-step transition behaviour was noted by Bataillard and co-workers in a Ni-Ti alloy containing lenticular  $\text{Ni}_4\text{Ti}_3$  precipitates. They utilised both thermal analysis and electron microscopy to study the multi-step transformation behaviour. They postulated that the multiple peaks were due to separate  $\text{B2} \rightarrow \text{R-phase}$  and  $\text{R-phase} \rightarrow \text{B19'}$  martensite, which occurred inhomogeneously within grains due to a localised stress-field around the coherent precipitates (Bataillard et al, 1998).

Alternatively, Khalil-Allafi and co-workers proposed that the multi-step transformation behaviour has a different origin. Namely that the compositional inhomogeneity, which occurs within grains as the precipitates grow, and the difference in nucleation barriers for the formation of the R-phase and the B19' martensite are the causes of this anomalous behaviour (Khalil-Allafi et al, 2002a).

However, they later discounted both their own and Bataillard et al's interpretations as not fully explaining the observed transformation features and instead proposed that heterogeneous precipitation was the main cause of the multi-step transition behaviour. Precipitates were seen to grow

preferentially on grain boundaries which resulted in an inhomogeneous precipitate microstructure. The centre of grains was found to be largely unaffected by the precipitation process (with short ageing times) with only the precipitate-containing boundaries exhibiting different transformation behaviour (Khalil-Allafi et al, 2002b). Length of ageing time was also found to affect transformation behaviour strongly (Khalil-Allafi et al, 2004).

There are therefore three competing theories regarding the multi-step transformation behaviour: (i) stress fields acting around precipitates, (ii) compositional inhomogeneity due to precipitate formation and (iii) preferential precipitation on grain boundaries (inhomogeneous precipitation). All have been used to try to explain the multi-step transformation behaviour in aged NiTi.

Fan et al have recently tried to solve the mystery of the multi-step behaviour once and for all by a DSC study of NiTi using both single crystals and polycrystals (Fan et al, 2004). Comparison of the single crystal and polycrystal thermal analysis curves find that the multi-step transition behaviour is only observed within polycrystalline samples, thus the grain boundaries, and the preferential precipitation of  $\text{Ni}_4\text{Ti}_3$  on them, is required for multi-step transformation behaviour to be observed. They developed a theory to determine whether multi-step transformation events will occur within the material based on fundamental principles of NiTi decomposition kinetics. The main point which is of relevance to the present study is that an alloy of the composition discussed here should exhibit the multi-stage transition. The three peaks that are observed on cooling are due to the following (Otsuka and Ren, 2005):



- 1<sup>st</sup> peak: B2  $\rightarrow$  R-phase transformation in the grain boundary region containing a large volume of Ni<sub>4</sub>Ti<sub>3</sub> precipitates.
- 2<sup>nd</sup> peak: B2  $\rightarrow$  B19' transformation in the precipitate-free region of the grains (conventional type of transformation).
- 3<sup>rd</sup> peak: R-phase  $\rightarrow$  B19' transformation in the grain boundary region.

For the ageing times and composition of alloy discussed here, it would be expected that the multi-stage transition would be apparent.

#### 4.1.5 Methods of analysis

Both single-peak fitting approach and whole profile analysis of the spectra were carried out. For the single peak approach fits were carried out using the *PeakFit* (version 4) software, distributed by Jandel Software. The profile function used was that developed by Jorgensen, Von Dreele and co-workers (Jorgensen et al, 1978; Von Dreele et al, 1982) and has an asymmetric shape which is appropriate to fit peaks obtained at a time-of-flight neutron source. The function is the result of convoluting two back-to-back exponential functions with a Gaussian and was previously discussed in chapter 2. It was fitted using a constant background using a least-squares routine. The fitted profile was as follows:

$$H(\Delta T) = N[e^u \operatorname{erfc} y + e^v \operatorname{erfc} z] + \text{const.} \quad (4.1)$$

For further details regarding the variables in this function, the reader is referred back to the appropriate part of chapter 2 or to the relevant section of the GSAS manual (Larson and Von Dreele, 2000). In the fitting of profiles only Gaussian width, integrated intensity, peak position and background intensity were allowed to be refineable variables. Such an approach is generally considered to give the smallest errors while still giving a satisfactory fit.

Whole pattern analysis was used to provide an accurate determination of lattice parameters of the phases present. The approach adopted here was to use the Le Bail structureless refinement available within the GSAS program (Larson and Von Dreele, 2000). The Le Bail method uses a dummy atom in place of the actual atomic structure shown in Table 4.2, with the intensities of peaks being allowed to vary irrespective of the structure factors of different peaks, while the lattice parameters are constrained to the symmetry of the unit cell. It is possible to obtain very precise lattice parameters in this way, particularly in strongly textured materials. It is probably best employed when the phase composition is known but can be a useful tool in solving the unit cell atomic arrangement in an unknown powder. In this study the whole pattern method is used to calculate the lattice parameters of the crystalline phases only via the Le Bail method.

Phase fractions have been calculated using the single peak approach in this work using the following equation:

$$\xi_{hkl} = 1 - \frac{I_{hkl}}{I_{hkl}^0}. \quad (4.2)$$

Here,  $\xi_{hkl}$  represents the martensite volume fraction present within a particular grain orientation given by the Miller index  $(hkl)$ .  $I_{hkl}^0$  is the initial integrated intensity of the (austenite or R-phase) peak, with  $I_{hkl}$  the same reflection's integrated intensity at some point along the stress-strain curve (Vaidyanathan et al, 1999).

In a similar way, a macroscopic value for the phase fractions can be worked out if the integrated intensities are summed for all peak of that particular phase within the spectra. Thus global volume fraction,  $\xi_G$ , is determined through equation 4.3:

$$\xi_G = 1 - \frac{I_{total}}{I_{total}^0}. \quad (4.3)$$

Where  $I_{total} = \sum I_{hkl}$  and  $I_{total}^0 = \sum I_{hkl}^0$ . (Sittner et al, 2002).

Lattice strain,  $\varepsilon_{hkl}$ , is calculated in the usual way for specifically oriented grains via equation 4.4:

$$\varepsilon_{hkl} = \frac{d_{hkl} - d_{hkl}^0}{d_{hkl}^0}. \quad (4.4)$$

Where  $d_{hkl}$  is the d-spacing of a particular austenite/R-phase Bragg peak at some value of stress or strain, and  $d_{hkl}^0$  is the d-spacing of the same reflection at a nominally zero strain.

#### *4.1.6 Objectives of present study*

A great deal of the research effort has been expended on investigating the effect of ageing, i.e. the role of precipitation, on the thermal behaviour of the alloy. That is, the multi-step transformation behaviour which often results from ageing. However, there have been comparatively few studies on the effects of ageing on the mechanical behaviour (Gall et al, 1999a), with none attempting to resolve both the microstructural details simultaneously with the macroscopic stress-strain curve, as is attempted here.

The currently reported experimental study involves the deformation behaviour of aged NiTi.

## **4.2 Experimental details**

### *4.2.1 Material and heat treatment*

The alloy used in this study had nominal composition Ni-49.2Ti (at.%). The material was obtained from Memory Metalle, Germany, and was delivered in rod form with a length of 0.8 m and rod diameter of 12.7 mm. Small cylindrical samples were machined from this as-received material using a carbide cutting tool due. The machined cylinders measured approximately 27 mm in length and 9 mm in diameter, which is a suitable size for use in diffraction experiments using ENGIN-X as the large size increases the diffraction signal without absorption of the neutrons becoming too much of a problem. Three samples were cut specifically for the diffraction experiments, and several extra for calorimetry testing.

In the as-machined state, the samples were subjected to a solution heat treatment designed to place the material into a known microstructural state, i.e. single phase, which may not have been the case after machining. The solution heat treatment consisted of the following: heating under vacuum at 850 °C for 0.5 h followed by quenching into water at room temperature. Such a heat treatment, according to the phase diagram (Massalski et al, 1990), gives a single phase microstructure at room temperature.

In addition to this, ageing heat treatments were performed on the samples as follows: one sample was aged at 400 °C for 1.5 hours, while another was aged for 400 °C for 20 hours, followed by immediate water quenching to room temperature to avoid further decomposition. Both samples had been subjected to the solution heat treatment described above before ageing.

#### *4.2.2 Experimental arrangement*

The ENGIN-X instrument at ISIS spallation neutron source was used for this investigation. The experimental set-up for this instrument has been discussed extensively in chapter 2. The usual arrangement of detector banks situated at  $\pm 90$  degrees to the incident beam is used. Samples were stressed using the 50 kN capacity INSTRON loading rig available on ENGIN-X. Macroscopic sample strain was determined through the use of a clip-on extensometer. Both of these enabled a macroscopic stress-strain curve to be collected during the deformation experiments. All tests were conducted in compression with diffraction spectra recorded during temporary halts in the loading process. All tests were conducted at room temperature. Compressive stresses and strains are reported as positive quantities.

Therefore, to conclude this section, three different compression experiments were conducted and will be discussed in the Results and Discussion section:

- Compression of solution heat treated Ni-Ti.
- Compression of solution heat treated Ni-Ti after ageing at 400 °C for 1.5 hours.
- Compression of solution heat treated Ni-Ti after ageing at 400 °C for 20 hours.

### **4.3 Results and discussion**

#### *4.3.1 Calorimetry results*

Differential scanning calorimetry tests were conducted on samples from material subjected to each of the three heat treatments. Samples were spark-cut from the bulk of the material in order not to induce artificial microstructural changes, such as increase dislocation density, which could be brought about sawing or other mechanical cutting methods.

Figure 4.3 shows the DSC curves for the tested materials. The solution treated material, which has not been subjected to any ageing treatments, displays a classical single step transformation on both cooling and heating. This is obviously associated with the  $B2 \rightarrow B19'$  martensitic transformation on cooling and the reverse  $B19' \rightarrow B2$  transformation on heating. Prior to the mechanical test, the sample was heated in water to 100 °C and then allowed to cool to room temperature. The transformation temperatures can

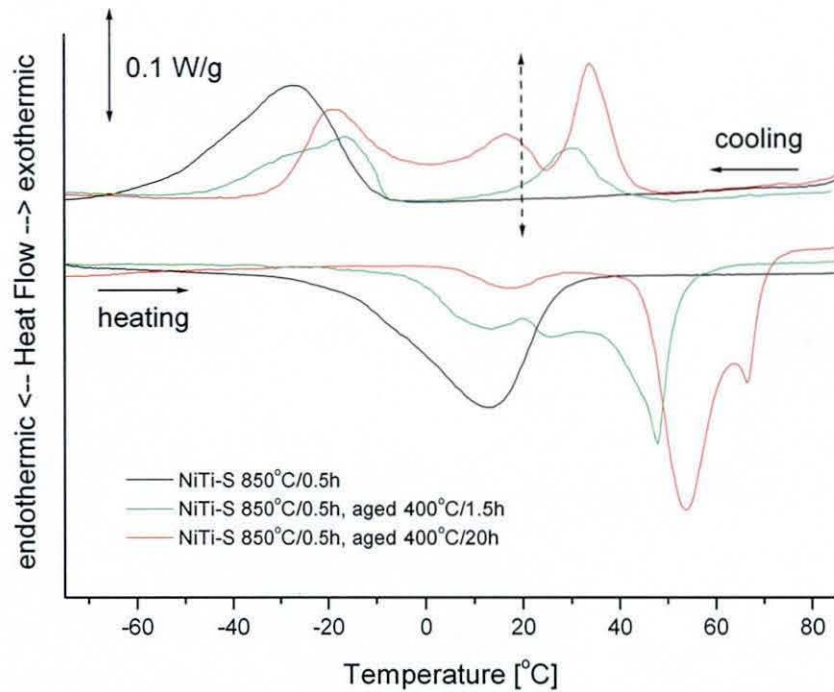


**Figure 4.3:** Differential scanning calorimetry chart recordings for all samples. The broken arrow indicates the temperature at which the deformation experiments were conducted (room temperature). Samples were heated to 100 °C prior to the experiment and then allowed to cool to room temperature.

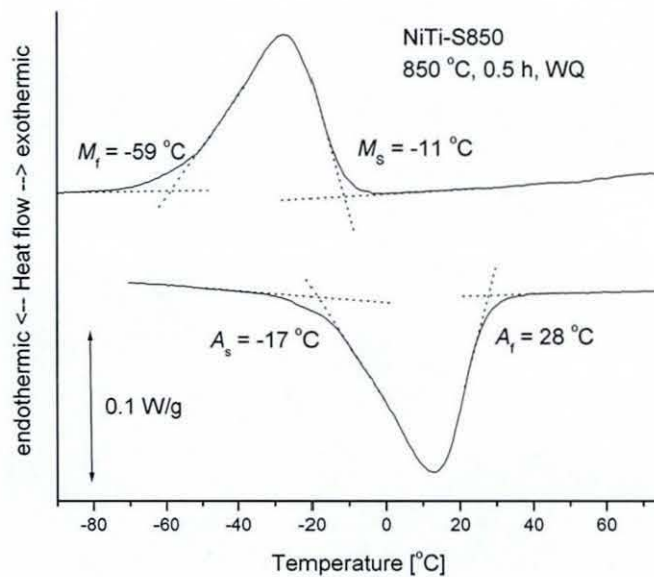


**Figure 4.4:** Baseline construction used in determining transformation temperatures of shape memory alloys. DSC curve is that from the solution treated alloy discussed in this chapter.

be measured from the diagram - Figure 4.4 shows the construction used in measuring these values - are found to be:  $M_s = -11\text{ }^{\circ}\text{C}$ ,  $M_f = -59\text{ }^{\circ}\text{C}$ ,  $A_s = -17\text{ }^{\circ}\text{C}$  and  $A_f = 28\text{ }^{\circ}\text{C}$ .

Thus, this material is expected to be fully austenitic at the test temperature.

The two aged samples both show multi-step transformation behaviour, with three peaks on cooling and three on heating, indicating that the precipitated microstructure is present in these samples. The occurrence of three peaks within the spectra indicates that the R-phase, in addition to the conventional B19' monoclinic martensite will be a possible transformation product in these two samples.

In this alloy the R-phase appearance can be solely attributed to the presence of the  $\text{Ni}_4\text{Ti}_3$  precipitates since the ageing treatments were carried out on a solution treated alloy which can be assumed to have a minimal value of dislocation density.

The broken arrow in Figure 4.3 indicates the deformation temperature for all samples. In the same way as the solution heat treated sample, the aged samples were both heated to  $100\text{ }^{\circ}\text{C}$  and allowed to air cool to room temperature prior to the mechanical tests. Both samples will therefore have some kind of martensite present within their microstructure at the beginning of the deformation experiments.

#### *4.3.2 Mechanical response*



Figure 4.5 shows the macroscopic stress-strain curves for all samples. A quasi-static strain rate was used during the loading phases. The solid square points on the figure indicate the stress/strain levels at which the diffraction spectra were recorded. Only the loading portion of the stress-strain curve is shown in the figure for the solution heat-treated sample. Typically around 20-40 minutes was required to collect good quality data. This is longer than is required for most materials studied using ENGIN-X and is due to the lower symmetry nature of the martensite phases, i.e. monoclinic crystal structure.

The mechanical properties of each sample (tangent modulus and yield/transformation stress) can be measured from the data in Figure 4.5. These are summarised in Table 4.4. The modulus for the aged materials was determined as the tangent modulus at 0.2 % strain due to non-linearities in the stress-strain curve at low strains (Higgins, 2001). Yield/transformation stresses were measured in the conventional way using the 0.2 % offset method.

It can be seen that the moduli for the three samples differ. In the case of the solution heat treated alloy the value of 68 GPa is of the right order of magnitude for that expected of austenitic NiTi.

The moduli of the aged materials are much lower however, with some non-linearity in the initial stages of deformation in both cases. The ageing of the solution treated alloy has clearly had a strong effect on the value of the tangent modulus, with its value decreasing with increasing ageing time.

The yield behaviour is also clearly different for all samples, with marked difference in the yield stress of each material. Again the reason for this is

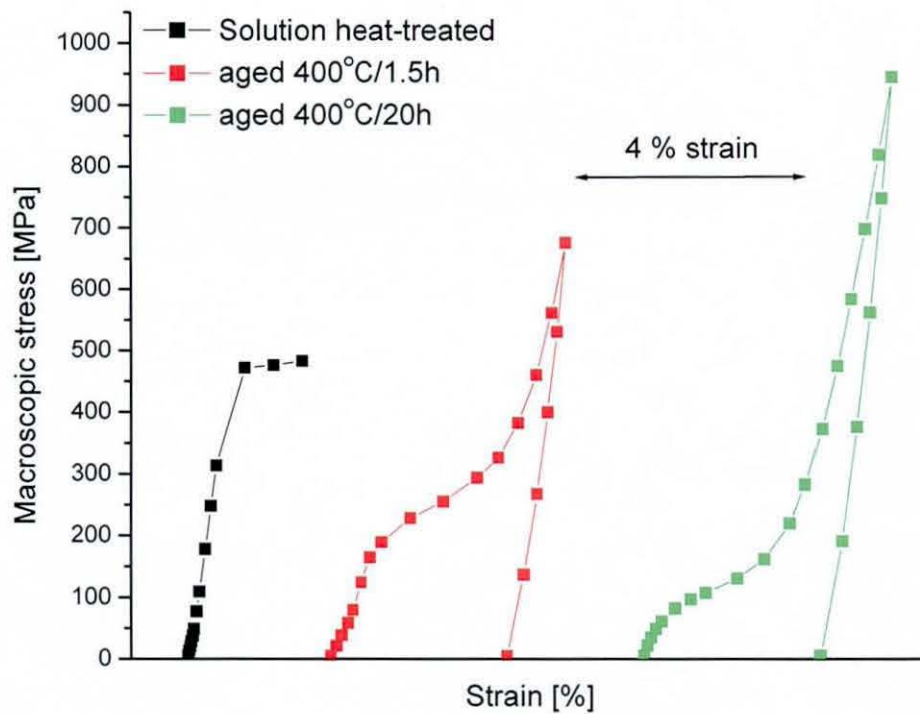


**Figure 4.5:** Stress-strain curves for heat treated samples. A quasi-static loading rate was used. The solid square points denote the stress/strain values at which diffraction spectra were collected. Compressive stresses and strains are represented as positive quantities in the figure.

Sample	Modulus [GPa]	Yield/transformation stress [MPa]
Solution heat-treated	68	470
Aged 400 °C/1.5h	19	190
Aged 400 °C/20h	15	87

**Table 4.4:** Mechanical properties of the heat treated samples determined from the stress-strain curves in Figure 4.5. The modulus for aged materials was determined as the tangent modulus at 0.2 % strain due to non-linearities in the stress-strain curve. Conventional Young's modulus was measured for the unaged material.

clearly the microstructure induced by the ageing treatment. The yield stress can be seen to decrease with increasing ageing time, in a similar way to the modulus values in Table 4.4.

The large changes that can be observed in the macroscopic mechanical behaviour can be clearly related to the change in microstructure caused by the ageing treatment. The diffraction experiments discussed within the next section will allow this evolution in this microstructure (phase fraction and internal strain evolution) to be followed as the deformation proceeds.

#### *4.3.3 Diffraction results*

##### *4.3.3.1 Room temperature microstructures*

It is clear from examining the macroscopic stress-strain curves shown in Figure 4.5 that the mechanical properties of the samples at room temperature are quite different. This must be ascribed to the change in microstructure brought about by ageing, i.e. precipitation phenomena.

The result of the precipitation on the microstructure of the alloy at room temperature is quite clearly documented by examining the diffraction spectra collected under zero strain.

Figures 4.6a, 4.6b and 4.6c show room temperature diffraction spectra (collected in the axial orientation) for all samples. Small d-spacing ranges, centred on the main austenite (100), (110) and (111) reflections respectively are focussed upon.

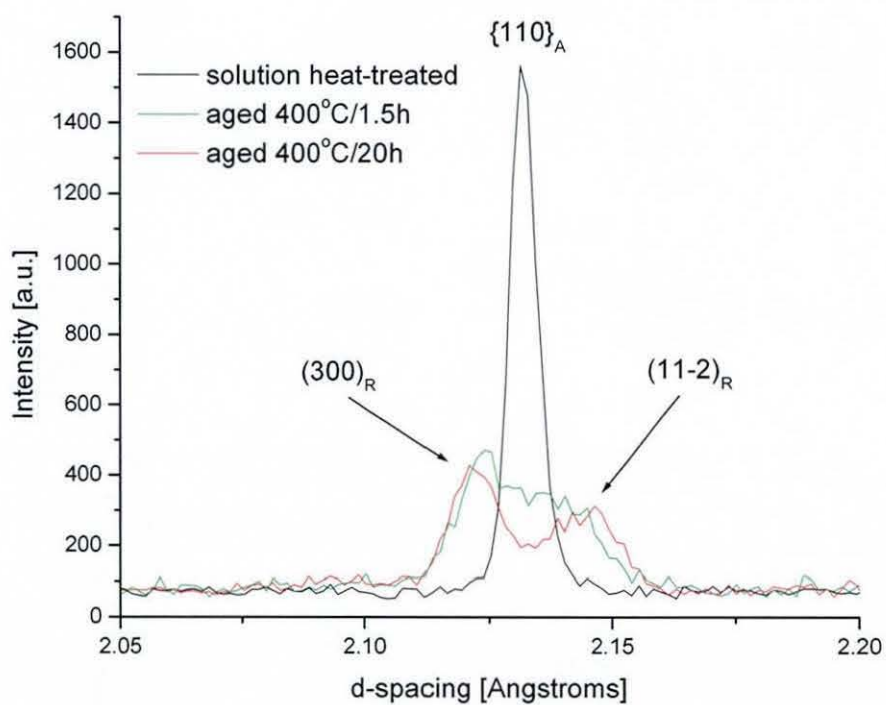
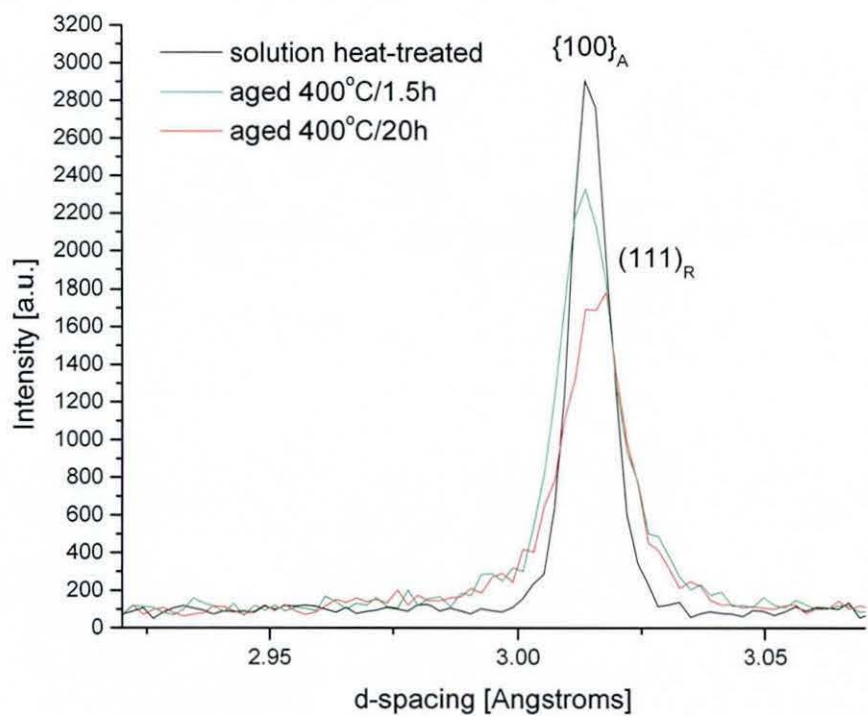


**Figure 4.6a (upper) and Figure 4.6b (lower):** Room temperature diffraction spectra collected for solution heat treated, and samples aged at 400 °C (continued overleaf).



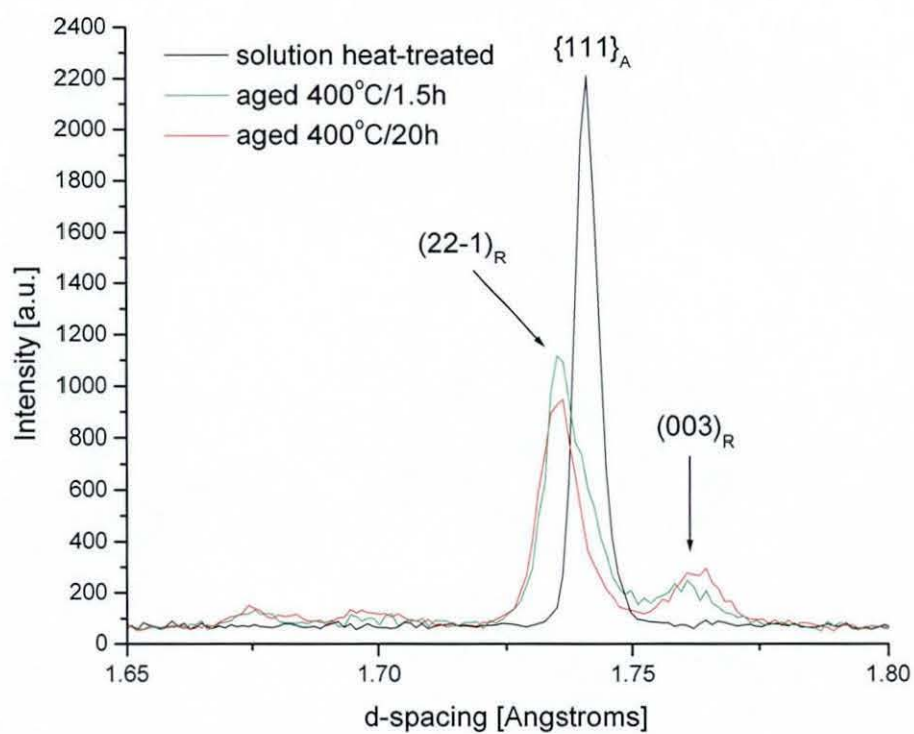


**Figure 4.6c:** Room temperature diffraction spectra collected for solution heat treated, and samples aged at 400 °C.

Figure 4.6a shows the room temperature diffraction spectra around the  $(100)_A$  Bragg peak. Clearly for the solution heat treated sample the material is in the austenite state, with the aged samples displaying a single peak also but of slightly greater widths and reduced intensity.

The increased peak width and reduced intensity can be rationalised on the basis of the formation of the coherent  $Ni_4Ti_3$  precipitates. The coherency stresses which arise due to precipitation of this type are classed as type III microstresses and thus broaden the reflection profiles when present (Warren and Averbach, 1950).

The decrease in intensity is related to the formation of the precipitates. Since these are very small for short ageing times, with diameters typically of the order of 100 nm (Gall et al, 1999b), they only form extremely broad diffraction peaks (which are very small anyway due to the low volume fraction of  $Ni_4Ti_3$ ) and thus only contribute to the background signal.

Since the deformation is being carried out at room temperature, it would be expected from examining the DSC plots in Figure 4.3 that some form of martensite would be present in the microstructure. It is clear from examination of the spectrum in Figure 4.6a that no B19' martensite has been formed. This leaves the R-phase as the only other option.

In diffraction experiments, due to the crystallography of the  $B2 \rightarrow R$ -phase transformation, R-phase formation is seen by a splitting of all major austenite reflections except the  $(100)_A$  (Lukas, 2002). Thus it would not be expected that the  $(100)_A$  should split and only by looking at further reflections will a full picture of the phase composition be found.

Figures 4.6b and 4.6c clearly show the splitting of the  $(110)_A$  and  $(111)_A$  peaks respectively. Thus there is conclusive proof that the R-phase has been stabilised at this temperature due to the formation of  $Ni_4Ti_3$  precipitates. It therefore appears, from examination of the spectra, that a complete austenite to R-phase transformation has occurred.

However, it should be noted that for Figs. 4.6b and 4.6c the R-phase peaks in the sample aged for 20 hours have a greater separation than do those for the sample aged for 1.5 hours. This behaviour can be ascribed to the second order nature of the R-phase transformation; namely, that it exhibits a continuous decrease in rhombohedral angle with decreasing temperature (as discussed in section 4.1.3 and shown in Figure 4.2).

Thus, while both aged samples are composed of the R-phase – plus a certain volume of precipitates – and therefore have the same crystal structure, they have slightly different lattice parameters due to the difference in rhombohedral angle. In order to measure the difference a whole pattern Le Bail fit of the diffraction spectra was performed, the results of which are shown in Figure 4.7.

The details of the fit are as follows: the crystal structure data of Goryczka and Morawiec, i.e. lattice parameter of  $a = 7.3541$  Angstroms and  $c = 5.2834$  Angstroms (hexagonal indices) were used as the basis for the refinement (Goryczka and Morawiec, 2004). The Le Bail fit was carried out using the GSAS diffraction pattern analysis software in which a least-squares refinement was performed. Refineable parameters were: lattice parameters, background terms and profile coefficients. The intensity varies automatically in a Le Bail fit. Only the R-phase structure was assumed to be present.

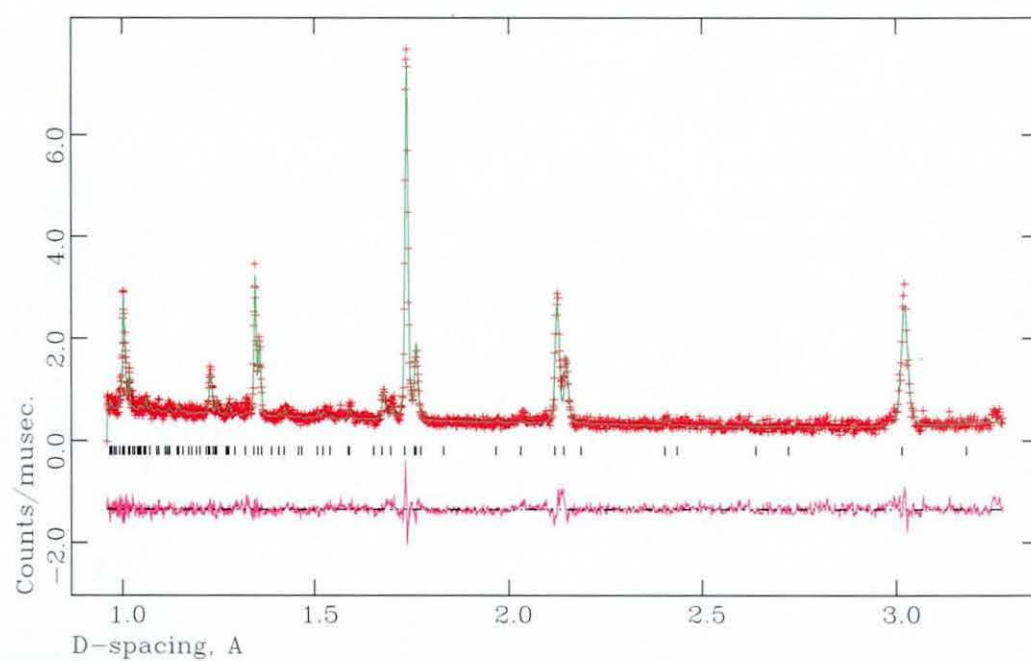
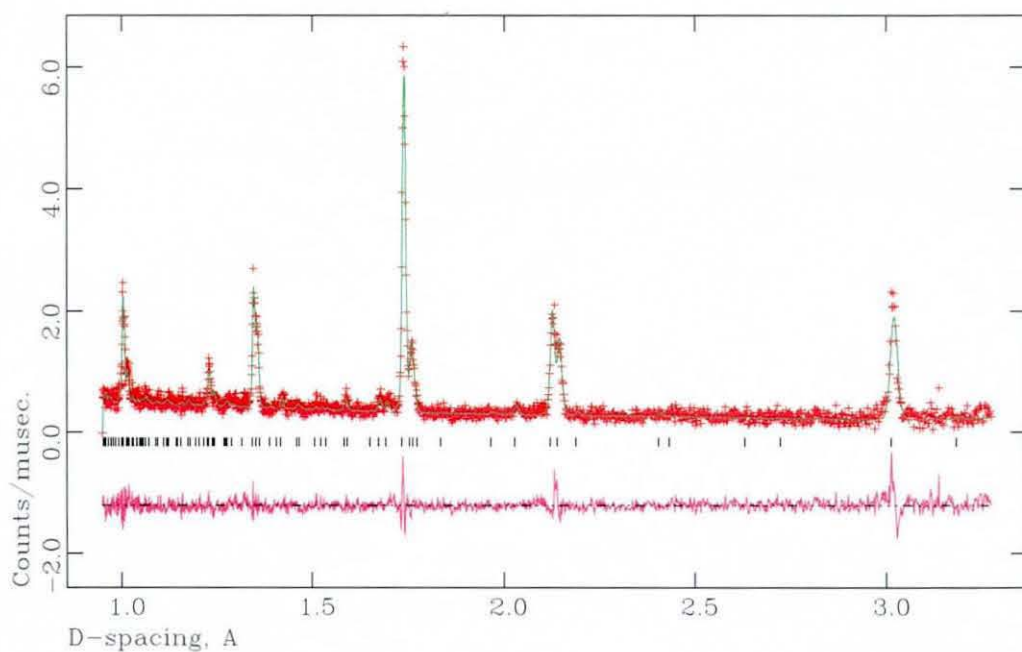


**Figure 4.7:** Le Bail refinement of diffraction spectra (axial orientation) for the sample aged at 400 °C for 1.5 hours (upper diagram) and 20 hours (lower diagram). The red cross marks are the experimental data, the green line the Le Bail fit to the data, the black tick marks are the expected reflection positions, and the purple curve is the experimental data/Le Bail fit difference.



The lattice parameter results from the fit were as follows. For the sample aged for 1.5 h:  $a = (7.3576 \pm 0.0003)$  Angstroms and  $c = (5.2724 \pm 0.0005)$  Angstroms, with those for the sample aged for 20 hours being:  $a = (7.3520 \pm 0.0002)$  Angstroms and  $c = (5.2846 \pm 0.0004)$  Angstroms.

From this information the rhombohedral distortion of the R-phase can be calculated by converting the hexagonal R-phase unit cell to a rhombohedral one. Thus the calculated rhombohedral angle for both samples are: for the sample aged 1.5 hours,  $\alpha = 89.49^\circ$  and for the sample aged for 20 hours,  $\alpha = 89.37^\circ$ . Due to the very small error in refined lattice parameters for the hexagonal phase it is estimated that the error is no more than  $\pm 0.01^\circ$  in the calculated rhombohedral angle. The rhombohedral angle of the R-phase formed therefore decreases with increasing ageing time.

This behaviour is due to the composition of the  $\text{Ni}_4\text{Ti}_3$  precipitates. Due to their being nickel-rich, their formation results in a depletion of nickel content in the matrix material. As such the martensitic transformation temperatures shift to higher temperatures. The depletion of the matrix nickel content will be greater in the case of the sample aged for 20 hours and this sample will have higher R-phase transformation temperatures as a result. This means that there is much a greater degree of under-cooling below the  $R_s$  temperature for the sample aged for 20 hours than there is for the sample aged for 1.5 hours. Thus the R-phase shows a smaller rhombohedral angle for the 20 hour-aged sample than it does for the sample aged for 1.5 hours.

#### *4.3.3.2 Deformation of solution heat treated sample*

Single-peak fitting of the diffraction spectra for the austenite (100), (110) and (111) reflections was carried out. The profile function of Jorgensen et al and Von Dreele et al discussed in the Introduction was used to perform all peak fits. Only the peak position, width and integrated intensity were allowed to vary in the fit.

From these values the orientation-specific internal strains and texture evolution during the deformation can be evaluated and correlated with the macroscopic data of the stress-strain curves.

The profile evolution of the (100)<sub>A</sub>, the (110)<sub>A</sub> and the (111)<sub>A</sub> peaks is shown in Figures 4.8a-c.

Since the material is in the fully austenite state prior to deformation, then the applied stress causes the peaks to shift in accordance with their elastic constants until a critical stress is reached and stress-induced transformation to the B19' phases begins, with the transfer of intensity to a single preferred peak, i.e. variant. Figure 4.9 shows the individual lattice strain responses calculated for the austenite reflections with the diffraction elastic constants calculated from linear fits to the data displayed in Table 4.5. It is clear that the deformation for this solution treated, unaged alloy is related to the stress induced B2 → B19' martensitic transformation. This behaviour has been discussed for a solution treated Ni-Ti alloy of slightly different composition in Chapter 3 and the values for the diffraction elastic constants and intensity evolution of the profiles agree with the results presented there.

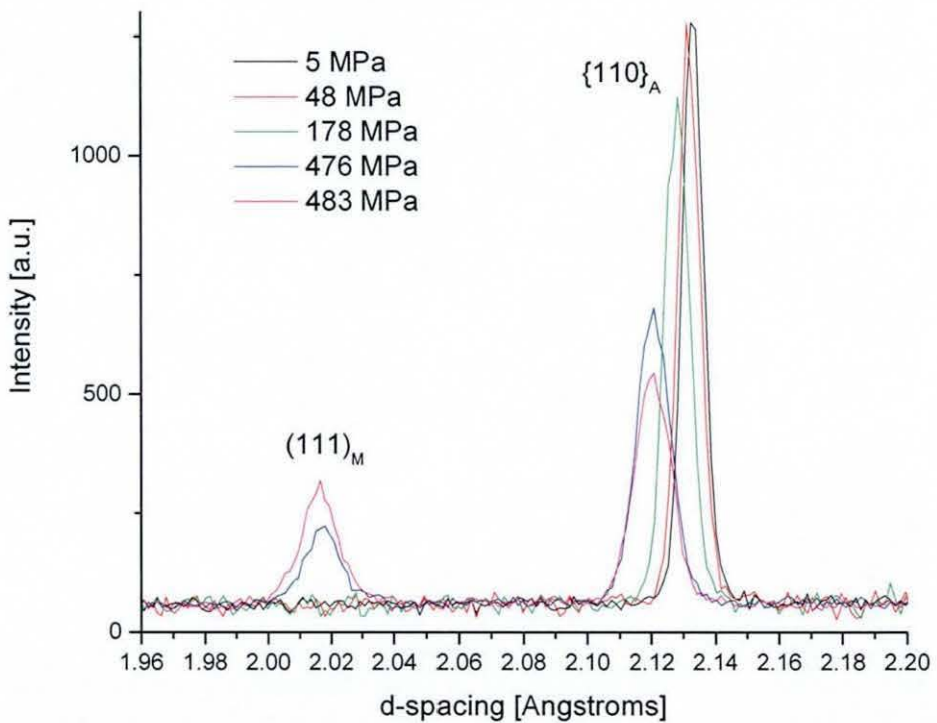
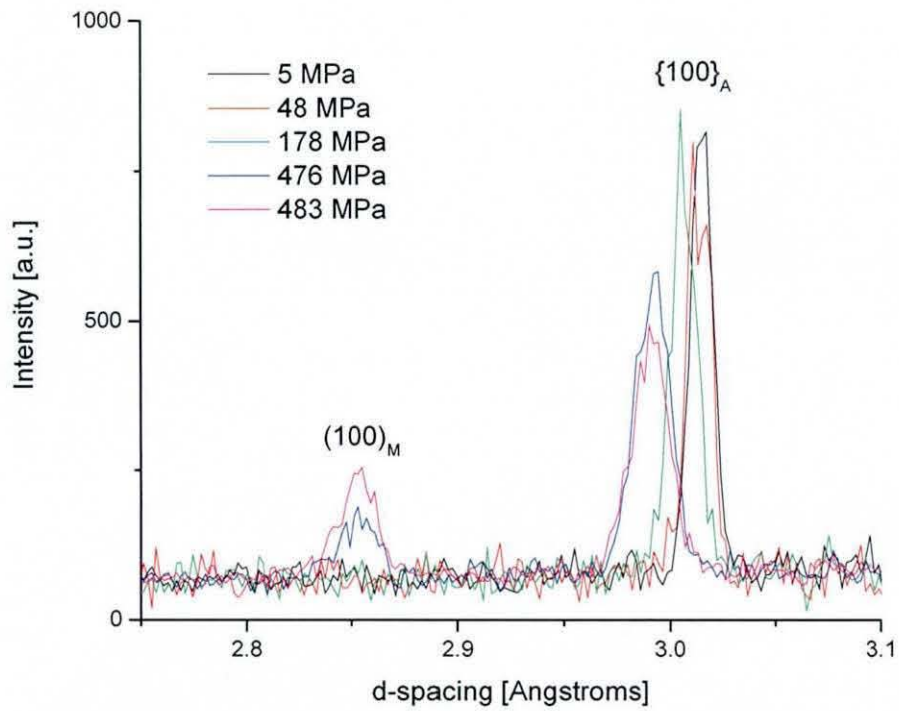


**Figure 4.8a (upper) and Figure 4.8b (lower):** Diffraction spectra recorded for the solution heat treated sample in the fully austenitic state prior to deformation (continued overleaf).

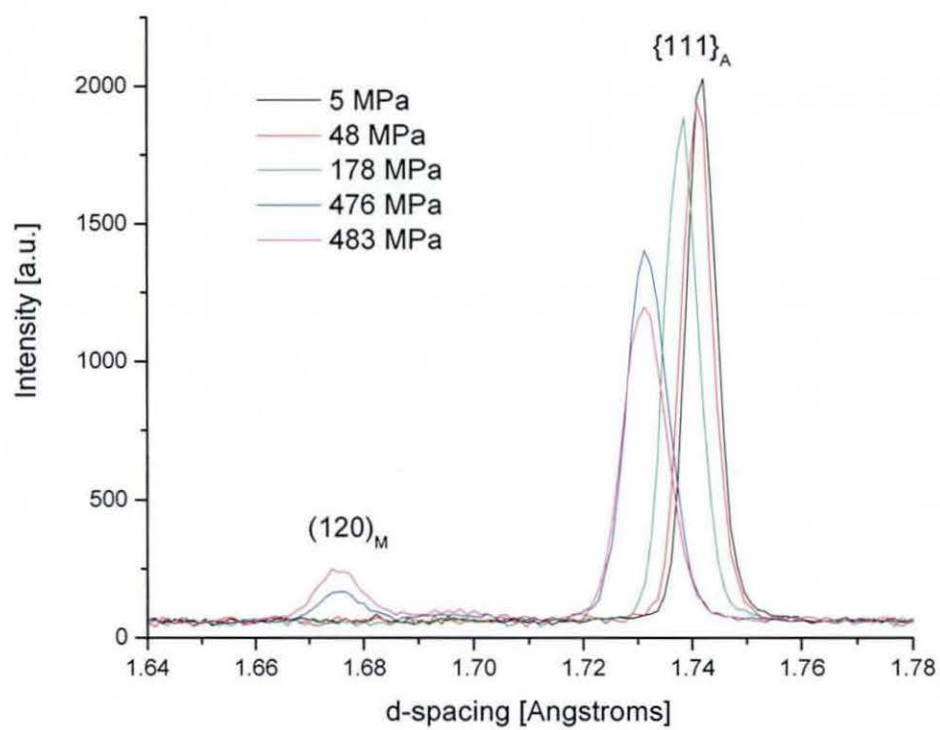


**Figure 4.8c:** Diffraction spectra recorded for the solution heat treated sample in the fully austenitic state prior to deformation.

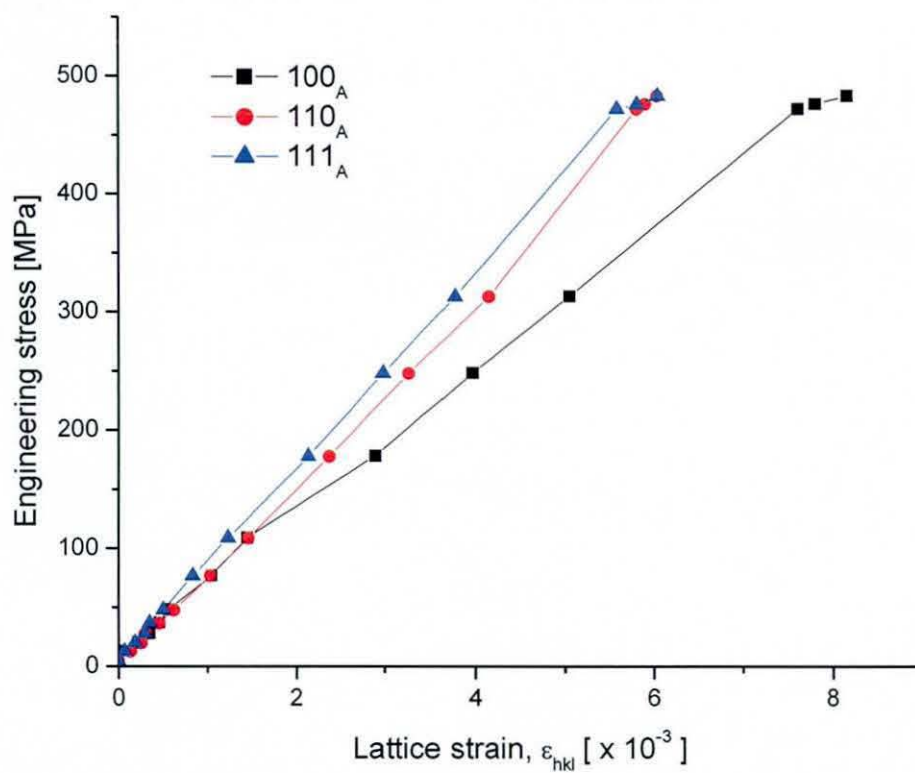


**Figure 4.9:** Lattice strain response for austenite reflections from the solution heat treated sample as a function of applied stress. Compressive stresses and strains are represented as positive quantities in the figure.

Austenite reflection index ( <i>hkl</i> )	Diffraction elastic constant [GPa]
(100)	60
(110)	75
(111)	81

**Table 4.5:** Diffraction elastic constants for austenite reflections obtained from linear fits to the data shown in figure 4.9.



#### *4.3.3.3 Sample aged at 400 °C for 1.5 hours*

Figures 4.10a-c shows the profile evolution for the main R-phase reflections, i.e. those derived from the  $(100)_A$ ,  $(110)_A$  and  $(111)_A$  peaks, for the sample aged at 400 °C for 1.5 hours.

4.10a shows the evolution of the R-phase peak derived from the  $(100)_A$  grains oriented with lattice-plane normals parallel to the applied load (axial geometry). This is indexed in the trigonal structure as the  $(111)_R$  plane. Due to the crystallography of the  $B2 \rightarrow R$ -phase transformation, this is the only peak that does not split.

Under an applied stress, the peak is observed to shift and then gradually decrease in intensity while there is a concomitant increase in the intensity of the  $(100)_M$  B19' martensite peak. This peak represents the formation of particular martensite variants (which are indistinguishable from one another in diffraction experiments) which offer a maximum amount of strain in the direction of the applied stress. These variants, which form in the originally  $(100)_A$  oriented grains, are the same as those which form preferentially during the stress induced  $B2 \rightarrow B19'$  martensitic transformation seen in the solution heat-treated sample in Figure 4.8a.

Figure 4.10b shows the diffraction profile evolution of those R-phase reflections derived from the  $(110)_A$  austenite grains. It can be seen that no austenite remains in the sample with the split reflections indicating the formation of the R-phase via the rhombohedral distortion of the austenite unit cell. The relative intensities of these two peaks provides an indication of the R-phase variant microstructure existing within this particular grain family. Each peak corresponds to the formation of two variants

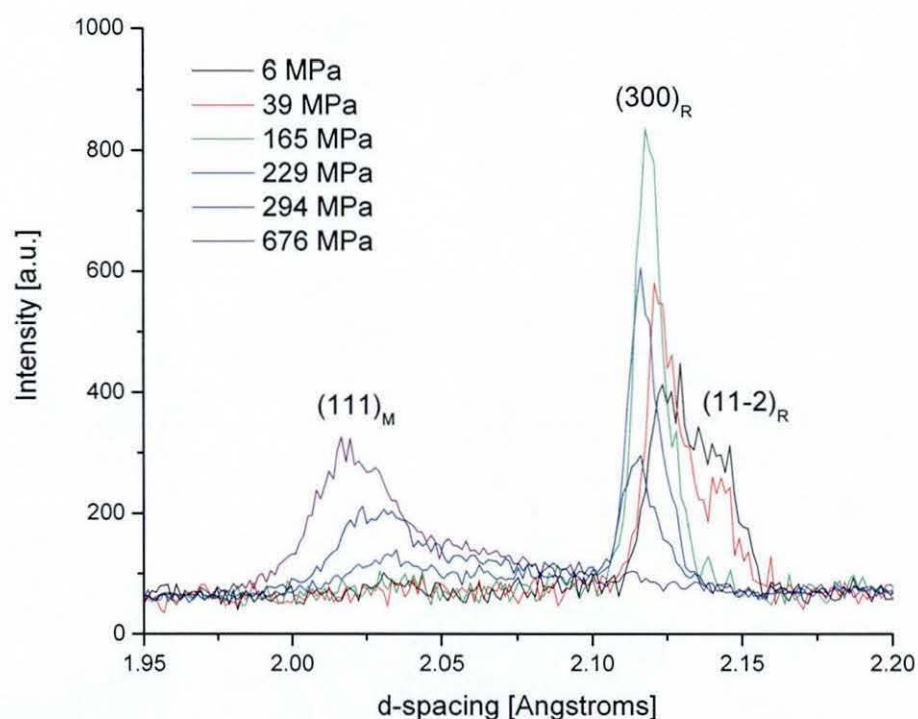
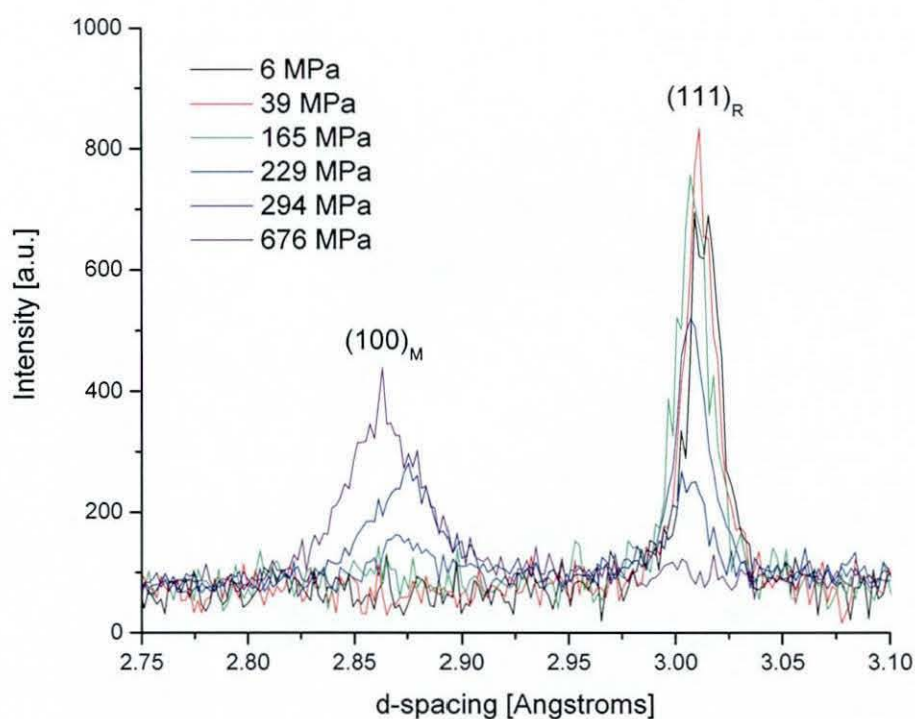


**Figure 4.10a (upper) and Figure 4.10b (lower):** R-phase diffraction profile evolution under the applied stress for peak derived from the  $(100)_A$  oriented grains (Fig. 4.11a) and those derived from the  $(110)_A$  oriented grains (Fig. 4.11b). Martensite reflections appearing have the subscript 'M'. Sample aged for 1.5 hours at 400 °C.

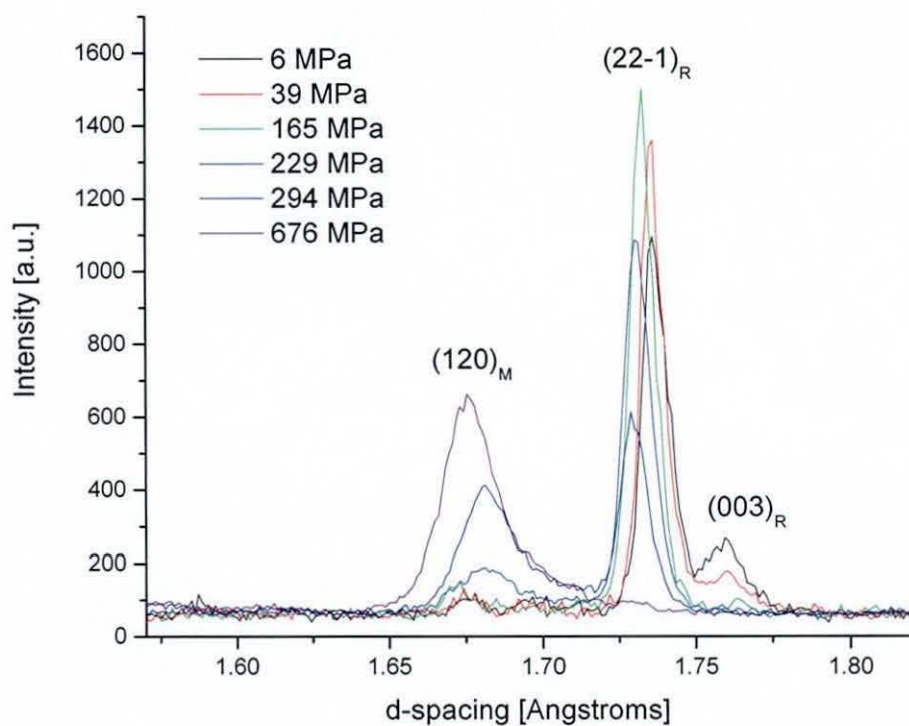


**Figure 4.10c:** R-phase diffraction profile evolution under the applied stress for peak derived from the  $(111)_A$  orientation. Martensite reflections appearing have the subscript 'M'. Sample aged at 400 °C for 1.5 hours.



(indistinguishable from one another in diffraction). The  $(300)_R$  reflection represents those variants orientated such that they provide a compressive strain in the direction of the applied stress and the  $(11-2)_R$  represent those which offer a tensile stress in the direction along the axis of the cylindrical test-piece.

Under stress free cooling an equal fraction of the four variants grows with each particular grain family, separated by interfaces. Since the R-phase is a thermoelastic martensite it forms a twinned microstructure when allowed to form under stress-free conditions. Thus by following the intensity changes of these peaks, the detwinning process in the  $(110)_A$  grain family may be followed.

It can be seen from examination of Figure 4.10b that the intensity begins to switch from the  $(11-2)_R$  peak to the  $(300)_R$  at an early stage in the deformation. This is related to the detwinning of the R-phase. This is then followed by the growth of a single martensite peak, the  $(111)_M$ , which is again the same one observed in the stress-induced transformation discussed above. Again, it is seen that the deformation of the twinned R-phase results in the formation of a preferential B19' variant, i.e. that which provides the maximum strain in the direction of the applied stress.

Figure 4.10c shows how the R-phase diffraction profiles derived from the 111 austenite grains evolve with applied stress. Again the original  $(111)_A$  peak is split due to the formation of the R-phase, into the R-phase  $(22-1)_R$  and  $(003)_R$  peaks. Which corresponds to the formation of three indistinguishable variants offering compressive strain in the direction of the applied stress, while the  $(003)_R$  intensity corresponds to the appearance of the R-phase variant capable of providing tensile strain along the stress-axis.

All variants are apparent due to the stress-free cooling of the sample prior to test.

The application of stress causes the detwinning of the R-phase. Since the stress is compressive the twinning deformation favours the growth of the variants offering the largest strain in the direction of the applied stress. Thus the  $(22-1)_R$  peak is seen to increase in intensity with increasing applied stress. The compression-favoured martensite  $(120)_M$  peak is seen to grow after this with an associated decrease in the intensity of the  $(22-1)_R$  reflection. Again, this is the preferential martensite variant which is formed during stress-induced  $B2 \rightarrow B19'$  martensite transformation.

All of these observation can be made quantitative by considering the evolution of the integrated intensity of the R-phase peaks which also allows quantitative phase analysis to be performed and correlated with the features of the macroscopic stress-strain curve.

Figure 4.11 shows the evolution of R-phase reflection intensity obtained from single-peak fitting of reflections. The R-phase intensity changes from almost the very beginning of the test in the case of all peaks except the  $(111)_R$ . This is due to the detwinning of the thermally induced R-phase which possesses a self-accommodated structure similar to that of the  $B19'$  martensite after stress free cooling. An interesting result is that the detwinning process begins in the grains at a very low stress – intensity changes are seen at as low a stress as 25 MPa which indicates that there is very little resistance to the movement of the interfaces between R-phase variants.

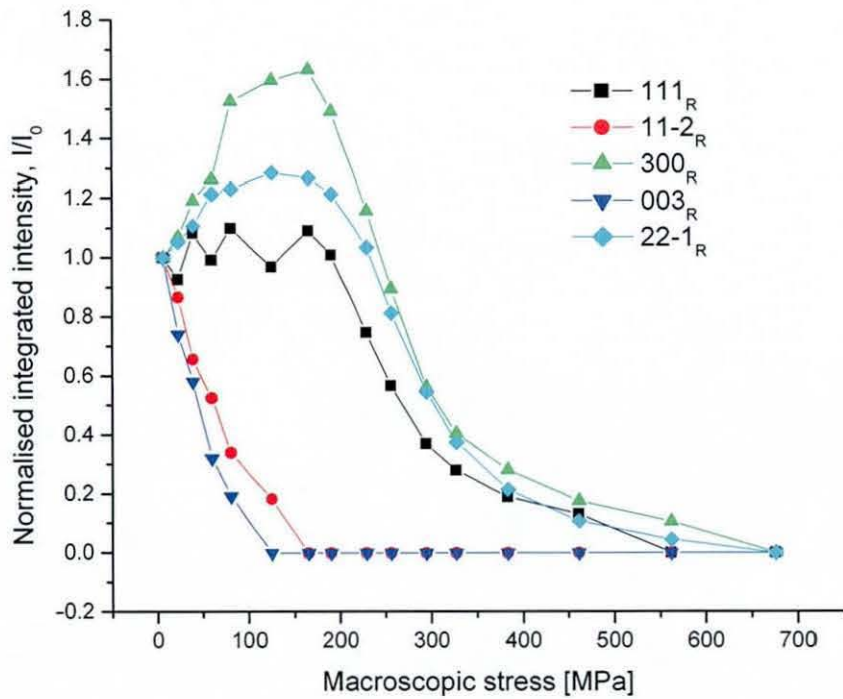


**Figure 4.11:** Integrated intensity evolution of R-phase reflections for NiTi sample aged at 400 °C for 1.5 hours. Intensities are normalised with respect to their starting values. The macroscopic stress is compressive and represented as a positive quantity in the figure.

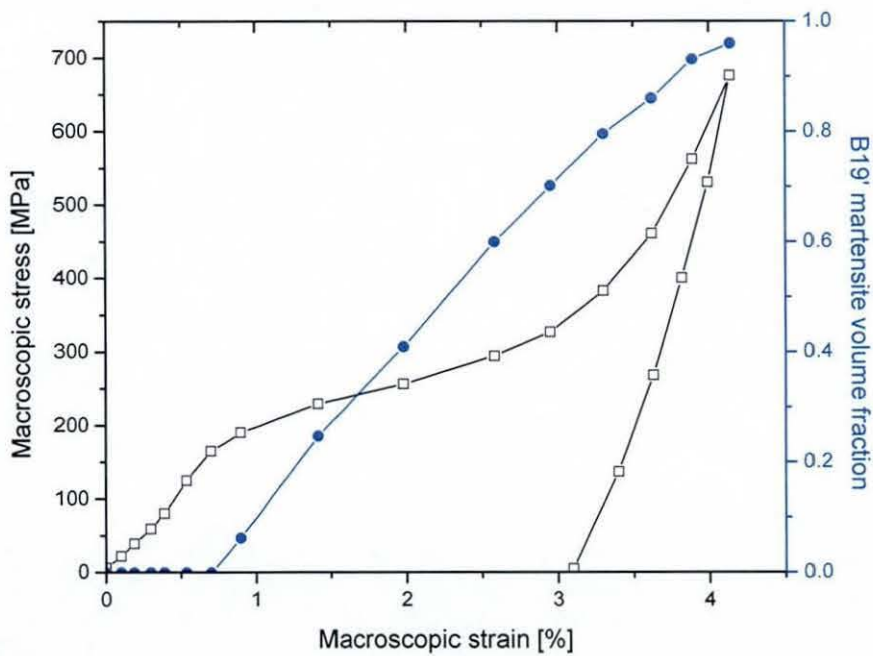


**Figure 4.12:** Global B19' martensite phase volume fraction correlated with the macroscopic stress-strain curve. Compressive stresses and strains are represented as positive quantities in the figure.



The intensity changes continue with the applied stress until a plateau is reached indicating that the detwinning process has been exhausted and a single variant remains within the particular grain orientation. After this, stress-induced transformation to the B19' phase begins and there is a decrease in R-phase reflection intensity. The  $(300)_R$  peak appears to decrease at a faster rate than the other and therefore this orientation appears to be preferentially oriented for  $R \rightarrow B19'$  transformation.

Figure 4.12 displays the global volume fraction of B19' martensite as the deformation proceeds, based on the combined intensities of the R-phase reflections and calculated using equation 4.3. The macroscopic yield of the sample is clearly correlated with the formation of the B19' martensite. The volume fraction of precipitates is estimated as 4 % based on intensity measurements of the  $(111)_R$  R-phase peak. The martensite volume fraction therefore reaches a plateau at a value of 0.96 in Figure 4.12.

It is also possible to obtain lattice strain data from those peak which are strong enough in intensity to be able to reliably fit. Lattice strain data from peaks  $(111)_R$  and  $(22-1)_R$ , both of which are compression favoured peaks. The lattice strain evolution with applied stress for these two peaks is shown in Figures 4.13a and 4.13b. The  $(11-2)_R$  and  $(300)_R$  peaks were too closely overlapped to enable a precise determination of position, thus the strain for these peaks is not reported. From the initially linear regions of the stress-lattice strain plots, the diffraction elastic constants for these two reflection can be calculated: They were measured as 53 GPa for the  $111_R$  peak, and 65 GPa for the  $22-1$  peak. These two diffraction elastic constants are quite different to their parent austenite reflections the  $(100)_A$  and the  $(111)_R$  measured in the compression test of the solution heat treated sample and the origin of this is likely the difference in elastic properties of the R-phase and

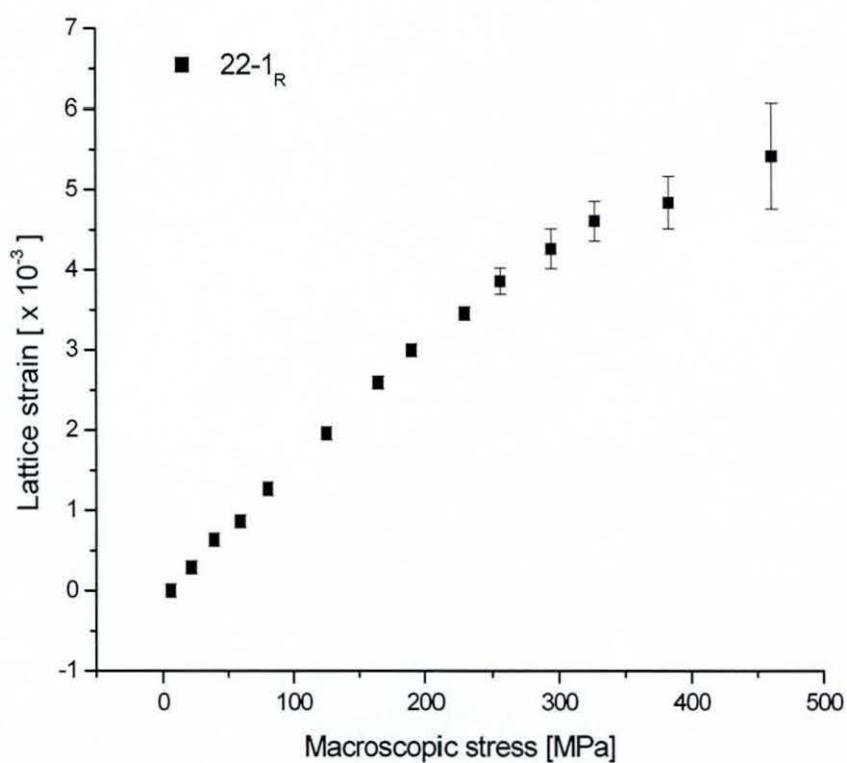
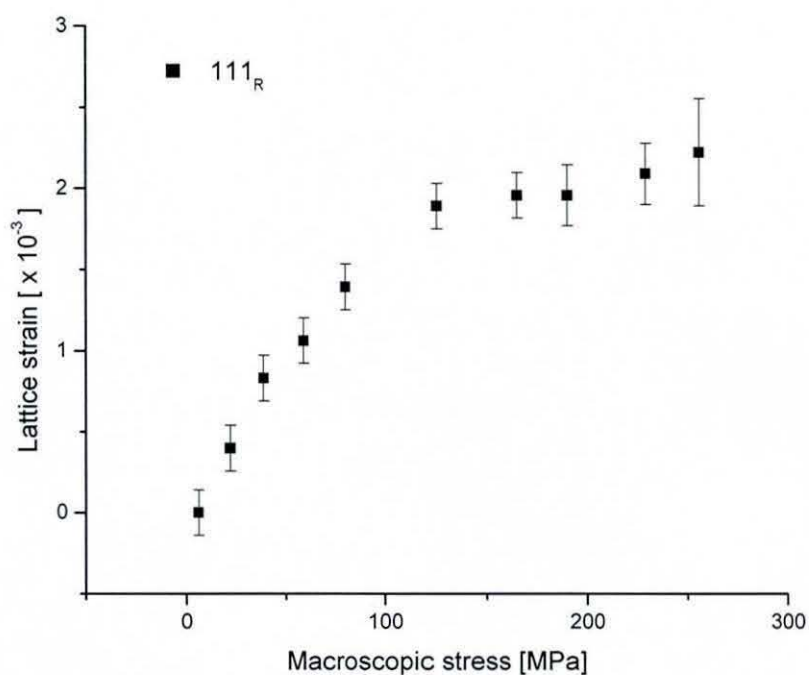


**Figure 4.13a (upper) and 4.13b (lower):** Lattice strain evolution with applied stress for  $(111)_R$  and  $(22-1)_R$  peaks. Stresses and strain are compressive and represented as positive quantities in the figure.

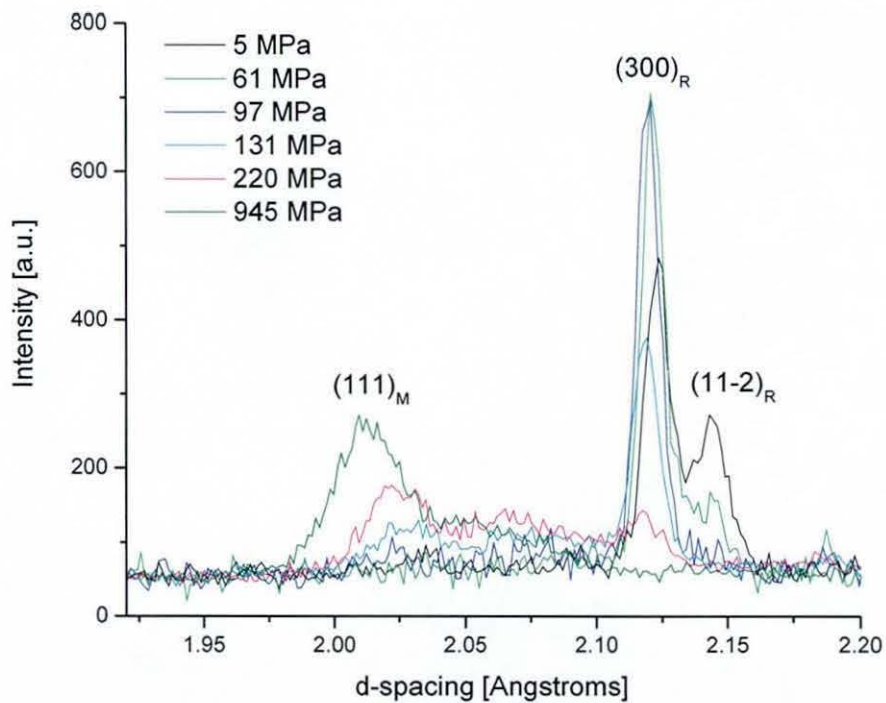
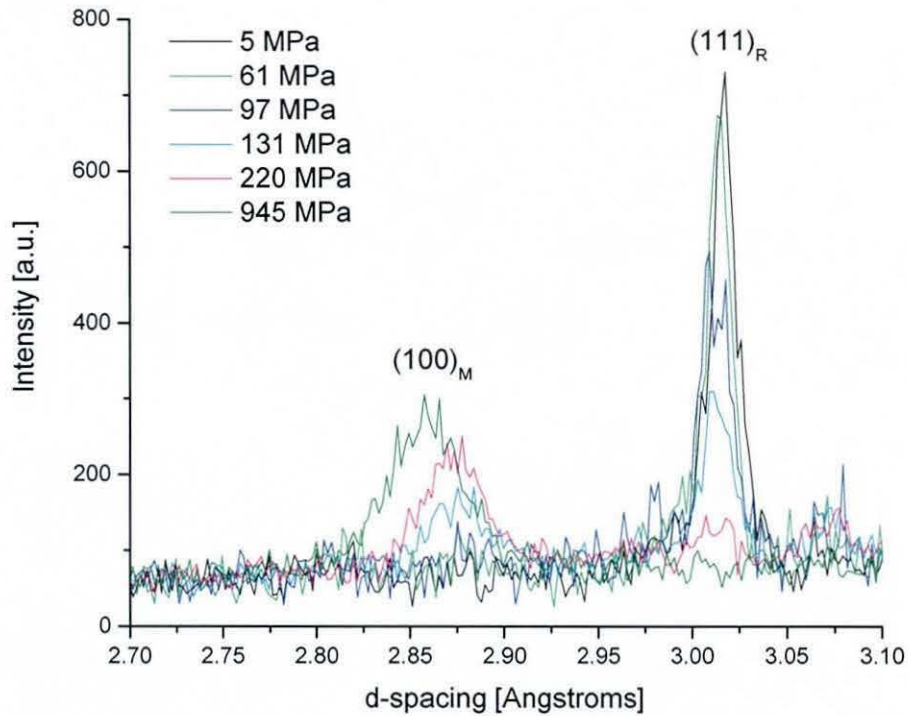
austenite phases. However it may also be due to differences in the load partitioning behaviour due to the differences in deformation mechanisms (R-phase reorientation plus elastic deformation versus purely elastic deformation in the case of austenite) (Sittner et al, 2006).

#### *4.3.3.4 Sample aged at 400 °C for 20 hours*

Diffraction profile evolutions for the main R-phase reflections are shown in Figures 4.14a-c. The details of the intensity evolution is almost identical to that discussed above for the sample aged for 1.5 hours and the reader is referred to the discussion in the previous section for further details of the microstructural changes occurring.

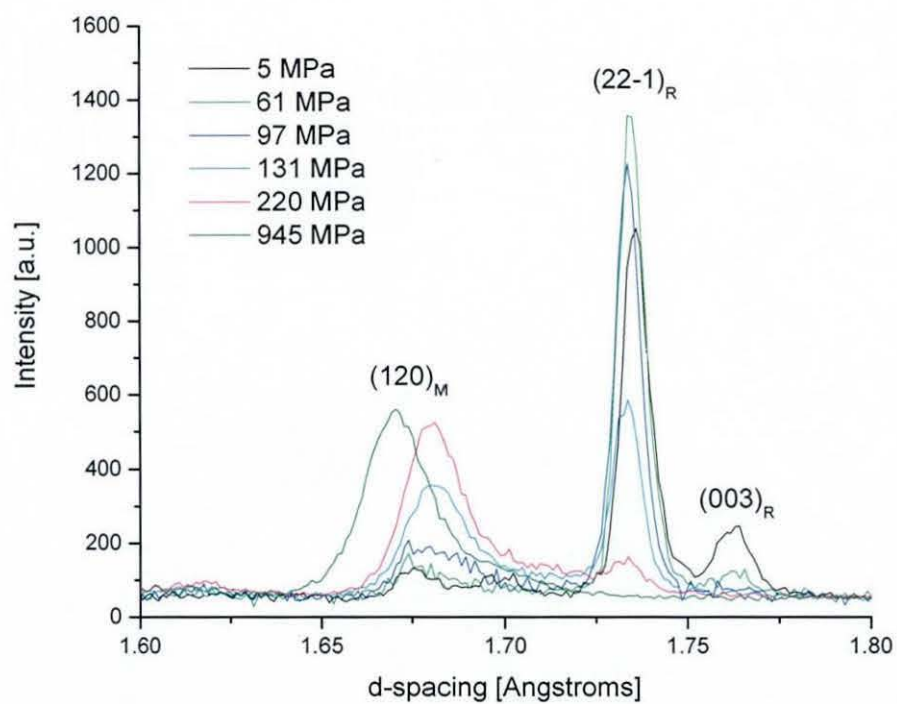
Figure 4.15 shows the evolution of R-phase reflection integrated intensities obtained from the single peak fits. Again twinning is seen to be an active deformation mode from almost the very beginning of the application of stress. Again, the mechanism is similar to that discussed above for the sample aged for 1.5 hours.

Figure 4.16 shows the evolution of the B19' phase volume fraction during deformation. The recorded macroscopic stress-strain curve is included on the figure. The volume fraction of precipitates was estimated as 10 % based on intensity measurements of the  $(111)_R$  R-phase peak. The maximum possible volume fraction of martensite is therefore 0.9, as shown in Figure 4.16. The yield of the material is clearly associated with the formation of the B19' phase.



**Figure 4.14a (upper) and Figure 4.14b (lower):** Diffraction spectra collected during deformation of the NiTi sample subjected to heat treatment of 400 °C for 20 hours. Figure 4.15a shows the d-spacing range around the originally  $(100)_A$  peak and Figure 4.15b shows that around the originally  $(110)_A$  peak.





**Figure 4.14c:** Diffraction spectra collected during deformation of the NiTi sample subjected to heat treatment of 400 °C for 20 hours. The figure shows the d-spacing range around the originally  $(111)_A$  peak.



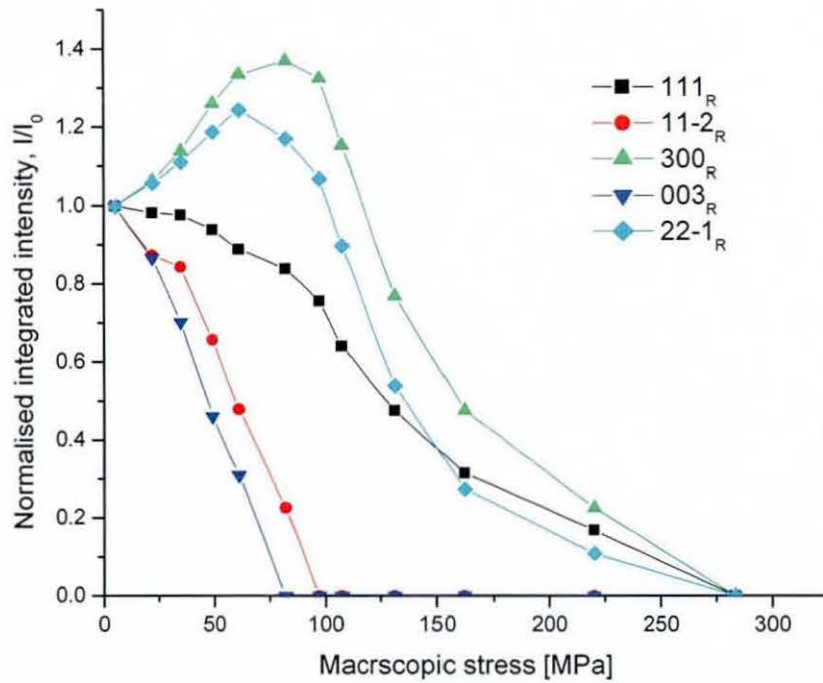


**Figure 4.15:** Integrated intensity evolution for the main R-phase peaks during deformation of the sample aged for 20 hours. Compressive stress is represented as a positive quantity in the figure.

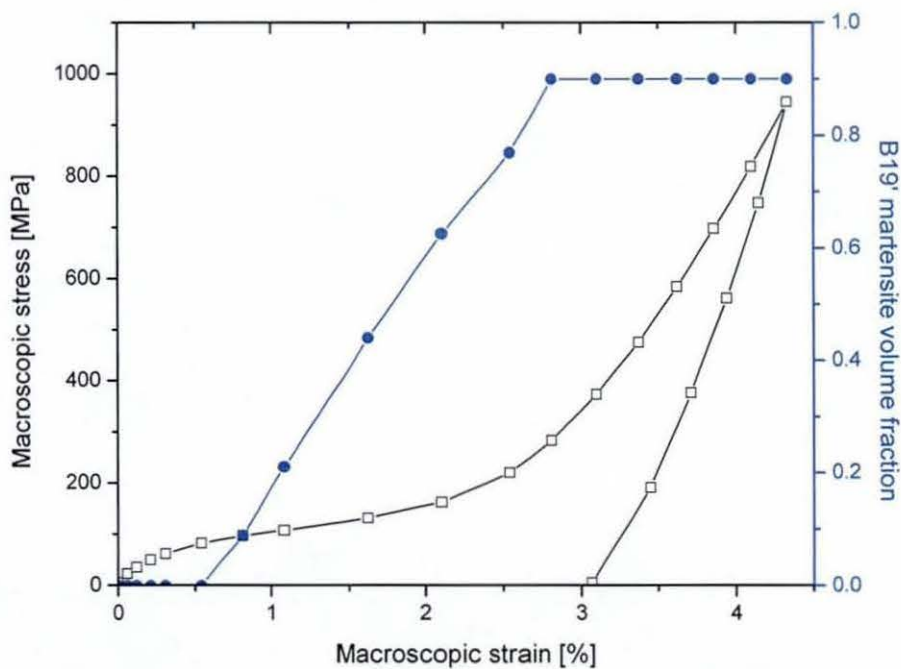


**Figure 4.16:** B19' martensite phase fraction evolution during deformation compared with the recorded macro stress-strain curve. Compressive stresses and strains are represented as positive quantities in the figure.

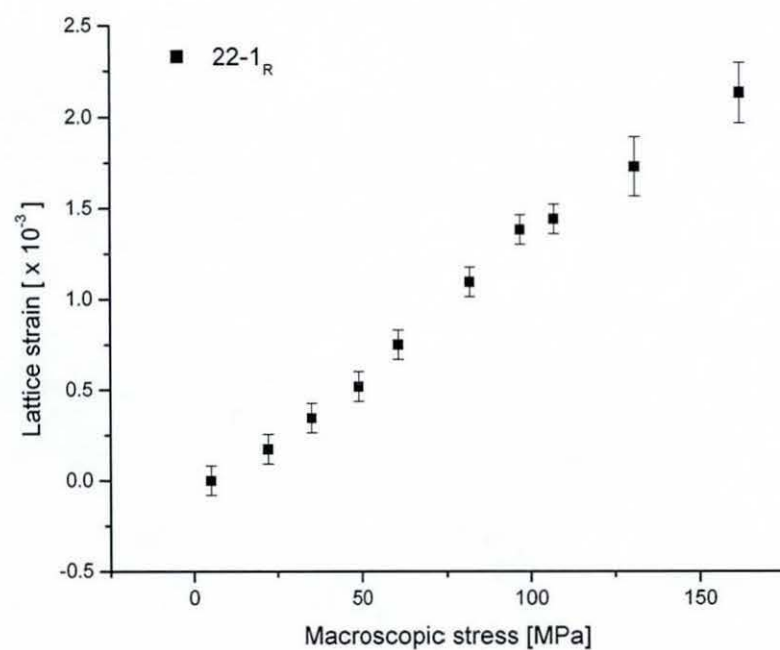
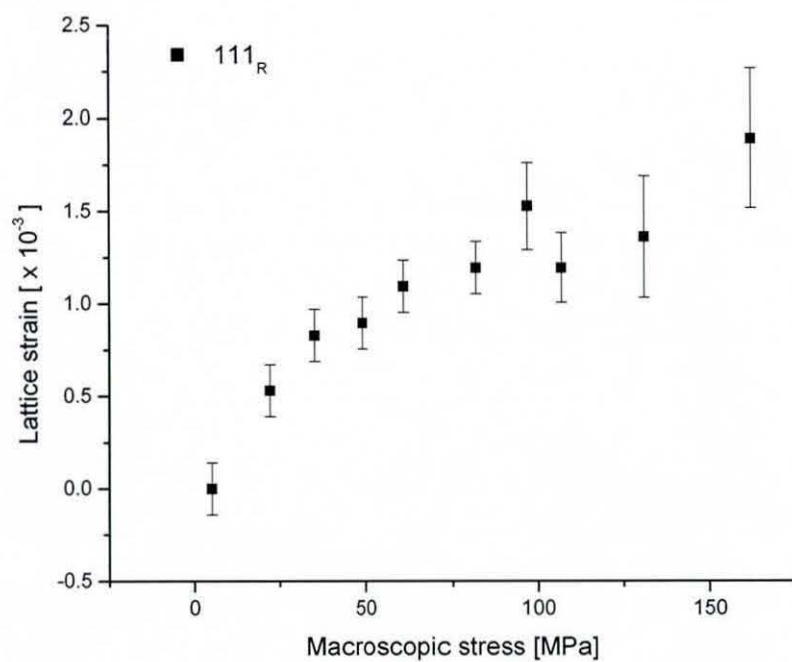


**Figure 4.17a (upper) and 4.17b (lower):** Lattice strain versus applied stress for R-phase reflection in the sample aged for 20 hours. Compressive stresses and strains are represented as positive quantities in the figure.

The lattice strain evolution for fittable R-phase reflection profiles is shown in Figures 4.17a and b. Diffraction elastic constants were again obtained from linear fits to the initial portion of the curves. These were determined as: 35 GPa for the  $111_R$  and 66 GPa for the  $22-1_R$  reflection.

#### **4.4 Conclusions**

Experiments have been conducted on aged samples of solution treated NiTi using both calorimetry and in-situ diffraction combined with mechanical testing.

The following conclusions have been reached:

- Ageing heat treatments has strong effect on mechanical behaviour at RT.
- Different deformation mechanisms are active in the aged samples due to R-phase presence at RT. In aged samples the R-phase has clearly been stabilised by the presence of the  $Ni_4Ti_3$  precipitates.
- There is a difference in measured R-phase rhombohedral angle in samples aged for different lengths of time. This is well known to have a strong effect on the recoverable strains possible due to R-phase reorientation and undoubtedly has an effect on the mechanical behaviour.
- Twinning is active as a deformation mode in R-phase samples from very low stress. This was observed in both aged samples and

indicates that the interfaces formed during austenite to R-phase transition are very glissile under an applied stress.

- Clear growth of R-phase and B19' variants providing maximum strain along the stress axis. In the initial stages of deformation the mechanism is detwinning of the R-phase via variant reorientation,. When this process is exhausted stress induced B19' transformation of the preferential variants begins.
- Yield in stress-strain curves is due to B19' martensite formation in all cases. The differences in yield stress (or more accurately transformation stress) are due to composition changes in the matrix caused by the precipitation process, which lowers the nickel content of the matrix and thus increases the transformation temperatures of the material. The knock-on effect of this is that the critical stress required to induced the B19' martensite is lowered and thus the apparent yield stress of the aged materials is decreased, and decreases further with increased ageing time.

#### 4.5 References

Bataillard, L., Bidaux, J. E., Gotthardt, R., *Philosophical Magazine*, 78(2), (1998), 327.

Callister, W. D., *Materials Science and Engineering*, John Wiley & Sons Inc., (2003), 174-191.

Dautovich, D. P., Purdy, G. R., *Can. Metall. Q.*, 4, (1965), 129.

Fan, G., Chen, W., Yang, S., Zhu, J., Ren, X., Otsuka, K., *Acta Materialia*, 52 (2004), 4351.

Fukada, T., Saburi, T., Doi, K., Nenno, S., *Mater. Trans. JIM*, 33, (1992), 271.

Gall, K., Sehitoglu, H., Chumlyakov, Y. I., Kireeva, I. V., *Acta Materialia*, 47(4), (1999a), 1203-1217.

Gall, K., Sehitoglu, H., Chumlyakov, Y. I., Kireeva, I. V., and Maier, H. J., *Journal of Engineering Materials and Technology*, 121, (1999b), 19-27.

Goryczka, T., Morawiec, H., *Journal of Alloys and Compounds*, 367, (2004), 137.

Higgins, R. A., *Properties of Engineering Materials*, 2<sup>nd</sup> edition, Butterworth-Heinemann, (2001), 73.

Jorgensen, J. D., Johnson, D. H., Mueller, M. H., Worlton, J. G., Von Dreele, R. B., *Proc. Conference on Diffraction Profile Analysis*, Krakow, 14-15 August, (1978), 20-22.

Khalil-Allafi, J., Ren, X., and Eggeler, G., *Acta Materialia*, 50, (2002a), 793-803.

Khalil-Allafi, J., Dlouhy, A., Eggeler, *Acta Materialia*, 50, (2002b), 4255-4274.

Khalil-Allafi, J., Eggeler, G., Dlouhy, A., Schmahl, W. W., Somsen, Ch., *Materials Science and Engineering A*, 378, (2004), 148-151.



- Kraus, W., Nolze, G., *Powdercell for Windows* (version 2.4), (2000).
- Larson, A. C., Von Dreele, R. B. Von Dreele, *General Structure Analysis System (GSAS)*, Los Alamos National Laboratory Report LAUR 86-748 (2002).
- Ling, H. C., Kaplow, R., *Metallurgical Transactions A*, 11, (1981), 77.
- Lukas, P., Sittner, P., Neov, D., Novak, V., Lugovyy, D., and Tovar, M., *Materials Science Forum*, 404-7, (2002), 835-840.
- Massalski, T. B., Okamoto, H., Subramanian, P. R., Kacprzak, L. (Eds.), *Binary Alloy Phase Diagrams*, 2<sup>nd</sup> edition, 3, Materials Park, OH: ASM International, (1990), 2874.
- Melton, K. N., Ni-Ti Based Shape Memory Alloys, in T. W. Duerig, K. N. Melton, D. Stockel and C. M. Wayman (Eds.), *Engineering Aspects of Shape Memory Alloys*, Butterworth-Heinemann, (1990), 21-35.
- Miyazaki, S., Otsuka, K., *Metallurgical Transactions A*, 17, (1986), 53.
- Miyazaki, S., Kimura, S., Otsuka, K., *Philosophical Magazine A*, 57, (1988), 467.
- Morawiec, H., Ilczuk, J., Stroz, D., Goryczka, T., Chrobak, D., *Journal de Physique IV*, (1997), C5-155.
- Nam, T. H., Saburi, T., Kawamura, Y., Shimizu, K., *Mater. Trans. JIM*, 31, (1990), 262.

Otsuka, K., Introduction to the R-phase Transition, in T. W. Duerig, K. N. Melton, D. Stockel and C. M. Wayman (Eds.), *Engineering Aspects of Shape Memory Alloys*, Butterworth-Heinemann, (1990), 36-45.

Otsuka, K., Ren. X., *Progress in Materials Science*, 50, (2005), 511.

Saburi, T., Tatsumi, T., and Nenno, S., *Journal de Physique*, 43, (1982), C4-261.

Saburi, T., Nenno, S., Nishimoto, Y., Zeniya, M., *Journal of the Iron and Steel Institute of Japan*, 72, (1986), 571.

Saburi, T., Ti-Ni shape memory alloys, in K. Otsuka and C. M. Wayman (Eds.), *Shape Memory Materials*, Cambridge University Press, (1998), 49-96.

Sittner, P., Lukas, P., Daymond, M. R., Novak, V., Swallowe, G. M., *Materials Science and Engineering A*, 324, (2002), 225-234.

Sittner, P., Landa, M., Lukas, P., and Novak, V., *Mechanics of Materials*, 38(5-6), (2006), 475-492.

Vaidyanathan, R., Bourke, M. A. M., Dunand, D. C., *Journal of Applied Physics*, 86(6), (1999), 3020-3029.

Von Dreele, R. B., Jorgensen, J. D., Windsor, C. G., *Journal of Applied Crystallography*, 15, (1982), 581-589.

Wang, F. E., Buehler, W. J., Pickart, S. J., *Journal of Applied Physics*, 36, (1965), 3232.

Warren, B. E., and Averbach, B. L., *Journal of Applied Physics*, 21, (1950), 595-599.



## **Chapter 5:**

# **Deformation twinning in NiTi under tensile and compressive stress**

### **5.1 Introduction**

#### *5.1.1 Stress-free twins in B19' martensite*

Under stress free cooling such that, in solution heat treated NiTi, the austenite B2 phase transforms to B19' martensite, a characteristic microstructure of variants of different fractions is formed. This known as self-accommodation and minimises the strain energy developed during austenite to martensite transformation.

Due to the phenomenological theory of martensitic transformations (PTMT) discussed in chapter 1, when martensite forms in the presence of austenite, twinning is required to be the lattice invariant shear. For NiTi, much research effort had been expended on determining the twinning system in this alloy formed under stress free cooling, particularly via use of electron microscopy. In a recent review (Otsuka and Ren, 2005) have discussed the results of previous investigations. The twinning systems determined are summarised as follows:

- Otsuka and co-workers found  $\{-1-11\}$  type I twins and stacking faults on the basal plane (Otsuka et al, 1971).

- Gupta and Johnson discovered both (001) compound twins and {011} type I twins (Gupta and Johnson, 1973). They also confirmed the {-1-11} twins observed by Otsuka et al, detailed above.
- Knowles and Smith found <011> type II twins (Knowles and Smith, 1981).
- Onda and co-workers determined (100) compound twins, which are conjugate to (001) twins (Onda et al, 1992).

Thus a multitude of twinning systems has been found in NiTi which is expected due to the low symmetry (monoclinic) nature of the B19' martensite crystal structure. In a typical stress-free cooled polycrystal many different types of twins may exist, however it is the general consensus that the <011> type II twins discovered by Smith and Knowles are predominant (Otsuka and Ren, 2005). However, the presence of some of the twinning modes are not compatible with solutions via the PTMT and their appearance can probably be explained as deformation twins. The (100) compound twins discovered by Onda et al fall into this category.

#### *5.1.2 Mechanical behaviour of twinned B19' martensite*

Many aspects of the mechanical properties of NiTi are related to the twinning/detwinning process, such as the shape memory effect and the damping capacity (Liu, 2001). A understanding of the deformation processes and evolution of texture on the granular scale in a polycrystal is thus very important in optimising the functional properties.

Detwinning should take place without significant dislocation generation if the deformation is to be reversible upon heating (the shape memory effect). Texture has a strong effect on the mechanical behaviour due to its strong effect on the detwinning properties.

The deformation of thermally induced martensite, with the characteristic self-accommodated variant microstructure discussed above, is generally associated with the reorientation of variants by the movement of the interfaces formed due to twinning. The yield stress of the material in this state is always seen to be less than the yield of NiTi deformed while in the austenite state. This leads many to term the martensitic phase soft, while the austenite is hard in comparison.

Under the action of a tensile stress, martensitic NiTi is seen to deform in a Luders-like manner at a constant stress of circa 100 MPa. This plateau proceeds until a macroscopic strain of around 6 % before the stress-strain curve deflects upwards (Liu et al, 2000). The yield stress of the material is assumed as the stress required to begin the detwinning process. The detwinning process in tension does not appear to occur homogeneously and is observed to propagate into the centre of the sample from the area around the grips.

Under compression, the macroscopic behaviour is quite different. Figure 5.1 shows a schematic diagram comparing the response under tensile and compressive stress.

The current understanding of the deformation mechanisms active during compressive deformation is that after an initial elastic region the material deforms via dislocation motion with the detwinning of variants playing an

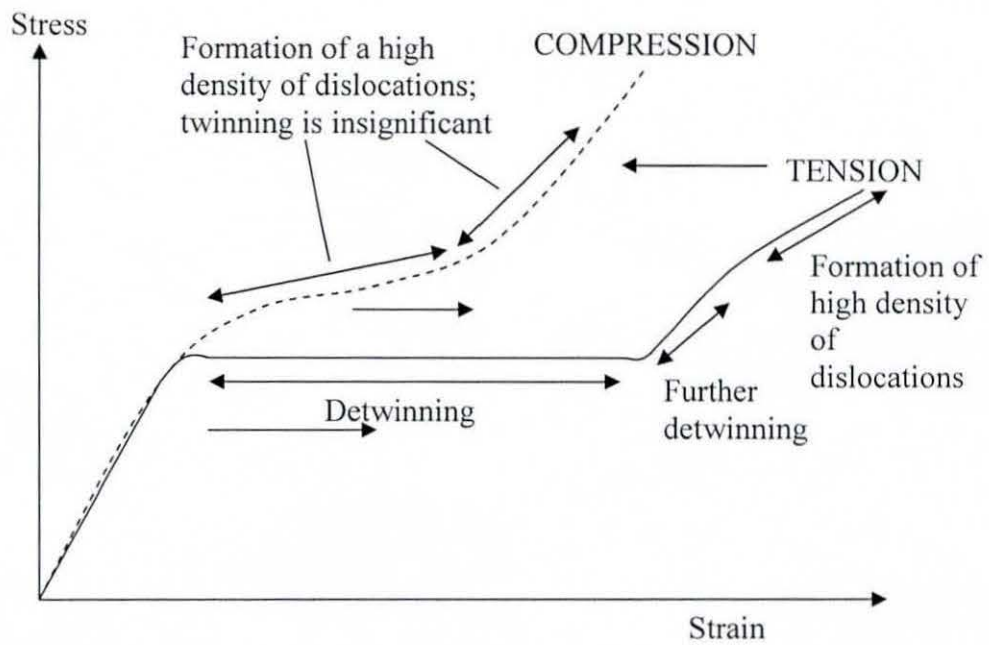


**Figure 5.1:** Current understanding, based on TEM studies, of the deformation mechanisms in the detwinning of martensitic NiTi under compressive and tensile deformation. Diagram after Liu, 2001.



insignificant role. Liu and co-workers investigated the microstructure formed in NiTi after compressive deformation to 4 % strain via electron microscopy and found a high value for dislocation density without evidence of large-scale detwinning taking place (Liu et al, 1998).

Thus in summary, there is a clear asymmetry in the stress-strain curves of martensitic NiTi under the action of a tensile and compressive stress. In the tensile case deformation occurs via detwinning and in the compressive case it occurs by dislocation generation and detwinning can be neglected. This represents the current understanding of the deformation processes in martensitic NiTi.

### *5.1.3 Objectives of present work*

There can be problems with the very thin samples used in the type of TEM study mentioned in the previous section: transformation behaviour may be unrepresentative of that observed in tests on bulk samples. In order to see a true picture of the deformation processes in the bulk of the material a technique able to resolve microstructural details at depth is required. The neutron diffraction technique is capable of this and allows variant fractions and internal strains evolving during deformation to be quantified. The emphasis is on determining the twinning activity taking place via the intensity changes of peaks (which are proportional to the volume fraction of certain variants).

Thus the focus of the experiments described in this chapter is to examine the deformation mechanisms active during tensile and compressive deformation of martensitic NiTi using the in-situ neutron diffraction technique. In order

to aid this study, offline pole figure measurements have been made on a sample subjected to various compressive strains. These measurements have been made using the Residual Stress and Texture (REST) diffractometer at the Neutron Research Laboratory (NFL) in Studsvik, Sweden.

## **5.2 Experimental details**

### *5.2.1 Material*

The material was Ni-Ti rod obtained from Memory Metalle, Germany, with a nominal composition of Ni-49.8Ti (at.%) (manufacturer's notation: NiTi-M) – the same material as that used for the stress-induced martensitic transformation study described in chapter 3.

Two samples were machined from the as-received material: a cylindrical sample suitable for compression testing, with a length of 27 mm and diameter of 10 mm, and a dumbbell-shaped compression sample suitable for use with the Hounsfield grips on the ENGIN-X Instron loading rig, of approximate diameter of 8 mm.

The samples were subjected to a heat treatment of 600 °C for 1 hour followed by immediate quenching into room-temperature water. The transformation temperatures of the material were subsequently measured using differential scanning calorimetry (DSC) and were found to be:  $M_s = 30$  °C,  $M_f = 6$  °C,  $A_s = 52$  °C,  $A_f = 74$  °C. The DSC thermogram is shown in Figure 5.1.

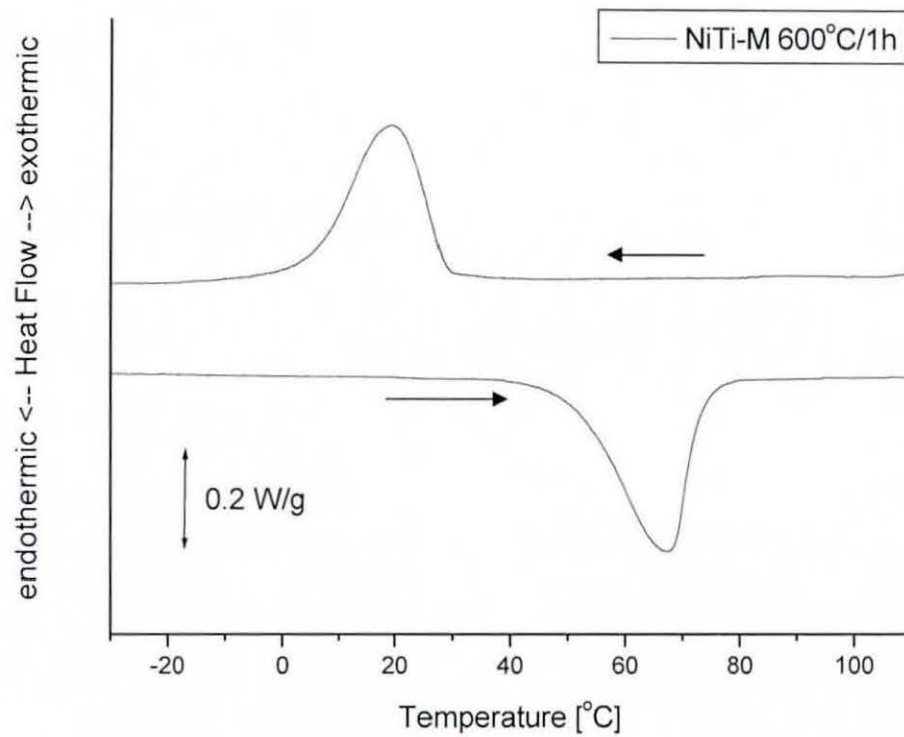


**Figure 5.2:** DSC thermogram of the NiTi sample used in the tension and compression tests. Tests were conducted at room temperature (20 °C). Samples were immersed in liquid nitrogen prior to test in order to ensure a fully martensitic microstructure. A heating rate of 10 K/min was used.

The sample used in the texture measurements was a cylindrical compression sample of near-equiatomic NiTi, which is martensitic at room temperature, was obtained from Dr. P. Sittner of the Institute of Physics, Academy of Sciences of the Czech Republic. The sample was a commercial thick wire (diameter = 5mm) formed by cold-drawing. The sample thus has the same texture (strong  $\langle 111 \rangle$  austenite fibre texture) as that of the samples obtained via Memory Metalle.

### *5.2.2 In-situ diffraction experiments*

The ENGIN-X instrument at ISIS, discussed in chapter 2, was used for the in-situ diffraction experiments. Separate test were conducted with the Memory Metalle samples deformed in both tension and compression. Sample strain was measured using a clip-on extensometer. Prior to testing, samples were immersed in liquid nitrogen and allowed to heat up to room temperature, ensuring a fully martensitic structure at room temperature. Both tests were conducted at room temperature. Diffraction spectra were collected by axial and radial detectors during halts in the loading of about 40 minutes duration. Diffraction peaks were fitted with the profile function of Jorgensen et al discussed within chapter 2, from which the integrated intensity and peak position were extracted. The incident beam slits for both experiments had an approximate vertical height of 5 mm and width of 4 mm used with 4 mm exit collimators, illuminating only the central region of the samples.

The measurements in which the diffracting plane normals coincide with the direction of the applied stress are denoted axial and those in which the



diffracting plane normal is perpendicular to the applied stress are denoted radial.

### *5.2.3 REST diffractometer*

In the texture measurements made on REST several martensite reflections were monitored in the undeformed sample and after deformation to -2 and -4 % strain.

The REST diffractometer is a constant wavelength, high-resolution diffractometer (steady-state reactor neutron source) operating with neutrons of approximately 1.7 Angstroms via a Si (331) monochromator. The experimental set-up is identical to that shown for a typical constant-wavelength diffractometer in Figure 2.2 in chapter 2. The texture measurements involved the sample being mounted in the centre of a two-circle Eulerian cradle allowing the orientation of the sample at all possible angles. Samples were deformed off-line to the prescribed strain and then unloaded. Subsequently they were mounted in the goniometer and measurements made. Due to the length of time required to collect a sufficient diffraction signal, only a quarter of the Eulerian space was sampled. However, due to the cylindrical symmetry of sample, characteristic on the cold-drawing fabrication process, these quarter pole figures could be mapped into the other quadrants to create full-pole figures. Pole figures were obtained for the following martensite reflections: the (011), (100), (002) and (120).

## **5.3 Results and discussion**

### *5.3.1 Macroscopic stress-strain response*

The macroscopic stress-strain curves obtained during tensile and compressive loading are shown in Figure 5.3. The asymmetry in deformation characteristics between both loading modes can be clearly observed. Both curves display the classical features seen in other studies of the tension-compression asymmetry in NiTi and shown in the schematic diagram in Figure 5.1. These are, for the tensile stress-strain curve, the initially elastic phase followed by yield, and then a plateau until about 6 % strain before the curve deflects upwards indicative of Luders-type deformation. For the compressions curve no clear plateau is observed. A much higher amount of stress is required to generate the same strain in compression and in tension. Both tests show the yield stress to be roughly the same regardless of the sense of the applied load. Yield occurs at approximately 100 MPa in both tension and compression.

### *5.3.2 Intensity evolution*

A full diffraction spectrum collected over a d-spacing range of about 1 to 3.2 Angstroms prior to deformation is shown in Figure 5.4. Included for comparison are spectra collected under the peak stresses achieved in the tension and compression tests in Figures 5.5 and 5.6 respectively. The detwinning is clearly evident for both compression and tension tests via the texture changes that have clearly occurred in both samples. Single peak fitting of the reflections indexed in Figure 5.4 was undertaken for both tests. Integrated intensity values for each reflection at the points marked on the stress-strain curves in Figure 5.3 were extracted from these fits. The evolution of the integrated intensity as a function of the macroscopic strain

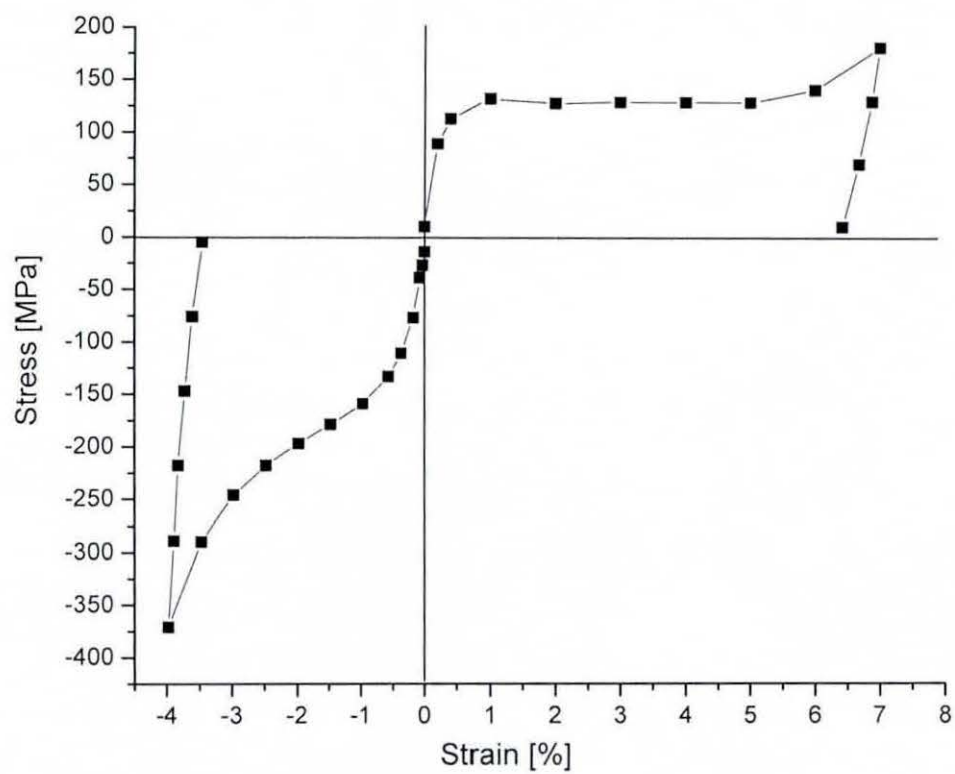


**Figure 5.3:** Tensile and compressive stress-strain curves for martensitic NiTi deformed at room temperature. The solid squares indicate the points at which neutron diffraction spectra were acquired.

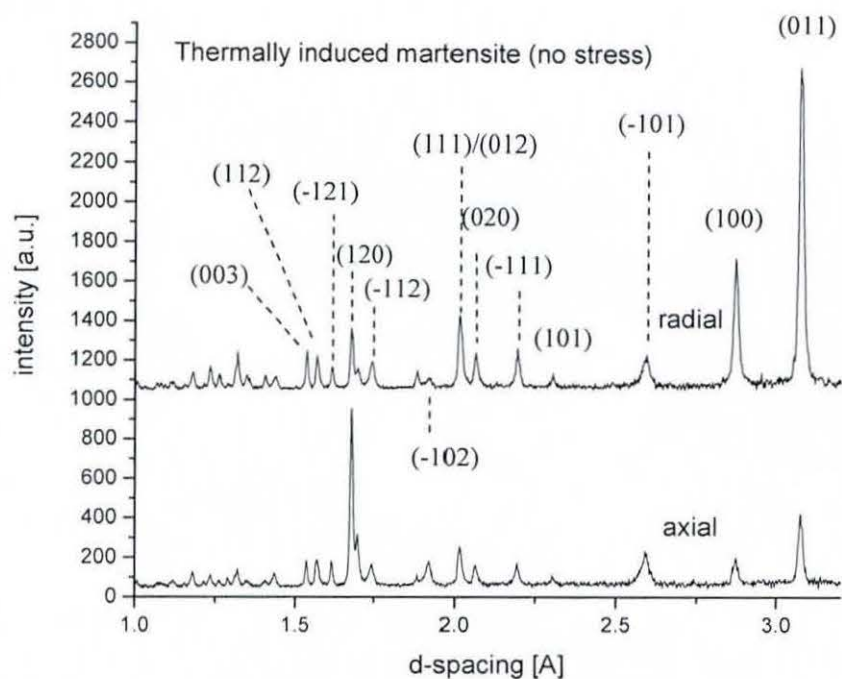


**Figure 5.4:** Diffraction spectra corresponding to thermally-induced martensite, i.e. the spectra recorded at 0 % strain.

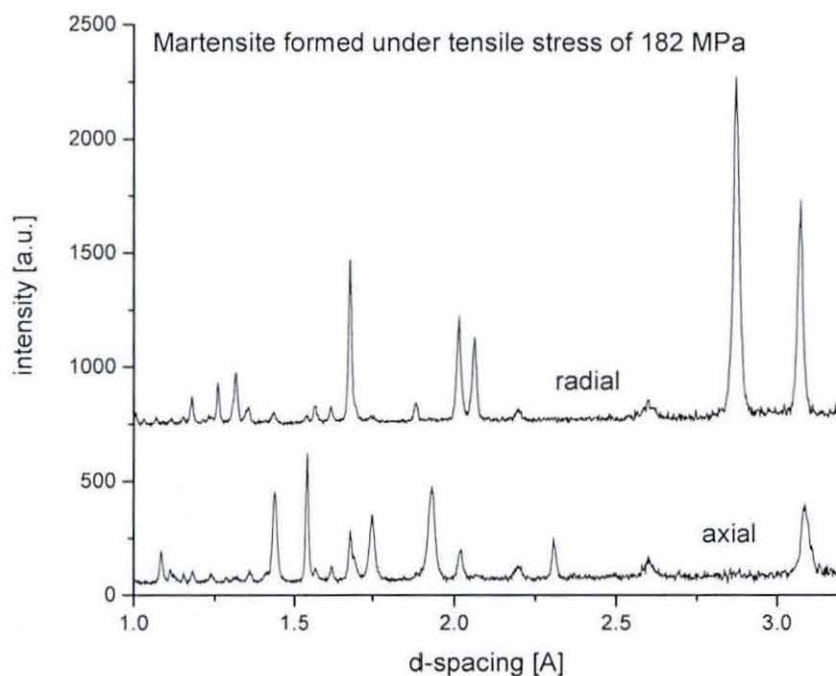


**Figure 5.5:** Diffraction spectra recorded under peak stress of 182 MPa during the tensile deformation. See Figure 5.4 for reflection indices.

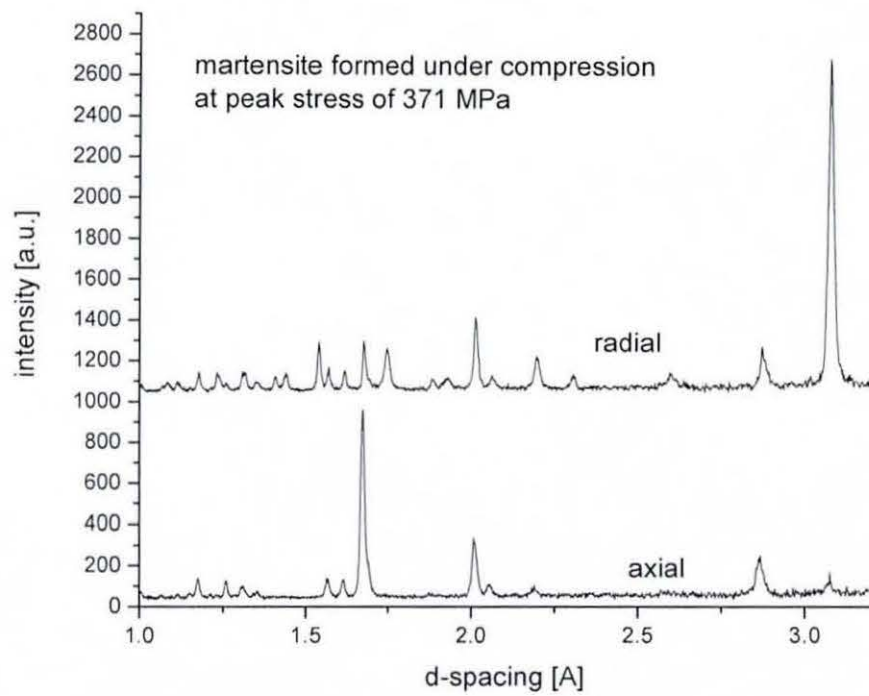


**Figure 5.6:** Diffraction spectra recorded under peak stress of 371 MPa during the compressive deformation. See Figure 5.4 for reflection indices.



is shown in Figure 5.7. The intensity data shown in Figure 5.7 was obtained from the axial detector and thus represents those reflections with lattice plane normals aligned with the bar axis.

The evidence of twinning occurring both during tensile and compressive deformation is clear from the intensity changes visible for most reflections. Dislocation formation gives rise to a broadening of the diffraction profiles, rather than large intensity changes and therefore these changes cannot be due to conventional plastic flow. There is, however, the possibility that plasticity-induced texture changes could be the cause of the integrated intensity increases/decreases, although the changes evident here seem to be too large for this to be the case and therefore they must be exclusively ascribed to detwinning of the B19' martensite.

In tension, the interpretation of the intensity changes is complicated by the fact that the material deformation occurs inhomogeneously initially. It is only when the deformation proceeds beyond the plateau region of the stress-strain curve that the sample begins to deform homogeneously. It is therefore difficult to say whether the intensity changes in the tensile case are representative of the changes in variant microstructure occurring in the bulk of the sample. However, the intensities at the peak stress of 182 MPa (strain = 7 %) are valid as bulk measurements. These clearly indicate the changes in intensity associated with the detwinning process. It is again observed that those variants which maximise the strain in the direction of the applied stress grow preferentially. It can be seen that those martensitic variants residing in the originally (100) austenite grains, i.e. those variants corresponding to the (011) and (100) martensite peaks, begin to detwin first and the variants within these grains are fully detwinned by the end of the

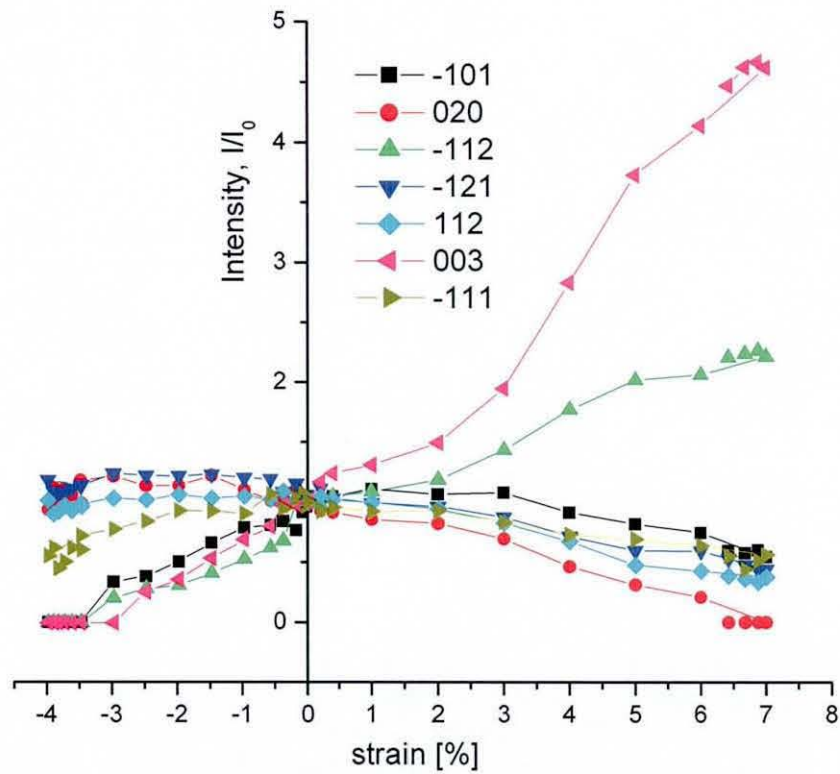
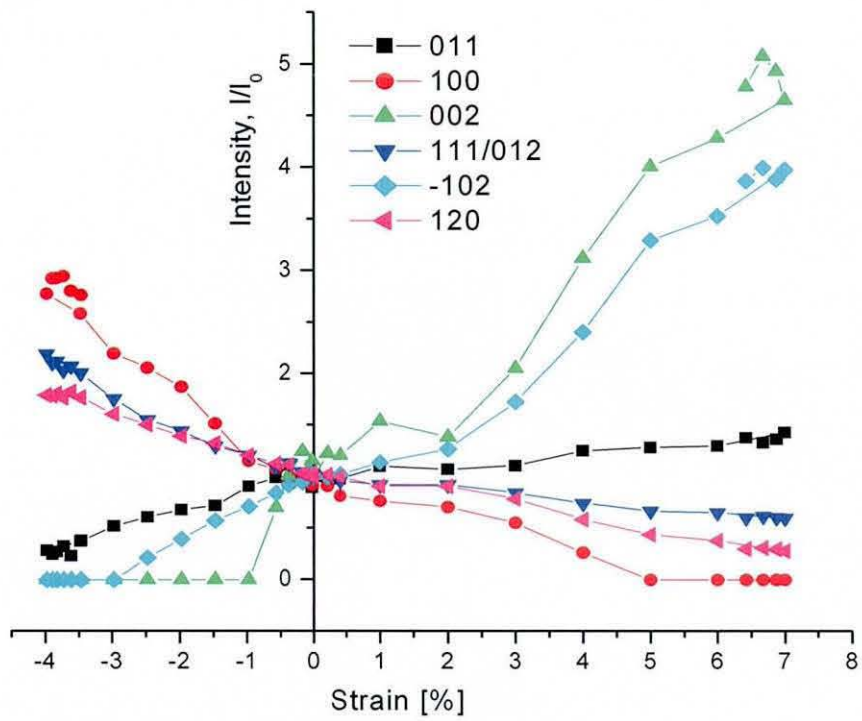


**Figure 5.7:** Integrated intensity evolution for martensite peaks during tensile/compressive deformation as a function of the generated macroscopic strain. Intensity data from axial detector.

test. These variants are therefore preferentially oriented for detwinning during tensile deformation of the NiTi polycrystal in the martensitic state.

Variants within other grain orientations still remain twinned to a certain extent and this indicates that further detwinning – and thus further generation of recoverable strain – is possible. Further detwinning is expected to take place at a higher stress than the 182 MPa reached here. Although full detwinning has not taken place, it is clear that those variants which maximise the tensile strain generated grow preferentially. These are the (011), (002) and the (-102) peaks which indicate the formation of LCVs associated with tensile strain generation of 1.73 %, 7.7 % and 9.7 % via full reorientation of variants in the (100), (110) and (111) austenite grains respectively.

Those grains which decrease in intensity are associated with the growth of variants favoured by a compressive stress. Examining Figure 5.7 it is generally observed that peaks which grow more intense in tension decrease in intensity during compression and vice versa. However, the (-111) notably does not – it is seen to decrease in intensity both in tension and in compression. The variants corresponding to this peak are associated with the generation of a small amount of tensile strain in the originally (110)<sub>A</sub>-oriented austenite grains. The simple case of full detwinning to form a single variant of martensite is therefore not generally seen. Most likely all of the twinning is not due solely to reorientation of the assumed <011> type II twins in the self-accommodated microstructure. There may well be deformation twins formed during mechanical tests.

Under compression, detwinning is evident by the changes in diffracted intensity for many peaks. This appears to contradict the earlier TEM work



on samples deformed in compression, which indicated that detwinning was a negligible process and that the main deformation mechanism was dislocation motion. Since the processes involved in creating the thin sheets required for use with TEM microscopes can have a strong effect on the microstructure and leave it unrepresentative of the bulk, the diffraction measurements here, which are made on unprocessed bulk samples, must be treated as providing the true picture of the deformation mechanism. This is clearly detwinning. As with the tensile deformation, it is clearly those variants which maximise the strain in the direction of the applied compressive stress that are seen to grow at the expense of more unfavourable ones, i.e. those associated with growth in the tensile test. Peaks which show a large growth in intensity include the  $(100)_M$ ,  $(002)_M$  and  $(120)_M$  which correspond to the growth of variants which yield compressive strains of -5.1 %, -5.6% and -3.9 % respectively when fully detwinned. These represent the variants which offer the maximum compressive strain generation in the (100), (110) and (111) austenite grains.

However, unlike the tensile deformation, in the compressive case not all peaks are seen to change in intensity. For example, the (112), (-121) and (020) exhibit very little change in intensity throughout the deformation. Most likely the variants corresponding to these peaks will be deforming plastically. Also, since the detwinning process has been exhausted in some grains, i.e. the originally (100) austenite grains, the recoverable strain generated is likely to be limited by plastic deformation of the fully detwinned variants, which is the only further deformation mode available after full detwinning and elasticity have been exhausted.

From examination of Figure 5.7 it appears that the intensity changes seems to stabilise at a macroscopic compressive strain of around 3.5 %. This

coincides with an inflection in the compressive stress-strain curve (Figure 5.3) and appears to indicate that the detwinning/reorientation process ends, or at least subsides, at this point. The deformation must presumably continue by the generation of dislocations beyond  $-3.5\%$  macroscopic strain.

Thus in compression, the deformation is not realised exclusively through detwinning – some plastic deformation does seem to take place. However plastic deformation does not appear to be the dominant deformation mechanism in bulk NiTi deformed in compression, as suggested by the earlier TEM work. It appears, from the intensity changes presented here, to be twinning.

### *5.3.3 Pole figures*

The pole figures obtained from texture measurements are shown in Figure 5.8; these correspond to the martensite 011, 100, 002 and 120 reflections. Pole figure measurements were made on four strong reflections which did not overlap with any others. These measurements were made after compressive deformation corresponding to  $-2\%$  and  $-4\%$  strain, with measurements made at  $0\%$  prior to this in order that a meaningful comparison could be made. The measurements were made on a sample of similar texture (i.e strong  $\langle 111 \rangle_A$  fibre texture) but from a different manufacturer. Thus the comparison with the in-situ measurements will indicate whether the twinning indicated by the above in-situ measurements during compression are valid for all wire/rod samples. The pole figures in Figure 5.8 are essentially contour maps which display the diffracted intensity as a function sample orientation. The centre of the pole figure corresponding to the diffracted intensity from axial detector in the in-situ

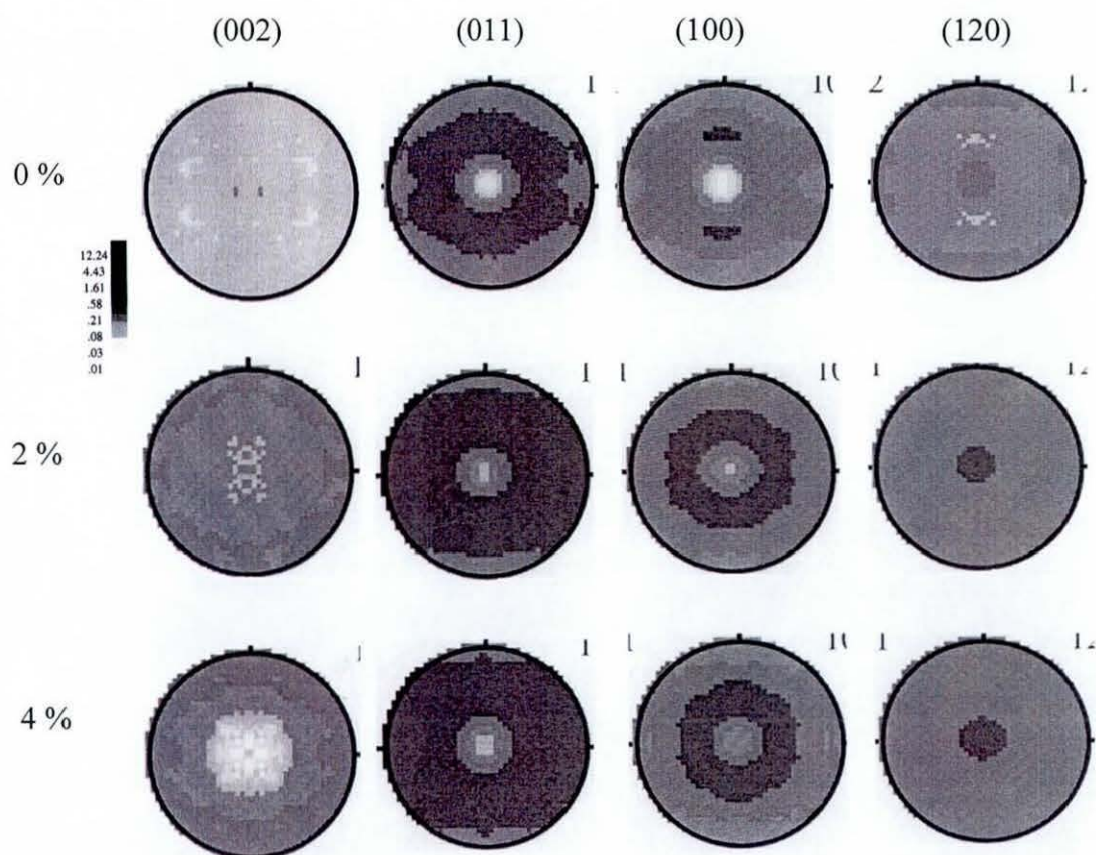


**Figure 5.8:** Pole figures collected using the REST diffractometer. The quantity on the left is the compressive deformation before pole figure measurement. Reflection indices are indicated in the upper part of the figure. Darker shade of grey indicates stronger intensity. The centre of the pole figures is equivalent to the axial measurements of intensity obtained on ENGIN-X.



experiments. For example, in the pole figure for the (100) martensite peak it can be seen in the centre of the pole figure that the intensity increases with each increment in strain. This indicates the growth of these variants in the  $\langle 100 \rangle_A$  oriented grains, in good agreement with the in-situ data.

It is clear from examination of the pole figures that large changes in the diffracted intensity for all peaks have taken place as a result of the compressive deformation. The intensity changes also correspond very well with those obtained during the in-situ deformation experiment. This confirms the earlier interpretation that twinning is the dominant deformation mechanism in the compressive deformation of martensitic NiTi.

#### *5.3.4 Lattice strain evolution*

The lattice strain response for various strong reflections is shown in Figure 5.9 and 5.10, obtained during the in-situ diffraction experiment on the compressive. Only lattice strains for the compression test are shown due to the localised deformation mode which occurs in tension complicating the lattice strain analysis. All of the peaks shown in Figure 5.9 and 5.10 show some linearity with the applied stress, at least initially. From this linearity the gradient may be measured and thus the diffraction elastic constants obtained. The following values are obtained:  $E_{100} = 72$  GPa,  $E_{011} = 119$  GPa,  $E_{111/012} = 125$  GPa and  $E_{120} = 134$  GPa.

The single crystal elastic constants for the B19' martensite phase are unknown at present, due to problems with growing the suitably-oriented martensitic single crystals. Thus in much of the previous modelling work on NiTi, modulus values have to be assumed to be much less than the austenite

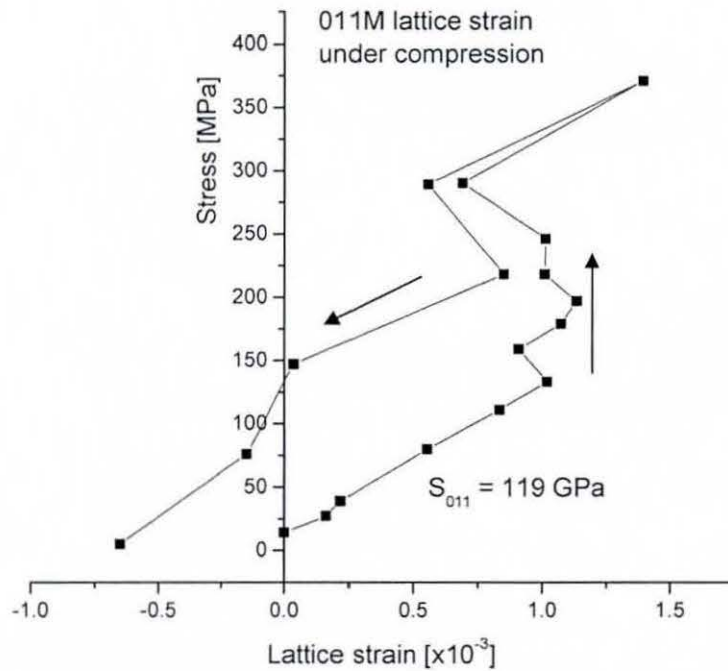
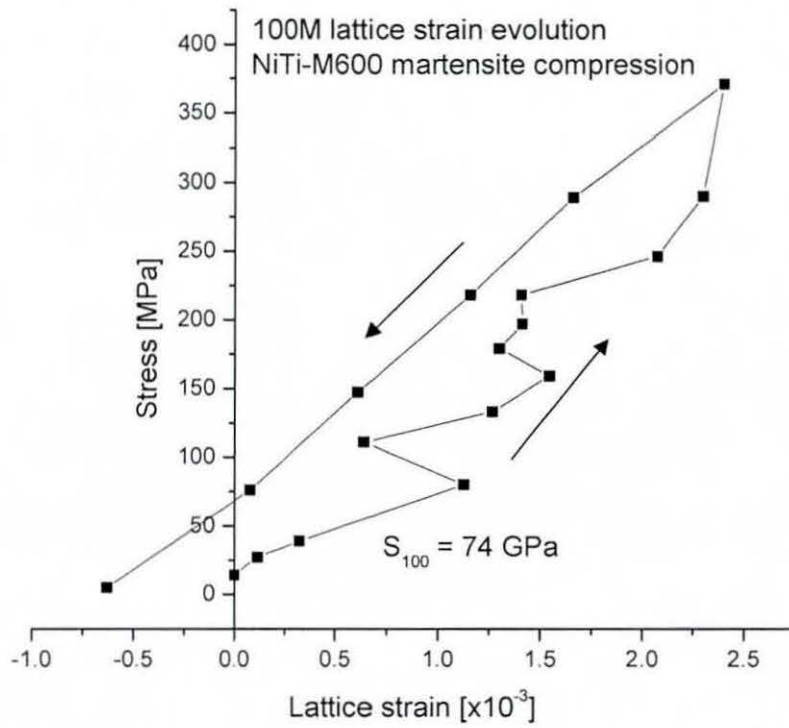


**Figure 5.9a (upper) and Figure 5.9b (lower):** Lattice strain evolution with applied stress of the (100) and (011) martensite peaks during the compression test. DEC's measured from linear portions of the curves. Compressive stresses and strains are represented as positive quantities in the figure.

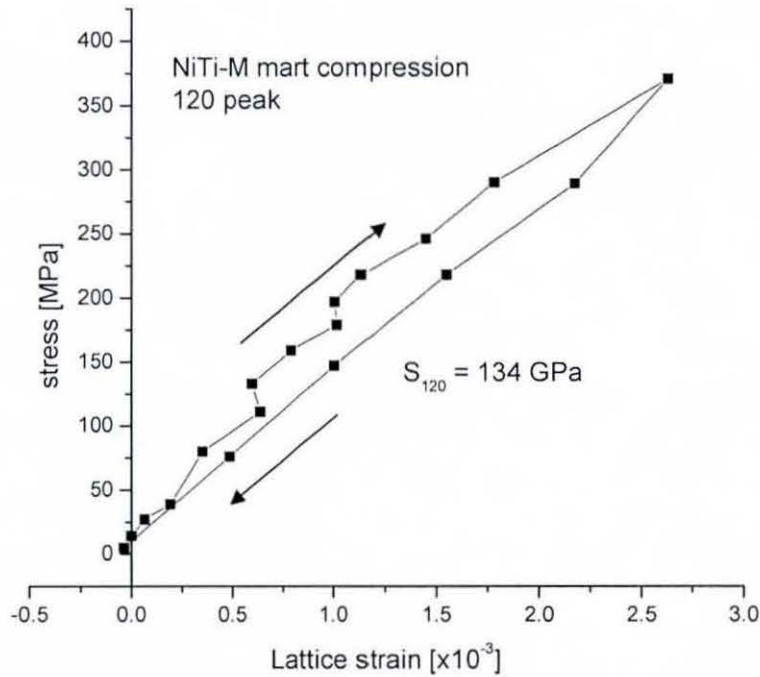
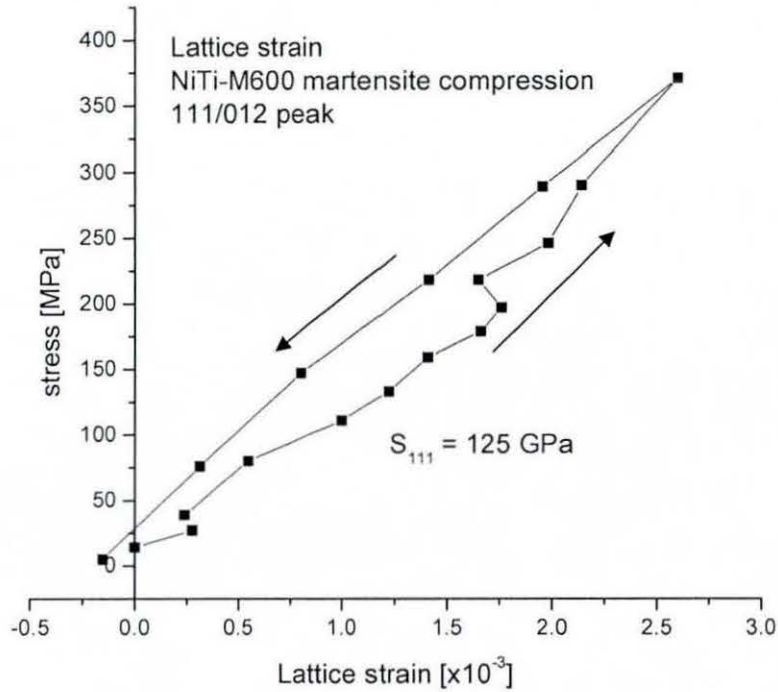


**Figure 5.10a (upper) and Figure 5.10b (lower):** Lattice strain evolution with applied stress of the (111)/(012) and (120) martensite peaks during the compression test. DEC's are included on the figures which are measured from linear portions of the curves. The compressive stresses and strains are represented as positive quantities in the figure.

modulus values. If we compare the DEC's for the martensite phase with those obtained for the austenite phase (results in chapter 3) we can see that in fact the moduli for the martensite peaks is much higher. This is a surprising result, as it is generally accepted within the modelling literature that the martensite is the softer phase. In fact some other experimental work by Sehitoglu et al has shown this conclusion and also the modelling work of Sittner et al indicates this conclusion. They found, in their study of the stress-induced martensitic transformation in NiTi, that simulation results more accurately reflected experimental results when martensite elastic constants were chosen to be 1.25 times greater than austenite ones, as opposed to their original estimation of being circa 80 % lower (Sittner et al, 2002). The DEC's measured above provide good experimental evidence that the values for the elastic constants of the martensite phase are higher than those for the austenite phase.

#### **5.4 Conclusions**

Detwinning is the dominant deformation mechanism in both tensile and compressive deformation. Previous TEM studies had indicated that martensitic NiTi does not detwin under compressive loading, however the intensity changes observed here in tests on bulk samples seems to indicate that it does. Modulus of various peaks with the spectra were measured and found to give values much higher than those for the austenite phase.

#### **5.5 References**

Gupta, S. P., and Johnson, A. A., *Trans. JIM*, 14, (1973), 292.



Knowles, K. M., and Smith, D. A., *Acta Metall.*, 29, (1981), 101.

Liu, Y., Xie, Z. L., Van Humbeeck, J. V., and Delaey, L., *Acta Materialia*, 46, (1998), 4325.

Liu, Y., Xie, Z. L., Van Humbeeck, J. V., Delaey, L., and Liu, Y. N., *Philosophical Magazine A*, 80(8), (2000), 1935.

Liu, Y., in Smart Materials, *Proceedings of SPIE*, 4234, (2001), 82-93.

Onda, T., Bando, Y., Ohba, T., and Otsuka, K., *Mater. Tran. JIM*, 33, (1992), 354.

Otsuka, K., Sawamura, T., and Shimizu, K., *Physica Status Solidi*, 5, (1971), 457.

Otsuka, K., and Ren, X., *Progress in Materials Science*, 50, (2005), 511-678.

Sittner, P., Novak, V., Lukas, P., Neov. D., and Lugovyy, D., *Proceedings of New Trends in Phase Transformations and their Applications to Smart Structures*, Metz, France, (2002).



## **Chapter 6:**

# **Cooling under fixed stress and recovery stress generation in NiTi**

### **6.1 Introduction**

#### *6.1.1 Martensitic transformation under constraint*

In Chapter 1 the shape memory effect was discussed whereby a shape memory alloy, deformed in the martensitic state, recovers all macroscopic strain via phase transformation back to the austenite phase. This process is known as free recovery.

In practical applications, however, not much use is made of the free recovery process. Generally speaking, the most useful properties result when the phase transformation is constrained in some way: usually by the imposition of an applied stress or strain. When the martensitic transformation takes place under constraint, either a stress (in the case of fixed strain) or strain (in the case of fixed stress) is generated. Since the generated stresses or strains can be controlled to certain extent through knowledge of the thermomechanical history of the sample and control of the applied stress or strain, such processes have obvious applications as actuators. It is in this field that NiTi components find many applications.

Probably the most useful functional property of NiTi, in terms of successful applications, is the generation of large stresses when the recovery of the

macroscopic shape of a NiTi element is impeded by an external constraint. The large stresses (up to around 700 MPa in some cases) are called *recovery stresses*. They find practical applications in, for example, pipe couplings and other types of shrink-to-fit components. The large stress means that, in some cases, NiTi elements have replaced the need for welding in some structures. Some copper-based SMA elements are also being produced commercially, although the stresses generated by these are not as high as for NiTi. The amount of stress generated strongly depends upon the thermomechanical history of the sample, e.g. prestrain prior to application of constraint (Van Humbeeck and Stalmans, 1998).

Despite the large application potential of these functional properties, experimental studies of them have been rare. Some, such as those by De Araujo et al have measured the strains generated as Ni-Ti-Cu wires were cooled through the martensitic transformation under various values of the applied stress. Resistivity changes were measured during cooling and can be used as a measure of the microstructural changes taking place (De Araujo et al, 1999).

Further work by Sittner et al also used in-situ resistivity measurements in conjunction with macroscopic stress-strain-temperature relations in order to provide insight into the microstructural evolution taking place while recovery stress generation occurred (Sittner et al, 2000).

In addition, some in-situ diffraction measurements of the phase transformation in NiTi under a fixed compressive stress of -250 MPa and some associated modelling work has been conducted by Sittner, Novak and co-workers (Sittner et al, 2004; Novak and Sittner, 2004). Here we conduct similar experiments with but under tensile stresses and strains. The results here will be compared with the previous micromechanical model and

experimental results where appropriate. The micromechanical model used is the same as that used in Chapter 2 for comparison with the in-situ diffraction results of SIMT in NiTi. Further details regarding the model are given in the appendix.

### *6.1.2 Objectives of present work*

The aims of the present work are as follows. The study the redistribution of the applied stress by the austenite grains (load partitioning mechanism) as the transformation proceeds under a fixed tensile stress, and to compare and contrast the results with those modelling and experimental results available in the literature for similar tests conducted under compression. In addition, further microstructural changes, i.e. phase fraction evolution and texture changes will be quantified during the tests for comparison.

## **6.2 Experimental details**

### *6.2.1 Material*

The material used in the experiment was Ni-49.8Ti (at.%) obtained from Memory Metalle in Germany. It is the same material used in the tension/compression deformation tests in Chapter 5 and in the stress-induced martensite experiment in Chapter 3. Samples were cut from the as-received material into shapes suitable for tensile testing. These are dumbbell shaped with a diameter of 7.8 mm at the gauge length. It was subjected to a heat treatment of 600 °C for 1 hour under vacuum before immediate quenching into water. The DSC thermogram for the material is shown in Figure 6.1.

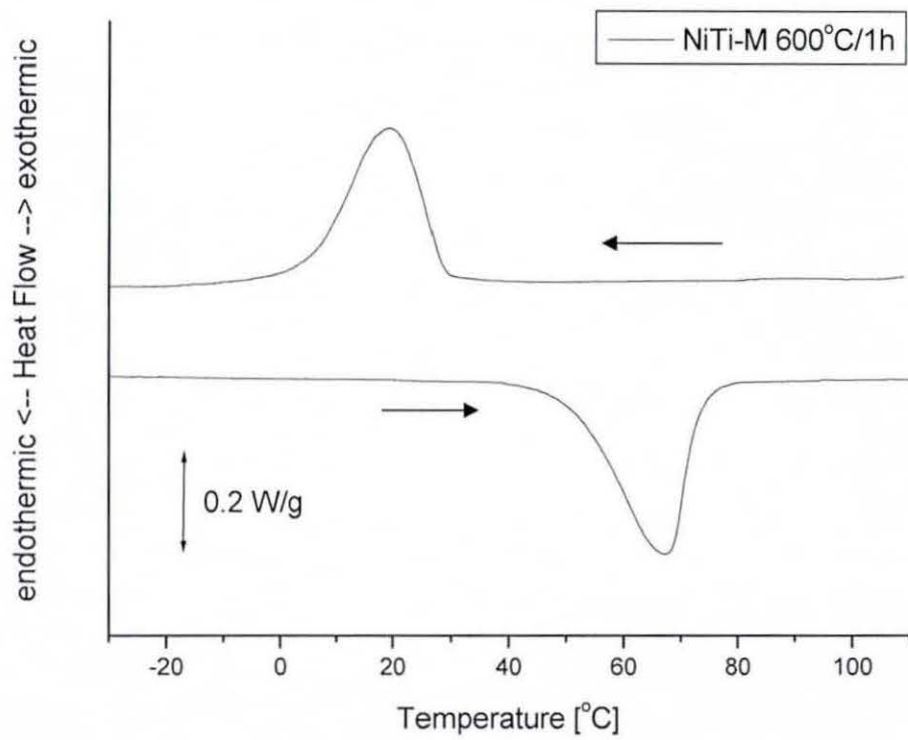


**Figure 6.1:** DSC thermogram of NiTi sample used in cooling under fixed stress and recovery stress generation experiments. A heating rate of 10 K/min was used.



The transformation temperatures are:  $M_s = 30\text{ }^{\circ}\text{C}$ ,  $M_f = 6\text{ }^{\circ}\text{C}$ ,  $A_s = 52\text{ }^{\circ}\text{C}$ ,  $A_f = 74\text{ }^{\circ}\text{C}$ .

### *6.2.2 Diffraction measurements*

The thermomechanical experiments were conducted using the ENGIN-X instrument at ISIS. The instrument was used in its standard configuration, as shown in chapter 2. Complex thermomechanical cycling was achieved through the use of the INSTRON loading rig equipped with heating apparatus. A thermocouple monitored the sample temperature with a standard precision of  $\pm 1\text{ K}$ . Sample strain was monitored by a clip-on extensometer. Essentially, two thermomechanical deformation experiments were carried out: (i) cooling the material through the martensitic transformation while a constant tensile stress of 200 MPa was maintained and (ii) the generation of recovery stress as the sample was heated through the reverse transformation under an imposed tensile strain of 4.79 %. All data was examined via single peak fits to the diffraction spectra.

## **6.3 Results and discussion**

### *6.3.1 Cooling under fixed tensile stress of 200 MPa*

The macroscopic stress-strain and strain-temperature relations recorded during the experiment are shown in Figure 6.2. The points at which diffraction spectra were collected are displayed at solid squares on the plots.

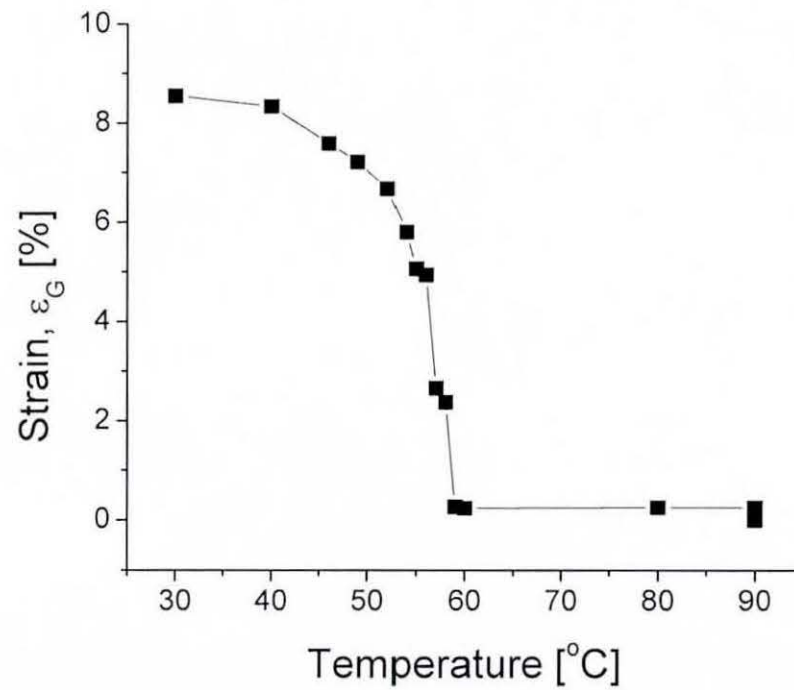
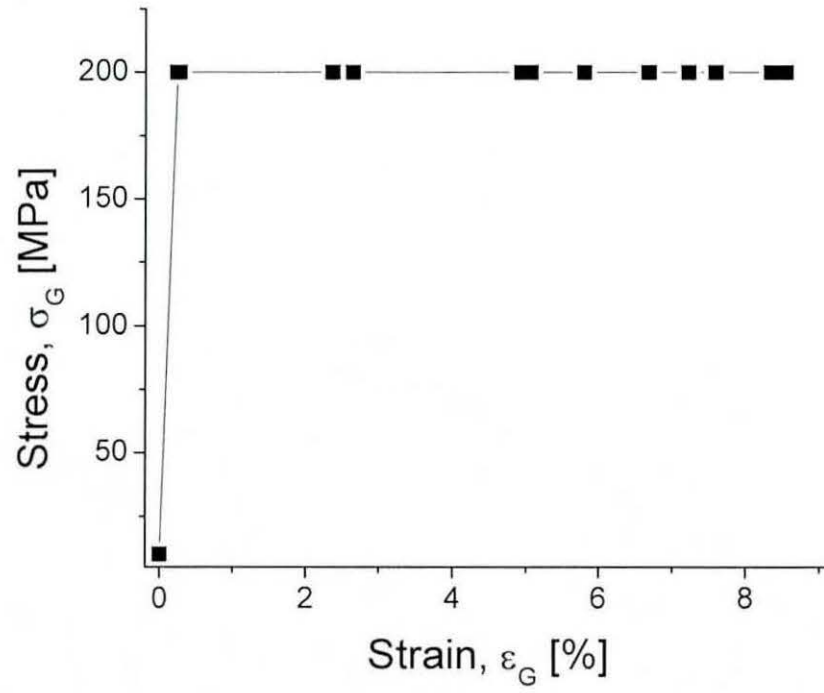


**Figure 6.2:** Macroscopic stress-strain and strain-temperature responses for NiTi cooled under a fixed tensile stress of 200 MPa. Diffraction spectra were collected at the points denoted by the solid square symbols.

The sample was heated to 90 °C in order that it was fully austenitic (see DSC curve in Figure 6.1). The stress-rig crosshead was adjusted during heating in order to maintain a zero strain condition. A diffraction spectrum was then recorded in order to provide the reference for subsequent strain measurements. The sample was then loaded to a tensile strain of 200 MPa and subsequently cooled to various temperatures while the stress remained constant. Concomitant with the lowering of the temperature was an increase in the macroscopic strain. This is due to the austenite to B19' martensite transformation. The R-phase is not a potential product phase in this experiment due to the solution heat treatment applied to the sample here.

Figure 6.3 shows the evolution of the intensity of the austenite (100), (110) and (111) grain families obtained by single peak fits to diffraction spectra collected in the axial detector as cooling takes place. These changes represent the transformation of regions of these grains to the B19' martensite. It is clear from the intensity changes in Figure 6.3 that the austenite grain orientations transform at different rates. In the case of cooling under a fixed tensile stress discussed here, the  $\langle 100 \rangle$  oriented grains transform preferentially, followed by the  $\langle 110 \rangle$  and the  $\langle 111 \rangle$  oriented grains, which leads to an evolving texture as the sample cools. This is due to preferential transformation of differently oriented grains. Interestingly, similar intensity changes were found in the cooling under a fixed compressive stress experiments undertaken by Sittner and co-workers, i.e. the  $\langle 111 \rangle$  grains were found to transform latest (Sittner et al, 2004). This is surprising due to the difference in the sense of the applied stress between the two experiments.

The strongly-textured nature of the sample is not just due to the preferential transformation of the austenite grains but also the formation of preferred



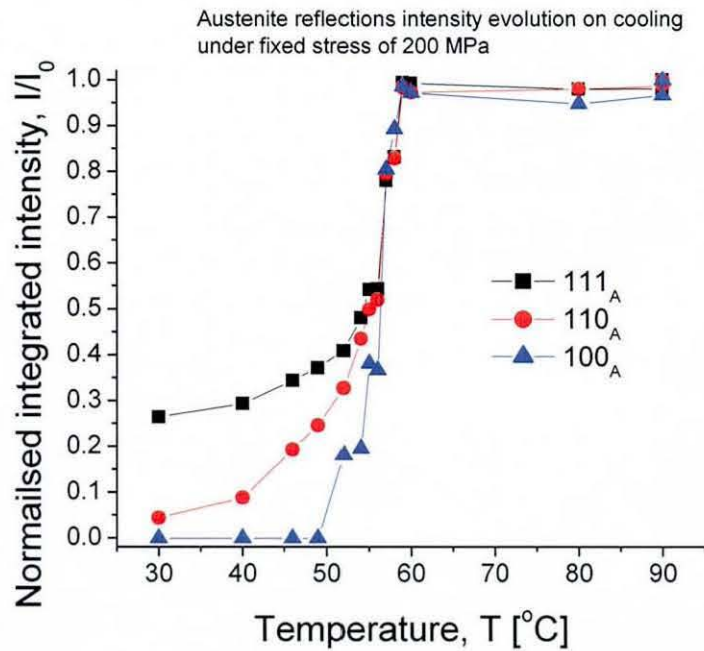


**Figure 6.3:** Intensity evolution for austenite reflections during cooling under a fixed tensile stress of 200 MPa. Intensity values are normalised with respect to those measured at 90 °C.

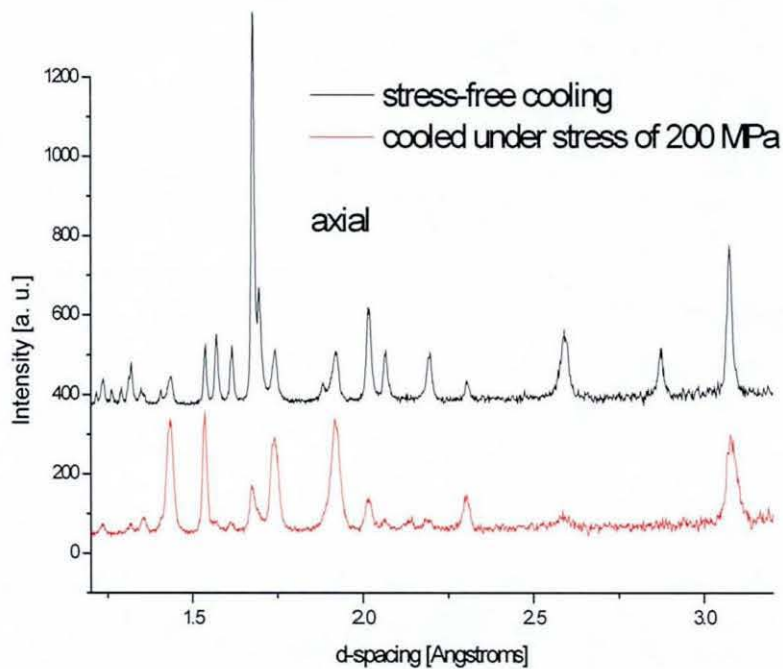


**Figure 6.4:** Comparison of full spectra acquired during stress-free cooling (upper trace) and cooled to a temperature of 30 °C under a fixed tensile stress of 200 MPa. Data collected in the axial detector.

variants, as seen in both the stress-induced martensite transformation (Chapter 3) and in the martensite compressive/ tensile detwinning experiments in Chapter 5. The same martensite peaks are seen to increase here as was observed in the tensile detwinning case, i.e. those peaks associated with variants providing maximum strain in the direction of an applied tensile stress are observed to grow. Comparison of the diffraction spectra obtained under stress-free cooling and at 30 °C after cooling through the martensitic transformation under an applied tensile stress, displayed in Figure 6.4, shows the strong difference in spectra obtained. The resulting martensite texture from cooling under a fixed tensile stress is almost identical to that obtained in the tensile detwinning test shown in Figure 5.5 in Chapter 5. This indicates that the samples have the same variant microstructure existing in them after cooling under a fixed tensile stress and detwinning of the thermally-induced, internally-twinned martensite. This is quite surprising due to the fact that they have been obtained via completely different deformation modes, i.e. B2 to B19' martensitic transformation in the case of cooling under fixed tensile stress and reorientation of twinned B19' martensite. The reason for this similarity is most likely due to the large stresses reached during the experiments – these cause almost full detwinning of martensitic variants.

The lattice strain evolution for the (100), (110) and (111) austenite grains is shown in Figure 6.5. The sample was loaded in the austenite state at 90 °C prior to cooling and from Figure 6.5 it can be seen that the different grain orientations are under different strain after loading to 200 MPa. This is due to the differences in elastic constants of these grain orientations and it thus follows that the most compliant orientation, the <100>, develops the most strain and the least compliant, the <111>, develops the least. On cooling there is a small change in the lattice strain due to thermal contraction.

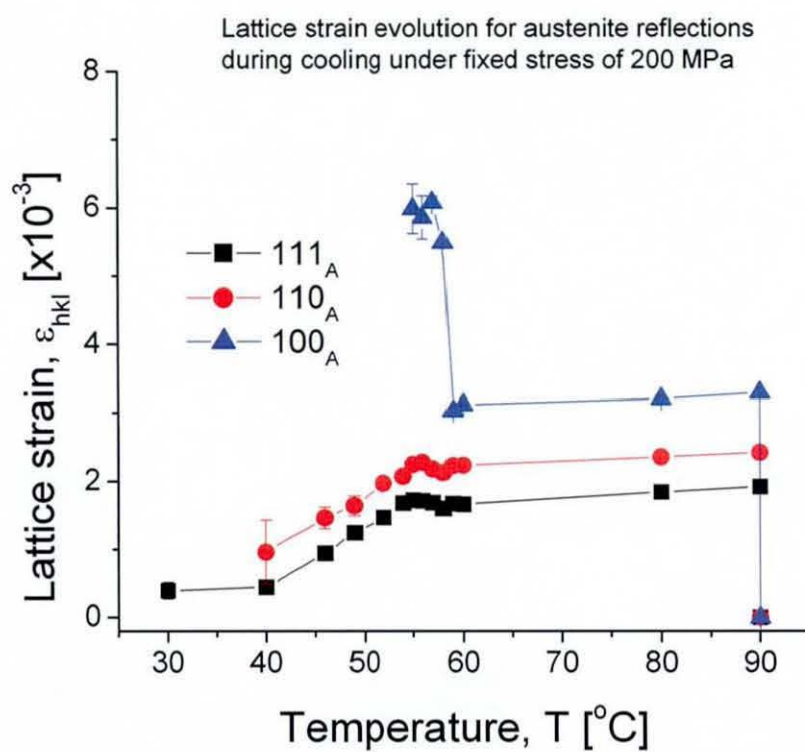


**Figure 6.5:** Lattice strain evolution in <100>, <110> and <111> oriented austenite grains during cooling under fixed tensile stress of 200 MPa.

However there is a large shift in the peak position of the (100) reflections at 60 °C. This coincides with a decrease in (100) austenite peak intensity at 60 °C is indicative of the martensitic transformation beginning. This decrease in intensity coincides with a large shift to greater tensile strain indicating the increased stress the austenite in this grain orientation is placed under. The strain then remains roughly constant with further cooling to 55 °C. Approximately 80 % of the <100> oriented austenite has transformed to martensite by this point (see Figure 6.3). Below 55 °C, the intensity of the (100)<sub>A</sub> peak reduces to such an extent that reliable values of peak position cannot be made, thus no lattice strains are reported after this point.

The (110)<sub>A</sub> and (111)<sub>A</sub> grains, however, show a greatly different lattice strain response to that exhibited by the (100)<sub>A</sub> grains. Figure 6.5 shows the strains within these grains to decrease as the transformation to martensite begins and proceeds, and thus shift the opposite way to the (100) grains, as the load is transferred to the growing martensite variants. In all cases the lattice strain should reduce to zero as the transformation nears completion and load is fully transferred to the martensite.

It is clear that while the external stress remains constant, the internal stress (proportional to internal strain) carried by different grain orientations changes greatly during transformation. This change in lattice strain is due to a change in the partitioning of the applied load as the martensitic transformation begins and proceeds, i.e. the applied stress is re-distributed amongst the various grain orientations due to transformation.

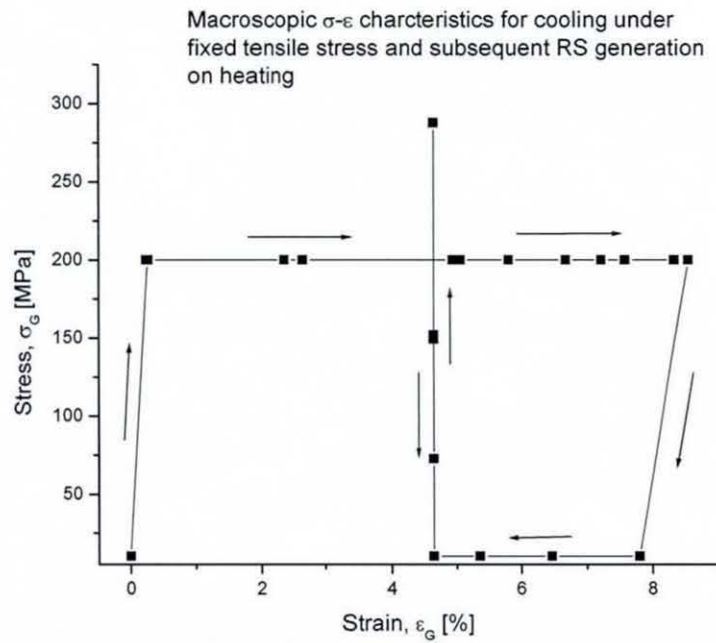
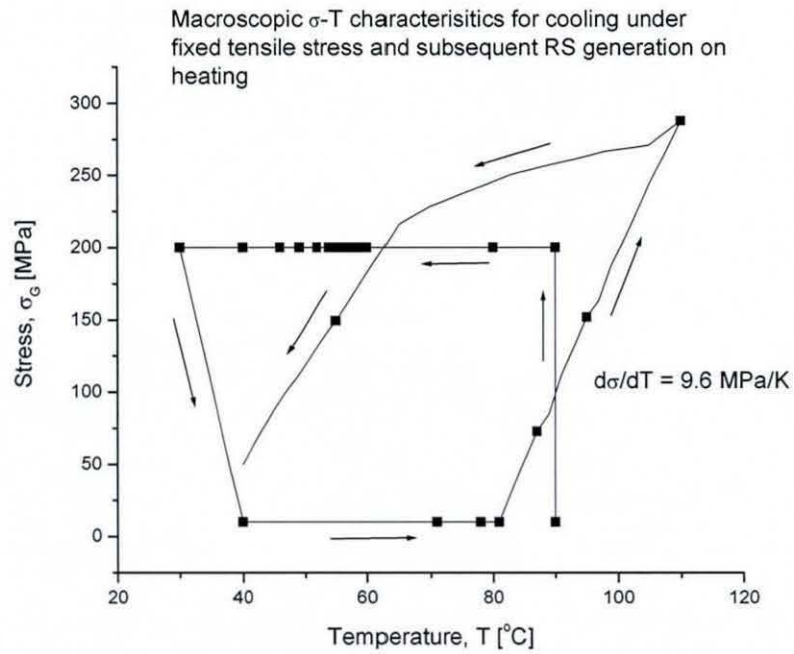
### *6.3.2 Recovery stress generation*



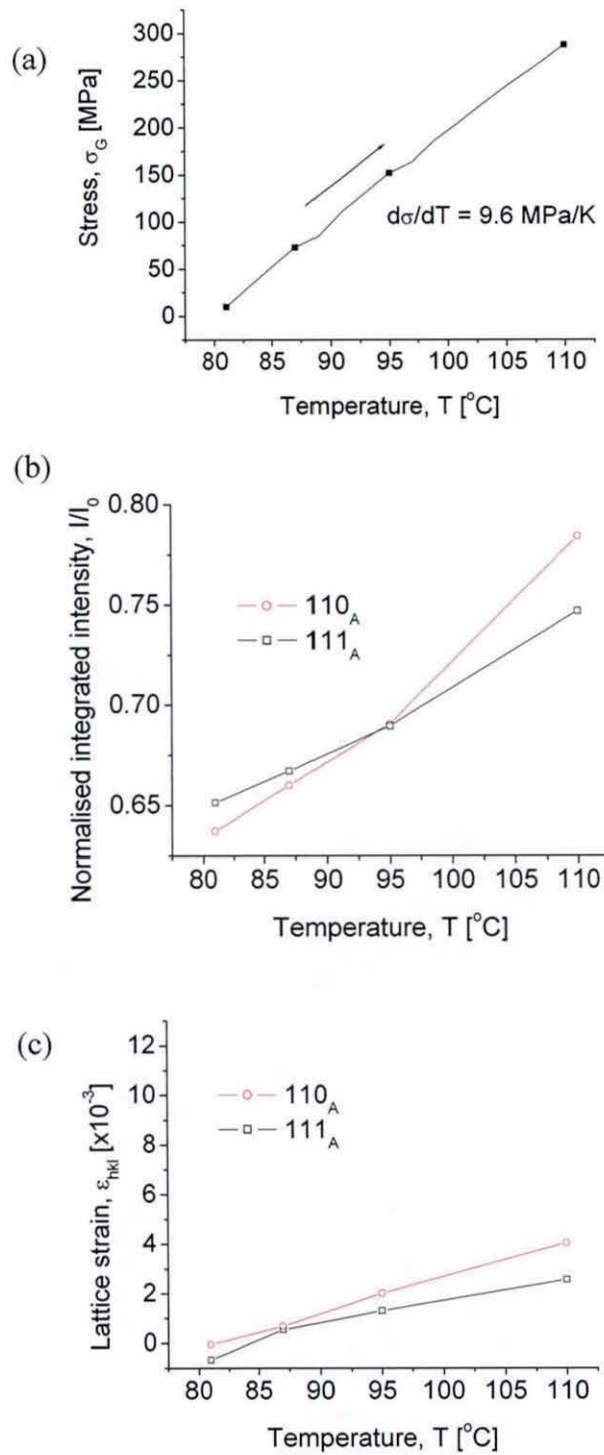
A recovery stress generation was carried out subsequent to the cooling under fixed tensile stress test detailed above. In the deformed martensitic state at 30 °C, the sample was unloaded and heated to 40 °C. It was then heated until recovery of the macroscopic shape began (the shape memory effect). This was allowed to continue until a macroscopic strain of 4.79 % existed (strain relative to that at 90 °C with the material fully austenitic). At this point, when the temperature was 81 °C, the stress rig was switched to strain-control mode and the strain fixed at a value of 4.79 % for the rest of the experiment. At this point, the microstructure of the sample consisted of a mixture of austenite and oriented martensite variants. The sample was then heated while the strain was fixed and diffraction spectra recorded at several temperatures. The macroscopic stress-strain-temperature response during the cooling under fixed stress and subsequent recovery stress generation is shown in Figure 6.6. It can be observed in the figure that a maximum stress of 288 MPa was generated through the constrained thermal cycle.

Figure 6.7a focuses on the heating part of the response with associated stress generation. Included in Figure 6.7 are the integrated intensity evolution and lattice strain response for the austenite (110) and (111) as the recovery stress is generated. The (100) peak provided unreliable fits in this test. Lattice strains and normalised intensities are determined via reference to peak fits performed at 90 °C while the material was fully austenitic and under a nominal load.

It can be seen from Figure 6.7, that the recovery stress generation involves the reverse B19' martensite to B2 austenite transformation. Before recovery stress generation begins, there is an approximately equal amount of austenite residing within the two grain orientations of about 65 %, which increases for both peaks as the sample is heated. The linearity of the growth in integrated



**Figure 6.6:** Macroscopic stress-strain-temperature response for NiTi sample cooled under fixed stress followed by free recovery to a strain of 4.79 % and then heating while the strain remained fixed at this value.



**Figure 6.7:** (a) Stress-temperature relation during constrained heating. The solid squares indicate the points at which diffraction measurements were obtained, (b) integrated intensity evolution during heating for the (110) and (111) austenite reflections and (c) lattice strain response for (110) and (111) austenite reflections during constrained heating.



intensity for the (110) and (111) reflections indicates that there is a linear relationship between austenite volume fraction and generated stress. The  $\langle 110 \rangle$  oriented grains transform back to austenite at a greater rate than do the  $\langle 111 \rangle$  grains providing some evidence of preferential transformation and texture evolution during constrained heating.

Figure 6.7c shows the lattice strain response for the  $\langle 110 \rangle$  and  $\langle 111 \rangle$  oriented grains. These clearly increase as the recovery stress is generated and the martensite reverts back to austenite. This is most likely due to increasing volume fraction of austenite within these grain orientations, which will take on progressively more of the load as the volume fraction increases. The  $\langle 110 \rangle$  oriented grains can be seen to have a slightly steeper lattice strain response than the  $\langle 111 \rangle$ . This result corresponds to the predicted lattice strain response found by the micro-mechanical modelling work of Novak and Sittner for recovery stress generation under a fixed tensile strain (Novak and Sittner, 2004).

The (100)<sub>A</sub> austenite peak does not appear to show any great growth, in contrast to the (110) and (111) austenite reflections, during constrained heating at 4.79 % strain. Figure 6.8 shows the region around this reflection d-spacing and includes the spectra at 81 °C: the temperature at which the strain was arrested and heating began. The profile appears to be that of a very strongly broadened (011) martensite reflection. There is little, if any, reflected intensity from the (100) austenite peak. It therefore appears that severe plastic deformation has taken place within the  $\langle 100 \rangle_A$  oriented grains. This is most likely a consequence of the comparatively large strain (4.79 %) imposed on the sample prior to heating.

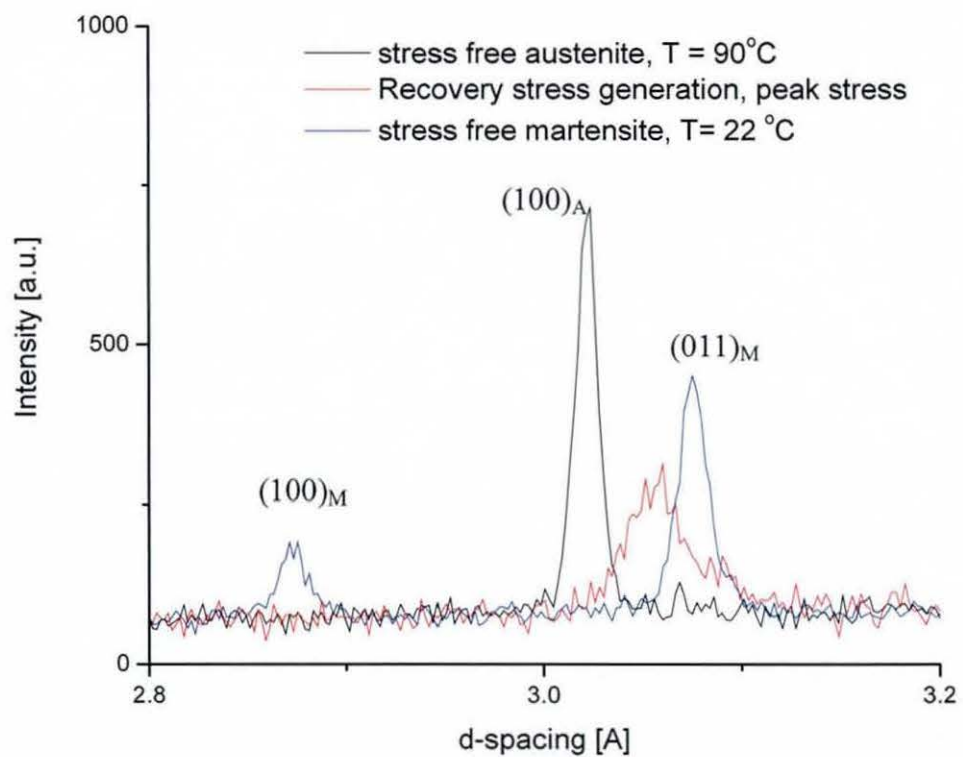


**Figure 6.8:** Diffraction profile changes at the peak stress of 288 MPa in the constrained heating cycle, compared with stress-free austenite and stress-free martensite spectra. The profile indicates strong plastic deformation in the  $\langle 100 \rangle$  oriented grains.

## 6.4 Conclusions

In-situ neutron diffraction studies of NiTi cooled through the martensitic transformation under a fixed tensile stress of 200 MPa and subsequent recovery stress generation have been studied. Significant changes in the lattice strain response for austenite (100), (110) and (111) grains have been observed related to the load transfer behaviour during the martensitic transformation in these grains. Evidence of evolving texture has also been observed with  $\langle 100 \rangle$  oriented grains seen to transform preferentially and  $\langle 111 \rangle$  latest. A subsequent recovery stress experiment showed stress generation of 288 MPa while the NiTi element was held at a macroscopic strain of 4.79 %. Austenite volume fraction increases on heating were found to be linear with increasing temperature as were the lattice strain responses for the  $\langle 110 \rangle$  and  $\langle 111 \rangle$  oriented grains. This result agrees well with the micro-mechanical simulation results in the literature (Novak and Sittner, 2004). There is strong evidence that, at this particular strain, extensive plastic deformation occurs in the  $\langle 100 \rangle_A$  oriented grains on constrained heating.

## 6.5 References

- De Araujo, C. J., Morin, M., and Guenin, G., *Materials Science and Engineering A*, 273-275, (1999), 305-309.
- Novak, V., and Sittner, P., *Materials Science and Engineering A*, 378, (2004), 490-498.

Proft, J. L., and Duerig, T. W., The Mechanical Aspects of Constrained Recovery, in T. W. Duerig, K. N. Melton, D. Stockel and C. M. Wayman (Eds.), *Engineering Aspects of Shape Memory Alloys*, Butterworth-Heinemann, (1990), 115-129.

Sittner, P., Vokoun, D., Dayananda, G. N., and Stalmans, R., *Materials Science and Engineering A*, 286, (2000), 298-311.

Sittner, P., Lukas, P., Novak, V., Daymond, M. R., and Swallowe, G. M., *Materials Science and Engineering A*, 378, (2004), 97-104.

Van Humbeeck, J. V., and Stalmans, R., Characteristics of Shape Memory Alloys, in K. Otsuka and C. M. Wayman (Eds.), *Shape Memory Materials*, Cambridge University Press, (1998), 149-183.



## **Chapter 7:**

### **Conclusions and suggestions for future research**

#### **7.1 Summary**

Chapters 1 and 2 were introductory in nature and covered the basics of both the thermodynamic, mechanical and crystallographic properties of martensitically transforming materials, and of the in-situ neutron diffraction technique – the main experimental technique used in this thesis. Chapters 3-6 covered the results and conclusions from the various experiments undertaken. These were chosen such that they encompassed the types of deformation behaviour associated with monotonic loading of NiTi alloys in practical applications such as isothermal stress-induced transformation, cooling under a fixed stress and recovery stress generation under constraint. Also covered was the important materials science problems of the effect of ageing in nickel-rich alloys on the mechanical behaviour, as well as studies of the tension-compression asymmetry in the deformation of twinned B19' martensite.

Chapter 3 focussed on the stress-induced martensitic transformation in a commercial NiTi rod during compressive loading. Single peak fitting analysis was used to determine both the lattice strain response and evolution of martensite/austenite phase volume fractions existing within several grain families during the deformation. Intensity changes were seen to correspond with the variant selection mechanism seen in shape memory alloys which resulted in the growth of those variants providing maximum strain when resolved along the loading axis. Quantitative measurements were made of

these changes in peak integrated intensity and the results were compared with micromechanical model results for polycrystalline NiTi available within the literature. The lattice strain responses were measured using single peak fits to the data collected. The initially linear responses of grain families both parallel and perpendicular to the applied stress were compared with theoretical predictions based on the average responses predicated by the Voigt and Reuss approaches to an elastically deforming polycrystal (the Hill-Kneerfeld average). Reasonable agreement was achieved despite the fact that the theoretical results are based on a random distribution of grains in the material. The lattice strain response into the transformation regime was seen to deviate from the initial linearity. This was ascribed to the particular load transfer behaviour which resulted from the preferential transformation of particular grain orientations. The  $(111)_A$  was seen to exhibit behaviour opposite to that of the  $(100)_A$  and  $(110)_A$  as a result of the lack of transformability in this particular grain orientation.

Chapter 4 examined the mechanical behaviour of a nickel-rich NiTi alloy after being subjected to ageing at 400 °C for two different lengths of times, which generally results in the formation of  $Ni_4Ti_3$  precipitates within the material. Deformation of an unaged sample was also carried out for comparison. DSC testing of the samples indicated a single step  $B2 \leftrightarrow B19'$  martensitic transformation taking place in the unaged alloy. The aged sample, however, exhibited multi-step transformation behaviour with three peaks being observed in the DSC thermogram on heating and cooling. All samples were deformed at room temperature. It was clear from mechanical testing at room temperature that the ageing heat treatments have a strong effect on mechanical behaviour due to the presence of the R-phase in the aged samples with differences in moduli and yield stresses for all samples. Detwinning of the R-phase was seen to be active as a deformation mode in



aged samples from a very low applied stress. This was observed in both aged samples and indicates that the interfaces formed during the austenite to R-phase transition are very glissile under an applied stress. It was also noted that there is a difference in measured R-phase rhombohedral angle in samples aged for different lengths of time. This is known to have a strong effect on the recoverable strains possible due to R-phase reorientation and undoubtedly has an effect on the mechanical behaviour. Clear growth of R-phase and B19' variants providing maximum strain along the stress axis was observed in the tests. In the initial stages of deformation the mechanism in aged samples is detwinning of the R-phase via variant reorientation. When this process is exhausted stress induced B19' transformation of the preferential variants begins. Yield in the measured stress-strain curves was found to be due to B19' martensite formation in all cases. The differences in yield stress (or more accurately transformation stress) are due to composition changes in the matrix caused by the precipitation process, which lowers the nickel content of the matrix and thus increases the transformation temperatures of the material. The knock-on effect of this is that the critical stress required to induced the B19' martensite is lowered and thus the apparent yield stress of the aged materials is decreased, and decreases further with increased ageing time.

The work detailed in Chapter 5 investigates the origin of the tension-compression asymmetry in the deformation of B19' martensitic NiTi. Detwinning was found to be the dominant deformation mechanism in both tensile and compressive deformation. Previous TEM studies had indicated that martensitic NiTi does not detwin under compressive loading, however the intensity changes observed here in tests on bulk samples seems to indicate that it does. Modulus of various peaks within the spectra were



measured and found to give values much higher than those for the austenite phase.

In Chapter 6 the martensitic transformation under an external constraint was studied by cooling through the transition under a fixed tensile stress and then heating the material while a fixed macroscopic strain was imposed on the sample. During the in-situ neutron diffraction studies of NiTi cooled through the martensitic transformation under a fixed tensile stress significant changes in the lattice strain response for austenite (100), (110) and (111) grains have been observed related to the load transfer behaviour during the martensitic transformation in these grains. Evidence of evolving texture has also been observed with  $\langle 100 \rangle$  oriented grains seen to transform preferentially and  $\langle 111 \rangle$  latest. The subsequent recovery stress experiment showed stress generation of 288 MPa while the NiTi sample was held at a macroscopic strain of 4.79 %. Austenite volume fraction increases on heating were found to be linear with increasing temperature as were the lattice strain responses for the  $\langle 110 \rangle$  and  $\langle 111 \rangle$  oriented grains. This result agrees well with the micro-mechanical simulation results in the literature. There is strong evidence that, at this particular strain, extensive plastic deformation occurs in the  $\langle 100 \rangle_A$  oriented grains on constrained heating.

## **7.2 Future research**

The work in this thesis on the ageing of nickel-rich NiTi alloys could be extended to incorporate microscopy work in order to determine the effects of precipitate volume fraction, size and distribution within grains. Further work could be carried out with more ageing times and different ageing temperatures to see the effects on both thermal and mechanical behaviour.

Of interest in furthering the detwinning study of Chapter 5 would be the use of tension-compression samples in order to observe the reorientation/twinning behaviour under these conditions. This can also be conducted over many cycles in order to observe changes in variant microstructure and residual strain build-up. In studies of the cooling under fixed stress in chapter 6, further work may be conducted by performing testing using a variety of fixed stresses combined with different heat treatments applied to sample prior to testing. Tests may also be conducted under compression to provide further information on variant selection within the material.

## **Appendix A**

### **The Sittner-Novak model**

#### **A1 Introduction**

The purpose of this appendix is to provide some basic details about the Sittner-Novak model of thermomechanically deforming shape memory alloys, due to its use within this thesis. Since the work included in this thesis is focussed solely upon the deformation of NiTi alloy, this alloy system will be focussed upon in the subsequent sections. The model is, however, applicable to other alloy systems such as the copper-based shape memory alloys where it has been successfully used in studies of the load partitioning behaviour, for example, in previous in-situ diffraction experiments.

#### **A2 Properties and assumptions**

The model is capable of simulating both the microscopic, e.g. internal strain and phase volume fractions, and macroscopic stress-strain-temperature response of polycrystalline samples. It evaluates the grain interactions in a self-consistent manner and is capable of incorporating the texture of the austenite phase. Since the simulation results provide information such as the lattice strain response and evolution of martensitic transformation within particular grain orientations for example, the output of the model is comparable with the results from single-peak fits to the in-situ diffraction data.

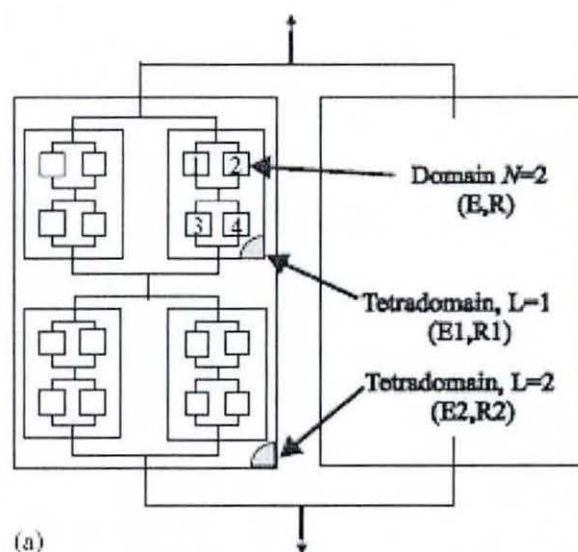


**Figure A1:** Layout by which grain interaction takes place within the model. For example, constant strain prevails in domains 1 and 2, whereas there is constant stress in bi-domains 1 and 2, and 3 and 4, respectively. Figure reproduced from Novak and Sittner, 2004.

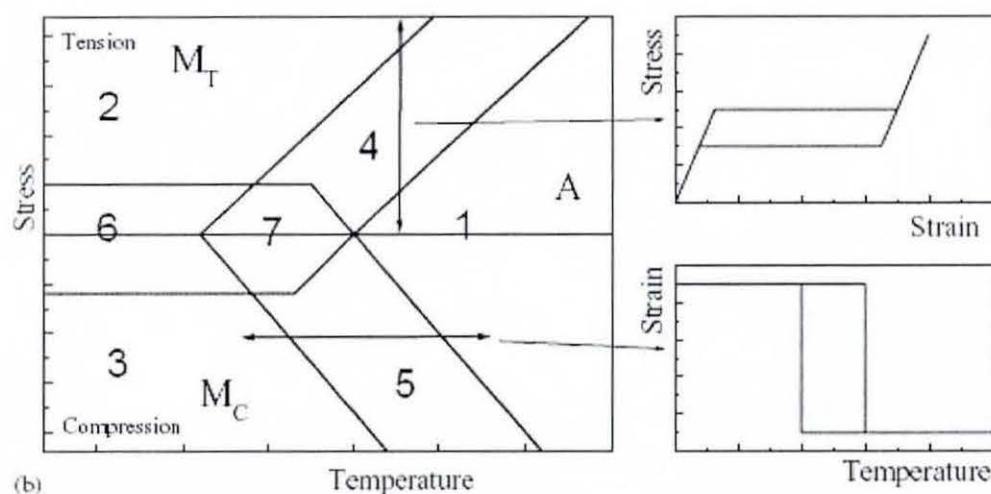


**Figure A2:** Types of processes which may take place within a particularly oriented domain. The simplest possible stress-strain and strain-temperature hysteretic response within a domain is assumed, as shown on the right-hand side of the figure. Transformation is from austenite to one of two variants denoted  $M_T$  in the case of tensile loading and  $M_C$  under compression. Figure reproduced from Novak and Sittner, 2004.



In the model the polycrystal is assumed to consist of an aggregate of around 200,000 oriented, dimensionless domains in which a uniaxial stress state is assumed. These deform according to the thermal expansion, elastic properties and transformation characteristics particular to their assigned orientation, i.e. the appropriate single-crystal values of these properties. The domains transform between austenite and two possible martensite variants: a tensile variant,  $M_T$ , and a compression variant,  $M_C$ , when the uniaxial stress and temperature reach the appropriate value given by the transformation slopes, obtained via the Clausius-Clapeyron equation, as shown in Figure A1. The domains interact via the tetra-domain layout displayed in Figure A2 which mixes constant stress and constant strain conditions for different domains. Internal stresses and strains and evolving martensite volume fractions are calculated, along with the macroscopic stress-strain-temperature response in a recursive manner using incremental steps in which either the macroscopic stress or strain, and the temperature are prescribed. For further details, including examples of the simulation output of relevance to the results presented in this thesis, the reader is referred to the following publications: Sittner and Novak, 2000; Novak and Sittner, 2004.

### A3 References

Sittner, P., and Novak, V., *International Journal of Plasticity*, 16, (2000), 1243-1268.

Novak, V., and Sittner, P., *Materials Science and Engineering A*, 378, (2004), 490-498.



